

# University of Napoli Federico II



## Ph. D. in Chemical Sciences XXXIV Cycle

*Design and structural study of novel organic and  
organic-inorganic hybrid compounds for advanced materials*

### **Ph.D. Student:**

Emmanuele Parisi

### **Tutor**

Prof. Roberto Centore

Prof. Antonio Carella

### **Coordinator**

Prof. Angelina Lombardi

### **Supervisor**

Prof. Finizia Auriemma

**2019-2021**

# Contents

<b>Abstract</b> .....	
<b>Index of Abbreviations</b> .....	
<b>Chapter 1 Introduction</b> .....	1
<b>Chapter 2 Fused-Ring Heteroaromatics</b> .....	7
<b>2.1 General aspects</b> .....	7
<b>2.2 Study of Topochemical Reactivity and Intermolecular Interactions in Different Polymorphs of Fused-Ring Heteroaromatics</b> .....	10
<b>2.2.2 Analysis of Chalcogen Bonding Interactions</b> .....	15
<b>2.2.3 Solid-State Topochemical Reactivity</b> .....	19
<b>2.3 Effect of chalcogen bond on the packing and coordination geometry in hybrid organic-inorganic Cu(II) networks.</b> .....	27
<b>2.3.1 Crystallographic and computational analysis</b> .....	28
<b>2.3.1 Preliminary Magnetic Characterization and Further Development</b> .....	37
<b>Chapter 3 N-Rich Heterocyclic Compounds</b> .....	40
<b>3.1 General aspects</b> .....	40
<b>3.2 New Versatile N-Rich Heterocycle Ligand</b> .....	42
<b>3.2.1 Analysis in solution</b> .....	45
<b>3.2.2 Crystallographic and computational analysis</b> .....	46
<b>3.3 High-Energy Density Materials</b> .....	61
<b>3.3.1 General aspects</b> .....	61
<b>3.3.3 Crystallographic and computational analysis</b> .....	68
<b>3.3.4 Thermal and sensitivity analysis</b> .....	78
<b>Chapter 4 Organic Polar Crystals</b> .....	81
<b>4.1 General aspects</b> .....	81
<b>4.2 Imines for NLO applications</b> .....	84

4.2.1 Thermal and crystallographic analysis .....	87
4.2.2 SHG measurements.....	95
4.3 Mechanically Responsive Molecular Crystals .....	98
4.3.1 General aspects.....	98
4.3.2 Crystallographic analysis of Tol_NMP phases .....	100
4.3.3 Dynamic behaviour .....	106
Chapter 5 Conclusions.....	110
Appendix A: Synthesis and Crystallization .....	113
Appendix B: Materials and Methods .....	133
Appendix C: Crystallographic Data.....	146
List of Publications.....	154
Bibliography .....	156

## **Abstract**

The Crystal Engineering approach has extended its outreach into many aspects of structural science. Indeed, this tool is all about the design of molecular crystal structures and there is now greater emphasis on property design. For this reason, there is a growing effort in the development of new materials in several research fields. This Ph.D. project aims to exploit the Crystal Engineering approach to design and synthesize novel organic and organic-inorganic hybrid materials for advanced materials applications. The first part of the work deals with the application of Crystal Engineering in recent years and its use in the context of this project. In particular, chapter 2 is dedicated to polymorphism and materials for application in organic electronics. Moreover, the chalcogen bonding effect is used to drive different crystal packings for similar crystal structures. Chapter 3 describes the work carried out on novel N-rich heterocyclic compounds. In particular, I will discuss the rich tautomerism behaviour of these systems and their application in the High-Energy-Density materials research field. Lastly, Chapter 4 is focused on organic polar crystals and mechanically responsive dynamic crystals. These materials find their application as NLO active materials and optical actuators, respectively. This work was carried out in collaboration with the group of Professor Thomas Klapoetke group at the Ludwig- Maximilian University of Munich, Professor Andrea Peluso at the University of Salerno and Dr. Stefano Lettieri at CNR-ISASI.

## **Index of Abbreviations**

5-ATN: 5-aminotetrazolium nitrate

AFM: Antiferromagnetic

Benzim: (E)-N'-benzylidene-4-hydroxybenzohydrazide

btd-1: poly (2,1,3-benzothiadiazole)copper(II) dichloride

btd-2: poly (2,1,3-benzothiadiazole)copper(II) dibromido

bTT: 1*H*,4'*H*-[3,3'-bi(1,2,4-triazole)]-4',5,5'-triamine

bsed-1: poly (2,1,3-benzoselenadiazole)copper(II) dichloride

bsed-2: bis(2,1,3-benzoselenadiazole-*k*N)dibromidocopper(II).

Chlorim: (E)-N'-(4-chlorobenzylidene)-4-hydroxybenzohydrazide

CL-20: hexazahexanitroisoximide

CSD: Cambridge Structural Database

DMF: N,N-dimethylformamide

DMSO: Dimethylsulphoxide

EWG: Electron Withdrawing Group

Fluorim: (E)-N'-(4-fluorobenzylidene)-4-hydroxybenzohydrazide

FM: ferromagnetic

HAT-DN: 5-aminotetrazolium dinitramide

HBI: 4-hydroxybenzohydrazide

HEDMs: High Energy Density Materials

HL: neutral ligand

H<sub>2</sub>L<sup>+</sup>: protonated ligand

H<sub>3</sub>L<sup>2+</sup>: diprotonated ligand

HMX: 1,3,5,7-Tetranitro-1,3,5,7-tetrazocane

L<sup>-</sup>: deprotonated ligand

Metoxim: (E)-N'-(4-acetylbenzylidene)-4-hydroxybenzohydrazide

NLO: Non-Linear Optics

NMP: N-methyl-pyrrolidone

NSeD: naphto[2,3-c][1,2,5]selenadiazole

NTD: naphto[2,3-c][1,2,5]thiadiazole

OSCs: Solution processed organic solar cells

RDX: 1,3,5-Trinitro-1,3,5-triazinane

RFID: Radio-frequency IDentification

SBIs : secondary bond interactions

SCSC: single-crystal to single-crystal

Toluim: (E)-4-hydroxy-N'-(4-methylbenzylidene)benzohydrazide

TKX-50: bishydroxylammonium 5, 5'-bis (tetrazolate-1N-oxide)

TNT: trinitrotoluene

TT9: 4-methyl-7-(pyrazin-2-yl)-2H-[1,2,4]triazolo[3,2-c][1,2,4]triazole

## Chapter 1 Introduction

Why does a crystal have the structure it has and not another one? Is it possible to predict the crystal structure? There are no simple answers to these apparently simple questions and, only in limited cases, convincing explanations can be given. In most cases, it is only possible to hypothesize solutions, and indeed, a pioneer in the rational study of the crystal packing of molecular compounds was Kitaigorodsky.<sup>1</sup> How uncertain it is to find a *priori* crystal structure is confirmed by the frequent manifestation of polymorphism, that is the occurrence of different crystalline phases of a given compound resulting from the possibility of different arrangements of molecules of that compound in the solid-state. However, a reliable *priori* knowledge of the crystal structure of a compound without the need of analyzing the crystals or even physically having them could save time and money. All this because many chemical and physical properties in the solid-state, *i.e.* electronic or proton conductivity, ferromagnetism, non-linear optics, and catalytic properties, are a consequence of the crystal structure.

For this reason, the development in molecular design to obtain molecules or crystals with defined properties has become more and more increasing in recent years. Crystal engineering is the rational design of functional molecular solids. This subject is of both fundamental and practical interest to solid-state structural chemists.<sup>2</sup> The term "crystal engineering" was coined by Pepinsky in 1955<sup>3</sup> but was not implemented until Schmidt studied a series of solid-state reactions in crystalline solids.<sup>4</sup> The study of intermolecular interactions, packing modes, and crystal properties are the three logical steps of crystal engineering. The interactions between molecules are analyzed in terms of hydrogen bonds, and other Secondary Bond Interactions (SBIs) and crystal structures are viewed as building blocks linked through supramolecular synthons.<sup>5</sup> Therefore, this field of research focuses on developing a synthetic strategy, which starts from a retrosynthetic step through the use of essentially simpler chemical entities, named

supramolecular synthons. Then, Supramolecular synthons are spatial arrangements of intermolecular interactions and play a focusing role in crystal engineering similar to that of the conventional synthon in molecular synthesis. Thus, during crystallization, a molecule that is endowed with a set of functionalities or functional groups through a molecular recognition process exploits weak interactions to generate supramolecular synthons that uniquely define the crystal structure (Figure 1). In many supramolecular syntheses, some synthons are kinetically dominant and invariably present when the molecules have specific functionalities. In this way, it becomes possible to identify several features that tend to retain supramolecular synthons by promoting the design of desired crystalline structures.

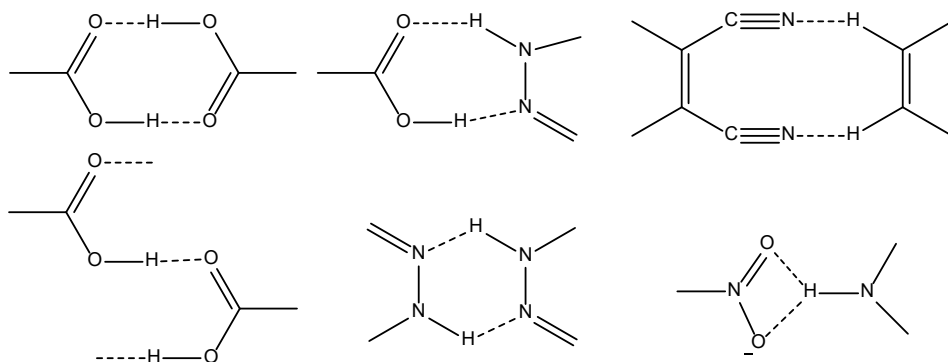


*Figure 1. Representative supramolecular synthons*

In fact, the goal of crystal engineering is to recognize and design synthons that are robust enough to be exchanged from one network structure to another, which ensures generality and predictability. Such structural predictability leads, in turn, to the anticipation of one-, two-, and three-dimensional patterns formed with intermolecular interactions.<sup>5</sup> In this regard, crystal engineering has found widespread applications: the development of new metal-organic frameworks for gas absorption and storage<sup>6</sup> and pharmaceutical polymorphs and cocrystals<sup>7</sup> (salts, solvates, clathrates, inclusion crystals, and hydrates).

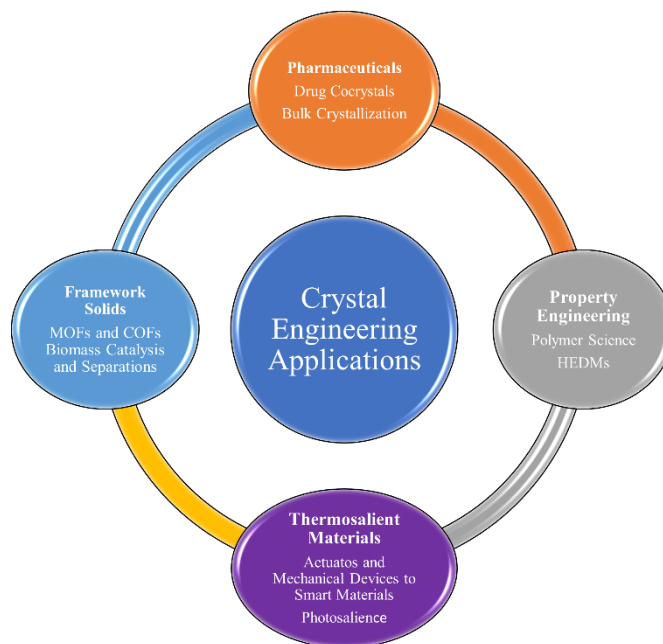


Figure 2. Application domains of the field of Crystal Engineering.

Crystal engineering represents an important tool as well to develop novel materials in several fields of relevant technological interest.<sup>8-17</sup> First, developing novel organic semiconductors (OSCs) for application in organic electronics is the focus of a strong industrial and academic research effort.<sup>18</sup> Organic electronics represent one of the market sectors with the higher compound annual growth rate (29.5% in the period-2014-2020)<sup>19</sup>. OSCs show the ability to combine traditional semiconductors' electronic properties with the lightness and flexibility typical of organic materials. This feature opens the way to novel applications not affordable for silicon-based electronics (building-integrated photovoltaics, wearable electronics, flexible RFID and so on) that will revolutionize the next future world. Organic light-emitting diodes (OLED) are an already mature technology, and great effort has been devoted in the last years to the realization of materials with optimized performance in the field of organic photovoltaics (OPV) and organic transistors (OFET), and crystal engineering proved to be a solid support in this

context.<sup>20</sup> Organic electronics is in fact a multidisciplinary realm and one of the most important tasks of the chemist is the design and synthesis of novel materials that address specific issues. In this regard, heteroatom annulation strategies or replacing carbocyclic rings of the fused polyaromatic systems with heterocyclic counterparts are becoming an emergent approach to produce crystals with a molecular packing favourable for electronic transport. Progress in this area has been considerable, setting new materials for higher OFET performance than the current benchmark and introducing new design concepts for engineering materials and crystals.<sup>21,22</sup> Hybrid materials, as well, like organic-inorganic perovskites, are very appealing and represent the most attractive materials in new generation photovoltaics, affording solar cells with efficiency exceeding 20%.<sup>23-27</sup> Perovskites derive their name from the mineral structure of calcium titanium oxide (CaTiO<sub>3</sub>), discovered in the year 1839 by Gustav Rose and characterized by Perovski, from which it derives its name. The key feature of organic-inorganic material research focuses on employing the range of interactions found within organic and inorganic chemistry to create a composite with some enhanced property relative to that achievable with either organic or inorganic materials alone, or to combine useful properties of the two components within a single molecule.<sup>28</sup> In some cases, the goal is to search for new phenomena that result from the interaction between the organic and inorganic subunits. Complex structures, based on a molecule scale composite of inorganic and organic components, provide a substantial opportunity for tailoring new and functional materials for scientific exploration and technological applications. Inorganic materials, typically characterized by covalent and ionic interactions, offer the potential for high electrical mobility, a wide range of band gaps (supporting the design of insulators, semiconductors and superconductors), interesting magnetic interactions, a range of dielectric properties, substantial mechanical hardness, and thermal stability. Organic molecules, which generally interact through weaker

interactions such as hydrogen bonding and Van der Waals interactions, provide the possibility of structural diversity, highly efficient luminescence, a large degree of polarizability and plastic mechanical properties. For all these exciting combinations, hybrid materials are also potential candidates for optoelectronic applications and high-energy-storage capacitors.<sup>29</sup> From the structural viewpoint, 2D perovskite-like materials break the strict restrictions of the tolerance factor to organic cations and show remarkable structure tunability.<sup>30</sup> The field of organic photonics also can take advantage of the potentiality of the crystal engineering approach. The design and realization of polar crystals are of great interest for the realization of photonic devices such as light modulating systems, photorefractive devices, and optically switchable molecular machines.<sup>18,31,32</sup> The specific interest in polar crystals is mainly due to the variety of physical properties that can manifest in these devices. Pyroelectricity, piezoelectricity, electro-optic effect and NLO effect are only allowed or enhanced in polar space groups.<sup>33,34</sup> The bulk NLO activity can be deduced by measuring one of the effects arising from non-linear optical properties.

Another class of innovative materials, where  $\pi$ -stacking and hydrogen bonding need to be finely balanced (by applying the principles of crystal engineering), are the low-sensitivity and high-energy-density materials (HEDMs). These compounds are becoming increasingly popular among energetic materials because of their potential applications as explosives, propellants, or solid fuels.<sup>35,36</sup>

Other interesting applications are those related to mechanically responsive molecular crystals, *i. e.* crystals that can sense and respond to an external stimulus (e. g. heat, light) by a macroscopic mechanical motion (e. g. hopping, twisting, bending, reshaping) of the whole crystal. Mechanically responsive crystals are at the frontier of present research in Chemical Crystallography.<sup>37</sup> If properly integrated into devices, they can be active elements in soft and lightweight actuators, with values of force-to-weight ratio comparable or even superior to

those typical of some living creatures. Also in this case, the preparation of the new materials can be aided by a crystal engineering approach. For instance, a requirement for thermosalient crystals<sup>38</sup> (where the macroscopic mechanical effect is produced after a single-crystal-to-single-crystal transition, and so it is related to heat being absorbed by the crystal) is the presence of a network of strong directional intermolecular bonds (H-bonds, halogen bonds) so as to produce a very fast reconfiguration during the SCSC transition, with fast accumulation of internal strain that is promptly released producing the mechanical response of the crystal. The present PhD thesis project aims to investigate possibilities of the crystal engineering approach by exploiting its principles for the design and synthesis of new organic molecules or organic-inorganic hybrids that are potentially interesting for several advanced applications. At the same time, interesting aspects of solid-state chemistry, such as the polymorphism and the tautomerism of some systems, have been studied and explained. More specifically, the systems that will be shown in the next chapters will include fused-ring heteroaromatic systems for the realization of 2D-coordination network polymers with a perovskite-like motif; new N-rich fused-ring heterocycles, which proved to be very versatile depending on the application field; materials that crystallize in acentric polar space groups for NLO applications, and dynamic crystals.

## Chapter 2 Fused-Ring Heteroaromatics

### 2.1 General aspects

Since the historical publication of the three-dimensional Fourier maps of naphthalene and anthracene at the half of the XX century, fused-ring aromatics are widely used in structural chemistry.<sup>39,40</sup>

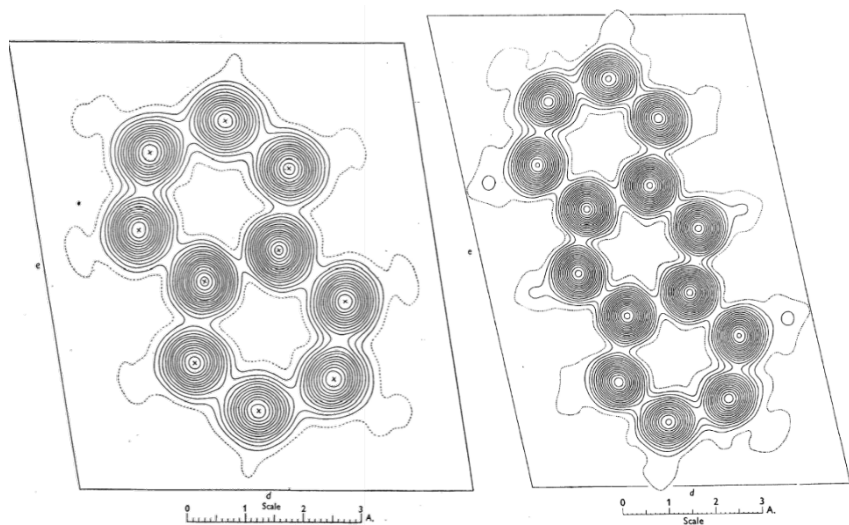
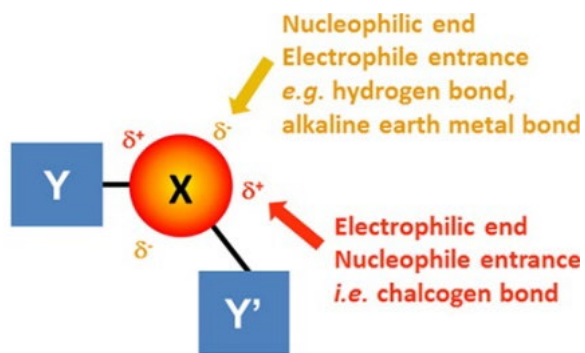


*Figure 3 Two landmarks of structural chemistry: crystal sections through the molecular plane of the three-dimensional Fourier map of naphthalene (left) and anthracene (right) molecules. Each contour line represents a density increment of  $\frac{1}{2} e.A.^{-3}$ , the half-electron line being dotted. Figures are taken from ref 39 and 40.*

The main result that has gradually emerged from the packing analysis of fused-ring aromatic hydrocarbons is the recognition of the face-to-edge and face-to-face motifs as the basic synthons in their packing. Despite the plenty of different fused-ring aromatic hydrocarbons, few different packing modes are observed. Desiraju and Gavezzotti rationalized the crystal packing in four basic packing modes adopted by the hydrocarbons, mainly in dependence on the number and type of rim H atoms.<sup>41,42</sup> In recent years, the semiconducting properties of fused ring aromatics have gained a great deal of interest. For anthracene<sup>43</sup>, pentacene<sup>44</sup> and picene<sup>45</sup> hydrocarbons and their derivatives, good hole/electron transport

properties and field-effect transistor (FET) behaviour have been measured. The introduction of heteroatoms in fused-ring aromatics has the effect of modulating the HOMO-LUMO gap and the electron/hole transport properties.<sup>46,47</sup> However, the introduction of heteroatoms can also change the fundamental paradigm of the packing, through new and powerful interactions as compared with weaker C—H $\cdots\pi$  and  $\pi\cdots\pi$  interactions of fully hydrocarbon systems. For instance, the coexistence of the elements of the 16<sup>th</sup> group (sulfur or heavier) and nucleophilic atoms can induce chalcogen bond interactions.<sup>48–50</sup> In the last decades, the study of chalcogen bonding interactions among the SBIs has obtained a growing interest because of their easily tunable strength. Chalcogen bonding can be strong enough to allow the interaction to act as an effective and robust tool in crystal engineering.<sup>51</sup> The IUPAC defines chalcogen bonding as a supramolecular interaction between an electrophilic region on a group 16 atom and electron-rich centres with typical interatomic distances intermediate between classic single bonds and the sum of van der Waals radii. This definition is in effect an extension of the definition recommended by IUPAC for the halogen bond.<sup>52</sup>



**X = O, S, Se, Te, (Po); Y, Y' = C, N, etc.**

*Figure 4. Schematic representation of the anisotropic distribution of the electron density around covalently bound chalcogen atoms and the pattern of the resulting interactions Adapted from Ref. 48.*

As shown from Figure 4, the surface electrostatic potential is more negative in the direction perpendicular to the covalent bond of the chalcogen, as in the case of the halogen bond. Consequently, the electrostatic potential is more positive in the elongated direction of the covalent bond, thus allowing nucleophile sites to establish electrostatic interaction in that area. If we move down along the 16<sup>th</sup> group, the electronic density is more anisotropic, and then, the chalcogen atom can establish a stronger interaction with a nucleophilic site. Multiple nonbonded interactions play together to produce stable and predictable specific synthons between different macromolecules such as polymeric materials. Concerning the crystal of coordination polymers with fused-ring heteroaromatics, the understanding of the nature and strength of chalcogen bond interaction on crystal packing is still an open research.

## 2.2 Study of Topochemical Reactivity and Intermolecular Interactions in Different Polymorphs of Fused-Ring Heteroaromatics

Two fused-ring heteroaromatic compounds (chart 1), naphtho[2,3-*c*][1,2,5]thiadiazole (**NTD**) and naphtho[2,3-*c*][1,2,5]selenadiazole (**NSeD**), were investigated by solid-state experimental and computational analysis. The synthetic details of the compounds are reported in Appendix A

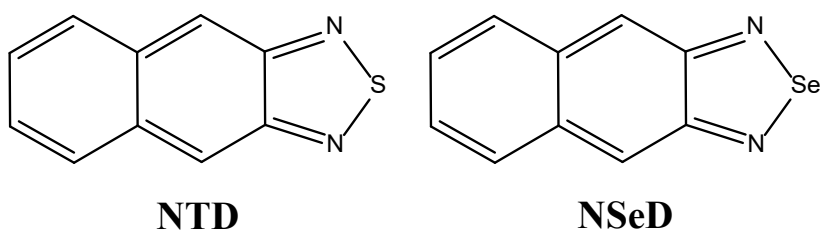


*Chart 1. Chemical Diagrams of the Two Fused-Ring Heteroaromatics studied.*

**NTD** shows three different polymorphic phases, while **NSeD** is nonpolymorphic. The different crystal packings give distinct responses in the topochemical reactivity of the compounds toward cycloaddition reactions, ranging from no reaction to the production of butterfly dimers. Crystallization of **NTD** from different solvents and conditions has led to the formation of crystals with three different morphologies, corresponding to three polymorphic phases (I, II, III Figure 5), as confirmed by XRD analysis.

i

---

<sup>i</sup> Parts of this chapter have been taken from *Crystal Growth & Design* **2020**, 20(2), 1229-1236

### 2.2.1 Analysis of crystal packing

The first polymorph, Phase I, was obtained by slow cooling to RT of a hot solution of **NTD** in hexane, giving crystals in the elongated prismatic form (Figure 5 a,b). Phase II was obtained by slow evaporation of **NTD** in heptane/dichloromethane in the form of lozenge-shaped crystals. By evaporation of an ethanolic solution of **NTD**, needle-shaped crystals of Phase III were obtained.

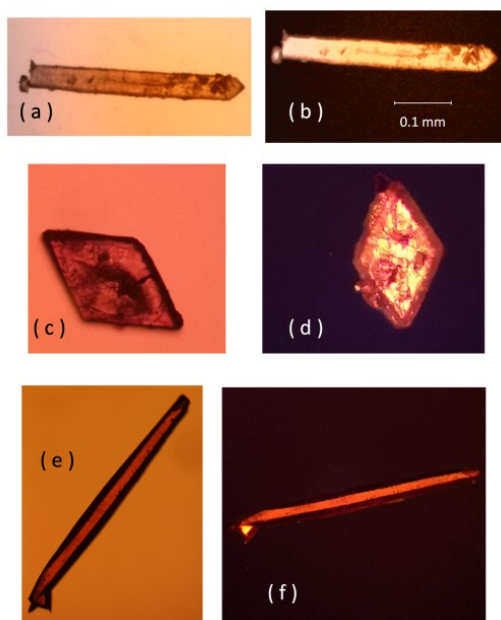


Figure 5. Pics of single crystals of different polymorphs of **NTD** taken at polarizing microscope: a) Phase I b) Phase I under crossed polarizers c) Phase II d) Phase II under crossed polarizers e) Phase III f) Phase III under crossed polarizers. The scale bar reported in b) is the same for the others.

The crystal packing of Phase I **NTD** is shown in Figure 6. There are two crystallographically independent molecules in this crystal structure, named A and B, whose mean molecular planes make a dihedral angle  $\tau$  of  $59.44(3)^\circ$ . A relevant motif present in the packing is represented by infinite chains, parallel to  $a$ , in which molecules, in alternated sequence ...ABAB..., are linked by weak H-

bonding between C-H donor and N acceptor, Figure 6a. Molecules A are placed perpendicular to the unique axis  $b$  of the unit cell. Therefore, along  $b$ , columns of parallel stacked molecules  $\cdots AAA \cdots$  are generated by translation and inversion. The stacking distance between centrosymmetrically related A molecules is  $b/2=3.533 \text{ \AA}$ . Moreover, in the crystal, molecules A keep their orientation and are always parallel to each other. B Molecules, on the other hand, are inclined with respect to the unique axis of about  $30^\circ$ ; as a consequence, in the crystal, molecules B take two different orientations, making a dihedral angle of about  $60^\circ$ ; the different orientations of the molecules are shown in the packing diagram of Fig. 6b.

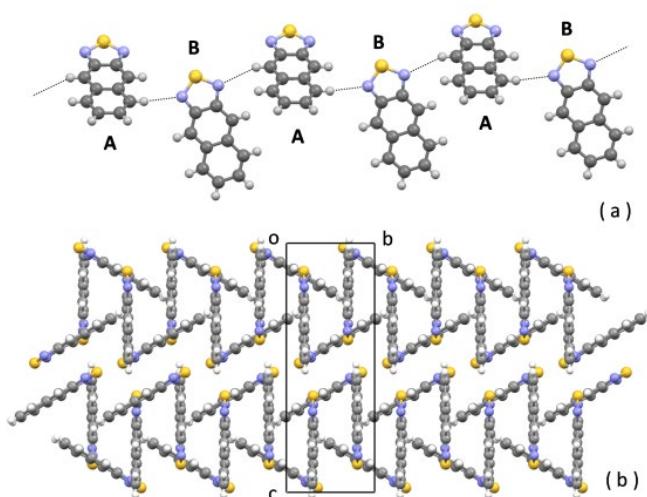


Figure 6. Packing of Phase I of **NTD**. (a) chain of molecules; (b) packing view down  $a$ .

In Phase II of **NTD**, the in-plane intermolecular contacts basically feature chalcogen bond interactions between N donor and S acceptor, with the formation of dimers across centres of symmetry (Figure 7). The  $N \cdots S$  distance is  $3.193(2) \text{ \AA}$ , and the angle  $N-S \cdots N$  is  $169.80(9)^\circ$ . This polymorph shows a sandwich-herringbone packing (Figure 7c), one of the four basic packings of fused ring

aromatic hydrocarbons, featuring face-to-edge and face-to-face close contacts. In fact, couples of parallel, centrosymmetrically related molecules are arranged in a herringbone packing. The two molecules of each couple are close to each other, and C $\cdots$ C intermolecular contacts as short as 3.357 Å are observed.

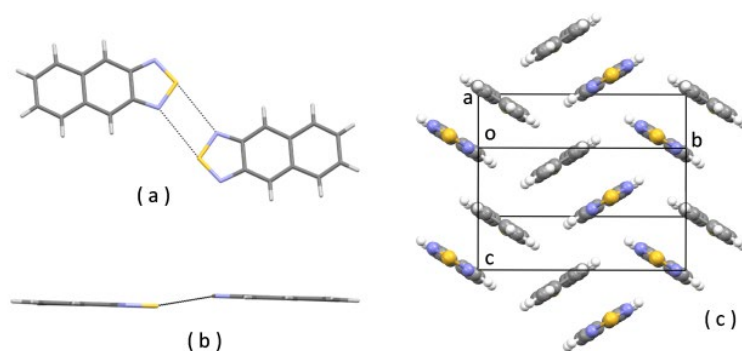


Figure 7. Crystal Packing of Phase II of **NTD**. (a) Front View of a chalcogen-bonded dimer; (b) edge view of a chalcogen-bonded dimer; (c) packing viewed down  $a+c$ .

The most relevant in-plane intermolecular contacts in the packing of Phase III of **NTD** are basically the chalcogen bonds between N and S (Figure 8 a,b). As in Phase II, they are formed across crystallographic inversion centres, leading to the formation of dimers. The N $\cdots$ S distance is 3.247(2) Å, and the angle N-S $\cdots$ N is 160.52(7)°. The packing of Phase III (Figure 8c) shows layers of parallel stacked molecules that are piled up along  $b$  with alternated orientation, in a zig-zag fashioned motif (the angle of zig-zag is about 50° and is related to the angle of about 25° that the independent molecule makes with the unique axis  $b$ ).

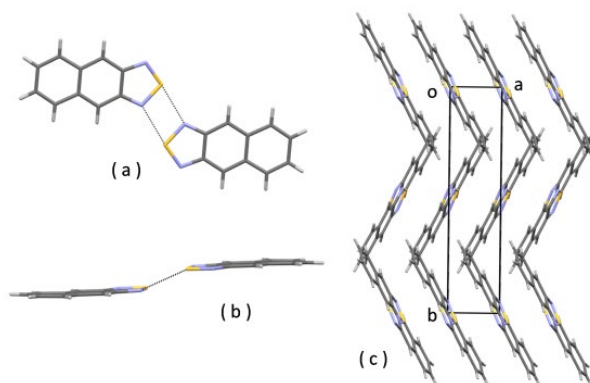


Figure 8. Crystal packing of Phase III of **NTD**. (a) front view of a chalcogen-bonded dimer; (b) edge view of a chalcogen-bonded dimer; (c) packing viewed down *c*.

The distance between the translationally related parallel stacked molecules in the layers is higher than in II, with C $\cdots$ C close contacts of 3.464 Å.

The packing of **NSeD** shows a predominance of chalcogen bond interactions, according to the more powerful acceptor capacity of Se compared with S.

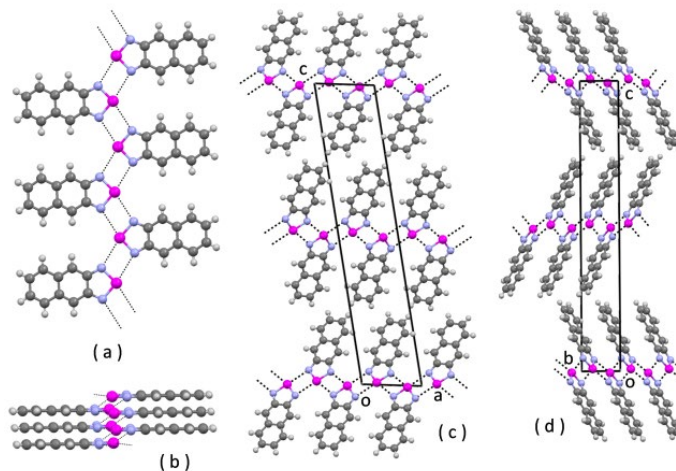


Figure 9. Crystal packing of **NSeD**. (a) front view of a chalcogen-bonded ribbon; (b) edge view of a chalcogen-bonded ribbon; (c) packing viewed down *b*; (d) packing viewed down *a*.

In fact, while in Phase II and III of **NTD** only one N atom of the molecule is involved in the chalcogen bond and dimers are formed, in the case of **NSeD** both N atoms are involved with Se acting as bifurcated acceptor. This leads to the formation of infinite ribbon-chains of molecules linked by chalcogen bonds across inversion centres (Figure 9 a,b). The chains are parallel to the crystallographic direction **a+b**. In this way, each molecule is involved in four chalcogen bonds instead of two as in Phase II and III of **NTD**. The N...Se distances are 2.890(2) Å and 3.005(2) Å, significantly shorter than in the case of S, notwithstanding the higher van der Waals radius of Se, and the angles N-Se...N are 167.63(9)° and 160.67(8)° respectively. The ribbons of chalcogen-bonded molecules form layers in the plane (**a,b**), which are piled up along **c** in alternated orientation, Figure 9 (c) and (d). Within each layer, molecular planes are parallel to each other, and face-to-face interactions are present.

### 2.2.2 Analysis of Chalcogen Bonding Interactions

In the CSD, few crystal structures of 1,2,5-thiadiazoles and 1,2,5-selenadiazoles contain the ribbon motif as shown in Figure 9a. Otherwise, the ribbon motif is more common for 1,2,5-telluradiazoles (10 structures out of 22 of CSD, i.e., 45%), and it is consistent with the higher interaction energy of N...Te chalcogen bond.<sup>53,54</sup>

In order to estimate the energy of the chalcogen bonding intermolecular interactions (S...N and Se...N), computational analysis was carried out in the framework of the optimization of the crystal phases with the program CRYSTAL17.<sup>55</sup> This was accomplished in the following way: from the optimized crystal structure of actual Phase II of **NTD** and virtual phase II of **NSeD** two dimers, in which two chalcogen bonds are present, have been extracted. The Phase I and Phase III of **NTD** were not considered because chalcogen bonds are not present in Phase I and in Phase III the S...N distance of the chalcogen bond is slightly longer than in Phase II. The difference between the energy of the dimer

and the sum of the energy of the two isolated molecules were calculated using DFT B3LYP level with a 6-31G\*\* basis set (APPENDIX B for computational details). The difference was divided by two, because the dimers feature two chalcogen bonds, and this result, indicated by  $E_{\text{ch}}$ , can be considered as a measure of the energy of the chalcogen bond in the investigated systems. The results are shown in Table 1.

*Table 1. Evaluation of the energy of the chalcogen bond from the optimized crystal structures.*

	S $\cdots$ N in II of <b>NTD</b>	Se $\cdots$ N in II of <b>NSeD</b>
$E_{\text{ch}}$	-2.54 kcal/mol	-4.90 kcal/mol

Energies are negative because the energy of the chalcogen bonded dimer is less than the sum of the energies of two isolated molecules. In another approach, the energy of intermolecular interactions was evaluated with CrystalExplorer17.<sup>56</sup> In this program, the first step is to build a portion of the crystal structure, *i.e.* a cluster of molecules surrounding a given one and whose barycentres are within 3.8 Å from the central molecule. Then the molecular wavefunction is calculated (in this case at level HF/3-21G because it is the only one supporting Se) and the interaction energies between the central molecule and the other molecules of the cluster. Concerning the chalcogen bonding interactions, the results are reported in Table 2.

*Table 2. The energy of the Chalcogen Bond from the Application of CrystalExplorer17.*

	S $\cdots$ N in II of <b>NTD</b>	S $\cdots$ N in III of <b>NTD</b>	Se $\cdots$ N in <b>NSeD</b>
$E_{\text{ch}}$	-3.3 kcal/mol	-3.01 kcal/mol	-5.33/-6.5 kcal/mol

It is interesting to note that the two approaches produce similar results in the relative strength of Se $\cdots$ N vs S $\cdots$ N chalcogen bond, indicating that with Se the chalcogen bond is about two times stronger than with S. Also the absolute value of the energy of the interaction is similar in the two approaches and is similar to

the values reported in the literature.<sup>54</sup> In particular, the energy of the stronger chalcogen bond, i.e.  $\text{Se}\cdots\text{N}$ , estimated to be about 5-6 kcal/mol, can be compared with the energy of a strong H bond,  $\text{N-H}\cdots\text{N}$ , which was estimated as 8.4 kcal/mol in literature.<sup>57</sup> Hirshfeld fingerprint plots of the three polymorphs of **NTD** and **NSeD** are reported in Figures 10-12. They were calculated using the program *CrystalExplorer17*. The fingerprint plots of the two independent molecules of Phase I of **NTD** are shown in Figure 9. The weak H bonding  $\text{C-H}\cdots\text{N}$  is evidenced by the two spikes above (molecule A) and below (molecule B) the principal diagonal, at about (1.1, 1.5) and (1.5, 1.1) respectively. The presence of only one spike in each plot is related to the fact that the donor is provided by molecule A and the acceptor by molecule B.

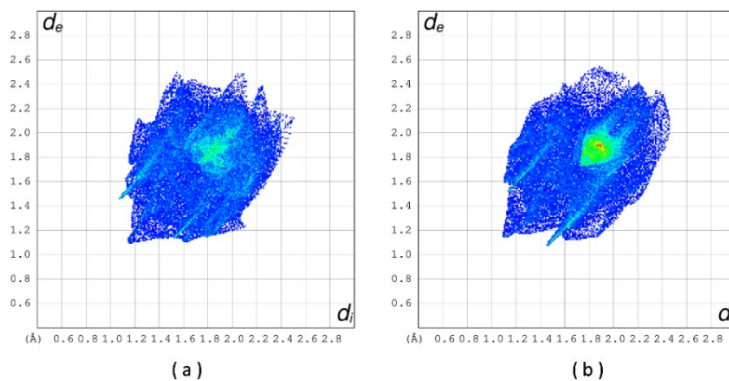


Figure 10. Hirshfeld Fingerprint Plots. (a) Independent Molecule A of **NTD** Phase I; (b) Independent Molecule B of **NTD** Phase I.

The plots of phases II and III of **NTD** are shown in Figure 10. The sting along the principal diagonal down to (1.0, 1.0) is related with frontal  $\text{H}\cdots\text{H}$  contacts. The wings, symmetrically placed with respect to the principal diagonal, are related with  $\text{C-H}\cdots\pi$  interactions and are much more evident in II. The chalcogen bonding interactions  $\text{N}\cdots\text{S}$  are evidenced by the thin green stripes parallel to the

principal diagonal down to (1.7, 1.4)/(1.4, 1.7). They are present both in II and III and are more pronounced in II.

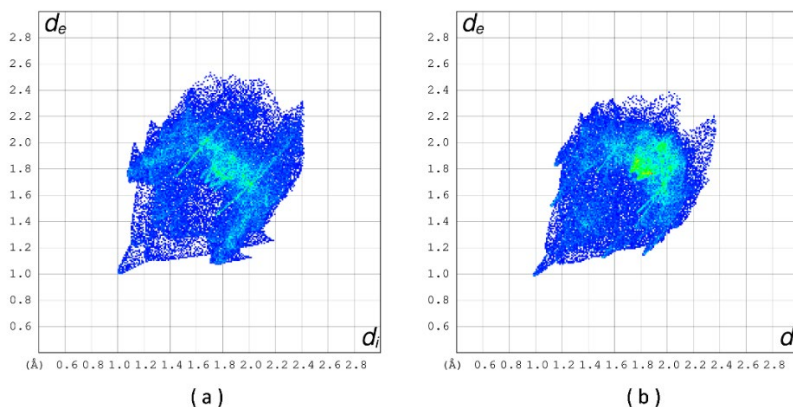


Figure 11. Hirshfeld Fingerprint Plots. (a) Phase II of **NTD**; (b) Phase III of **NTD**.

In the case of **NSeD** (Figure 12), the thin green stripes related with the chalcogen bond interactions  $\text{N}\cdots\text{Se}$  are more evident and they go down to (1.6, 1.3)/(1.3, 1.6).

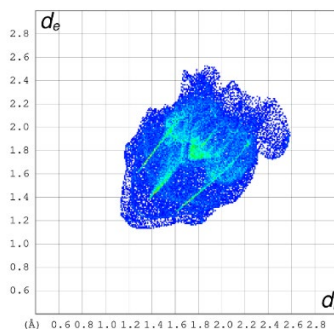


Figure 12. Hirshfeld fingerprint plot of **NSeD**.

In Table 3, the different intermolecular interactions present in the crystal phases of **NTD** and **NSeD** and the correspondent fraction of the Hirshfeld surface are reported.

Table 3 Amount of Hirshfeld surface due to different interactions for the three polymorphs of **NTD** and for **NSeD**.

	H···H	H···C	C···C	N···S/Se
<i>NTD_I</i>	30.9 %	14.3 %	5.9 %	
<i>NTD_II</i>	23.3 %	24.7 %	7.6 %	5.3 %
<i>NTD_III</i>	31 %	13.1 %	13.5 %	6.5 %
<i>NSeD</i>	38.5 %	17.7 %	8.9 %	16.3 %

### 2.2.3 Solid-State Topochemical Reactivity

Fused-ring hydrocarbons and fused-ring heteroaromatics have been reported to undergo cycloaddition reactions.<sup>58</sup> In the present case, the crystallographic analysis of Phase I of **NTD** has suggested the possibility of cycloaddition reaction and it was confirmed by leaving a chloroform solution of **NTD** under visible light at room temperature for several days. Single crystals were obtained, and from XRD analysis, the structure of the dimer was found as shown in Figure 13, a butterfly-shaped  $C_{2h}$  geometry was observed for the dimer, henceforth named as **NTD\_bfly**. The formation of the dimer is apparently due to a  $[\pi 4_s + \pi 4_s]$ -cycloaddition.<sup>59</sup>

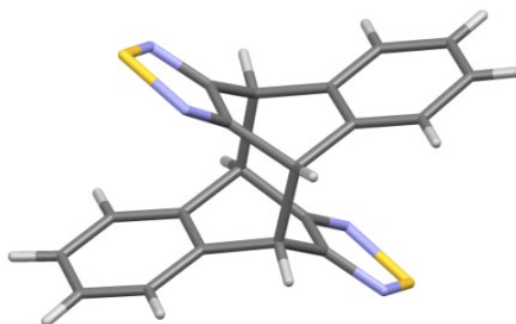


Figure 13. X-ray molecular structure of **NTD\_bfly** at 173 K.

As a result of the formation of **NTD\_bfly** dimer in solution, the possible topochemical reactivity in solid-state of the three polymorphic phases of **NTD** and **NSeD** has been investigated. The basic rules for topochemical reactions were initially proposed by Schmidt:<sup>4</sup>

- I. the stereochemistry of the dimer, in our case  $C_{2h}$  or  $C_{2v}$ , is determined by the contact geometry of the molecules in the crystal (antiparallel if molecules are related by a crystallographic centre of symmetry, parallel if they are related by translation);
- II. dimerization is possible provided the centre-to-centre distance of the double bonds involved is of the order of 4 Å ( $3.5 \text{ Å} < d < 4.2 \text{ Å}$ ), and the double bonds in the reacting molecules are strictly parallel.
- III. Other geometrical parameters have been introduced in addition to the centre-to-centre distance criterion. They involve the angles between the reactive bonds and the displacements of the reactive bonds with respect to each other.

The relative orientation of close molecules possibly involved in topochemical reactions for the three polymorphs of **NTD** is shown (Figure 14).

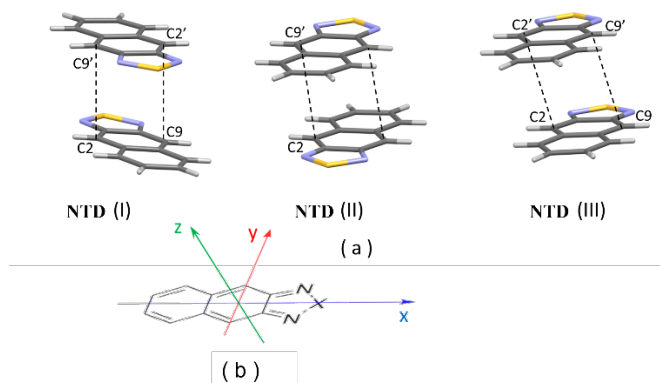


Figure 14. (a) Orientation of close molecules possibly involved in topochemical reaction for the three polymorphs of **NTD**; (b) reference system adopted for defining the relative orientation of close molecules.

In Phase I of **NTD**, there is suitable orientation and distance for cycloaddition of the independent molecules A (distance between the C atoms 3.620 Å and 3.825 Å, quasi-parallel orientation of closest centrosymmetrically related A molecules);

differently, for the independent molecules of B type the distances between C atoms are close to 7 Å. Experimentally, crystals of Phase I, irradiated with UV lamps, undergo a colour change, turning from orange to pale pink, producing a powder from which, by recrystallization from DMF, colourless single crystals of the  $C_{2h}$  **NTD**\_bfly dimer were obtained, as proved by single-crystal X-ray analysis. The dimerization yield was evaluated by NMR analysis.

Manually selected single crystals of the different polymorphs phases of **NTD** were put on microscope glass slides. The slides were placed at a distance of 2 cm from a UV lamp and directly irradiated for a time of the order of hours. The experiments were performed in a dark case (about 0.5 m<sup>3</sup>) equipped with an air ventilation system to avoid overheating. At a selected time step (6 h/24 h), an aliquot of the irradiated crystals was transferred in an NMR tube and analyzed. From these spectra, it is evident that there is a partial photodimerization for phases I II because the spectra contain both signals of the monomer and the dimer. The amount of the formed photodimer can be determined by peaks integration. The dimerization yield of Phase I is 4.3% after 6 h irradiation, and 7.0% after 24 h (Figure 15-16).

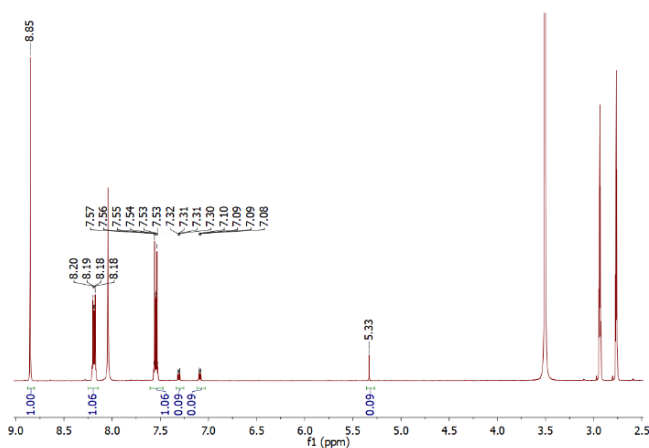


Figure 15.  $^1\text{H-NMR}$  spectrum in  $\text{DMF-d}^7$  of a phase I sample of *NTD*, after solid-state irradiation for 6 h. The signals near 2.70 ppm, 2.90 ppm and 8.03 ppm are due to residual DMF, and the signal near 3.5 ppm is due to water.

The dimer diagnostic peak is the singlet at 5.32  $\delta$  of the aliphatic methine C-H.

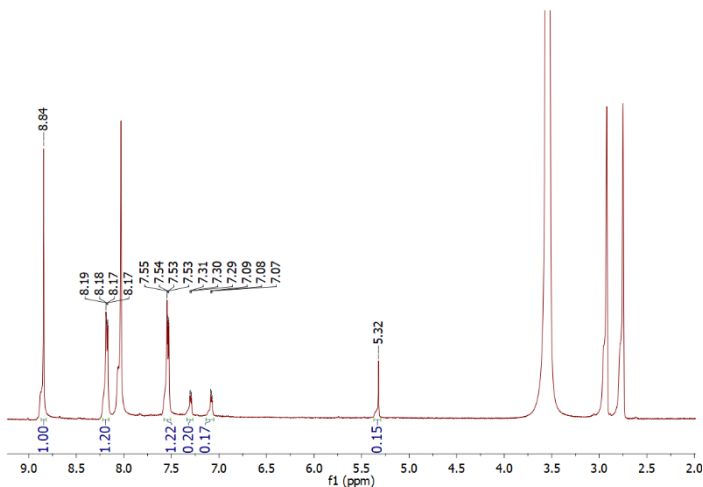


Figure 16.  $^1\text{H-NMR}$  spectrum in  $\text{DMF-d}^7$  of a phase I sample of *NTD*, after solid-state irradiation for 24 h. The signals near 2.70 ppm, 2.90 ppm and 8.03 ppm are due to residual DMF, and the signal near 3.5 ppm is due to water.

In polymorph phase II there is suitable orientation and distance for cycloaddition in the couples of centrosymmetrically related closest molecules (distance between

C atoms is 3.779 Å). Experimentally, also in this case, there is a partial dimerization with the formation of the  $C_{2h}$  isomer, as for polymorph I. In this case the yield in dimer is 5.2 % after irradiation for 18 h and 13.8 % after 24 h (Figure 17).

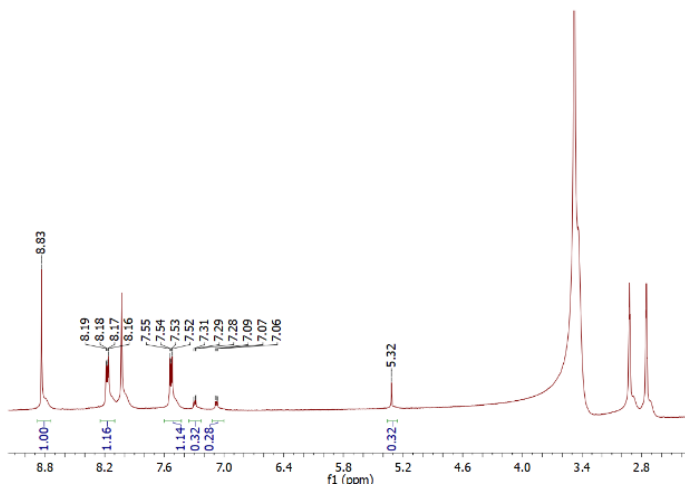


Figure 17.  $^1\text{H-NMR}$  spectrum in  $\text{DMF-d}^7$  of a sample of phase II of **NTD**, after solid-state irradiation for 24 h. The signals near 2.70 ppm, 2.90 ppm and 8.03 ppm are due to residual DMF, and the signal near 3.5 ppm is due to water.

In Phase III, stacked columns of translationally related molecules are present, with distances of 3.833 Å between relevant C atoms. Although Schmidt's rules are satisfied for the formation of the  $C_{2v}$  dimer, experimentally there is no dimerization and Phase III is photostable. In fact, after irradiation for 24 h, the sample is recovered unchanged without any detectable evidence of dimer formation in the  $^1\text{H-NMR}$  spectrum of the irradiated sample (Figure 18). In order to get further insight, it could be possible factoring the relevant intermolecular vectors of Figure 14b into their components in the reference frame that is naturally related to the symmetry point group of the molecule ( $C_{2v}$ ). Then, the x longitudinal axis is taken coincident with the  $C_2$  symmetry axis of the molecule. The y transverse axis is chosen perpendicular to  $C_2$  and in the plane of the molecule,

while the z normal axis is chosen perpendicular to  $C_2$  and in the other symmetry plane of the molecule. The results are shown in Table 4.

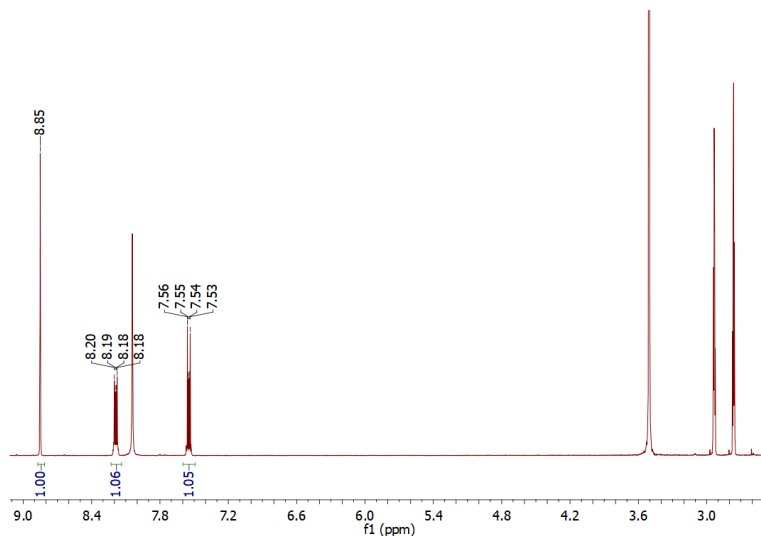


Figure 18.  $^1\text{H}$ -NMR spectrum in  $\text{DMF-d}^7$  of a sample of phase III of NTD, after solid-state irradiation for 24 h. The signals near 2.70 ppm, 2.90 ppm and 8.03 ppm are due to residual DMF, and the signal near 3.5 ppm is due to water.

Table 4 Short intermolecular vectors between atoms possibly involved in topochemical reaction, and the corresponding orthogonal components (in Å), according to the reference system defined in Figure 13.

	Interatomic vector	Longitudinal component	Transverse component	Normal component
NTD (I)	$\text{C}_2\text{-C}_9'$	$\tau_x=1.2816$	$\tau_y=-0.2122$	$\tau_z=3.5976$
NTD (I)	$\text{C}_9\text{-C}_2'$	$\tau_x=1.2808$	$\tau_y=-0.2038$	$\tau_z=3.3794$
NTD (II)	$\text{C}_2\text{-C}_9'$	$\tau_x=-1.4575$	$\tau_y=-1.0143$	$\tau_z=3.3347$
NTD (III)	$\text{C}_2\text{-C}_2'$	$\tau_x=-0.9718$	$\tau_y=1.2651$	$\tau_z=3.4850$

Apparently, the only anomalous features of phase III of NTD are the larger transverse component and the smaller longitudinal component. Moreover, the root-mean-square amplitude of molecular oscillation in the transverse direction for III (0.1418(3) Å at 173 K, 0.1795(4) Å at 293 K) is smaller as compared with

II (0.1425(3) Å at 173 K, 0.1926(7) Å at 293 K) and I (0.1548(3)Å at 173 K, 0.2036(8) at 293 K, independent molecule A).<sup>60</sup> It can also be noted that the transverse component in III is about half the length of the C2-C9 segment (2.853 Å). This means that atoms C2 and C9' of **NTD**(III) in Figure 14a lie very close to the molecular planes  $x'z'$  and  $xz$  respectively, which are nodal planes for the molecular  $\pi$ -electron density. These can be the reasons why polymorph III of **NTD** is photostable. Then, this analysis suggests that the transverse component of the intermolecular vector plays a relevant role in the topochemical reactivity. In the present case, transverse displacement components not higher than 1 Å seem mandatory for the topochemical reaction.

DSC and TGA measurements on **NTD** and **NseD** suggest that double bond opening reactions can also be thermally activated (Figure 18). Melting of **NTD** is observed at 100 °C. A broad exothermic signal follows the melting endotherm without weight loss. The sample does not show any endo/exothermic signal after cooling and heating again. This suggests that, at melting, **NTD** undergoes chemical transformation to an amorphous material. In **NSeD**, no endothermic signal related to melting is observed. The DSC curve on heating shows a very sharp exothermic signal at about 150 °C, again without losing weight. As for **NSeD**, no signal is observed on cooling and heating again. Moreover, after the exothermic signal, a single crystal of **NSeD** keeps its macroscopic shape, but completely loses crystallinity becoming amorphous, as proved by X-ray diffraction analysis, and insoluble in all tested organic solvents (acetone, chloroform, ethanol, dichloromethane, DMSO, DMF).

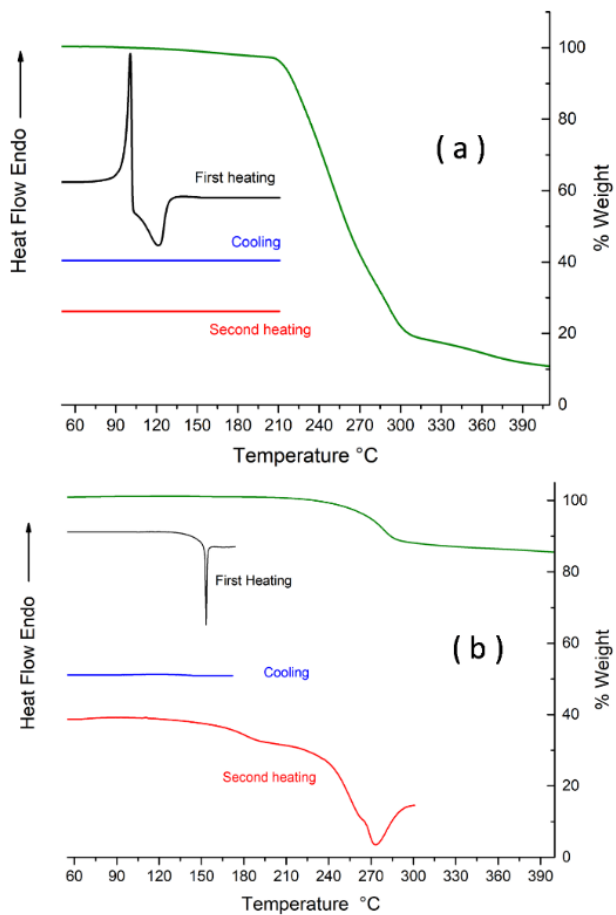


Figure 19. Combined DSC/TGA analysis for *NTD* (a) and *NSeD* (b). Scanning rate 10 K/min in flowing  $N_2$  atmosphere.

### 2.3 Effect of chalcogen bond on the packing and coordination geometry in hybrid organic-inorganic Cu(II) networks.

The easy tuneable strength of chalcogen bonding interaction in dependence of the chalcogen atom leads not only to interesting features in the crystal packing of polymorph, but it could also affect the coordination geometry of organic-inorganic hybrid materials.

Based on the previous studies<sup>61,62</sup> in this research field with the employment of 1,2,5-benzothiadiazole (**btd**) and 1,2,5-benzoselenadiazole (**bsed**) (chart 1), the chalcogen bonding effect on the packing and coordination geometry of novel hybrid inorganic-organic Cu(II) networks was investigated.

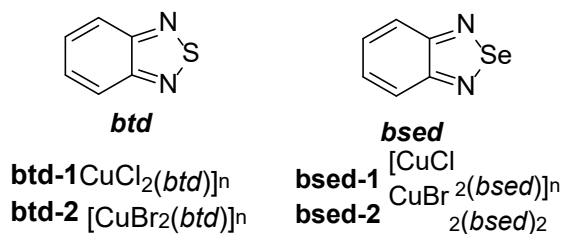


Chart 2. Chemical diagrams of the ligands and chemical formulae of the compound studied. **btd-1** poly (2,1,3-benzothiadiazole)copper(II) dichloride, **bsed-1** poly (2,1,3-benzothiadiazole)copper(II) dibromido, **bsed-1** poly (2,1,3-benzoselenadiazole)copper(II) dichloride, **bsed-2** bis(2,1,3-benzoselenadiazole-kN)dibromidocopper(II).

As nitrogen atoms of the heterocycle have the competing roles of coordinating the metal ion and forming secondary bond interactions, multiple arrangements are possible, and the overall structure will be the outcome of balance factors, such as the presence of  $\pi \cdots \pi$  aromatic stacking interactions or the relative strengths of the M-N, S $\cdots$ N and Se $\cdots$ N interactions. Each nitrogen of the organic ligand can bind two metal ions, as in the three isomeric polymeric structures of  $[\text{CuCl}_2(\text{btd})]_n$  (**btd-1**),  $[\text{CuBr}_2(\text{btd})]_n$  (**bsed-1**) and  $[\text{CuCl}_2(\text{bsed})]_n$  (**btd-2**) while in the complex  $\text{CuBr}_2(\text{bsed})_2$  (**bsed-2**) the **bsed** ligand is monocoordinated and interacts with neighbouring **bsed** molecule through the supramolecular synthon  $[\text{Se-N}]_2$ . In the

crystal structure of these compounds, the organic ligands preserve their strong face-to-face stacking interactions,<sup>63</sup> and when the free ligand reacts with copper(II) halides, an additional structure determining factor is introduced (coordination bond), leading to the construction of two-dimensional coordination polymers. On the other hand, in the complex **bsed-2**, the attachment of copper bromide to a nitrogen atom of the heterocycle enhances the electron acceptor ability of the chalcogen, reinforcing the [Se-N]<sub>2</sub> supramolecular synthon. In this way, the linear chains are further bridged through Se··N interactions to create a 2D layer. These hybrid compounds are an emerging class of magnetic materials that expand the material properties typically associated with magnets to include low density, transparency electrical insulation, and low-temperature fabrication, as well as combine magnetic ordering with other properties such as photoresponsiveness.<sup>64</sup>

### 2.3.1 Crystallographic and computational analysis

In order to obtain single crystals useful for X-ray structural crystallographic analysis, the crystallization has been performed in a glass tube by slow diffusion of two immiscible solvents, in which the organic ligand and inorganic salt were separately solved (Figure 20). Four different solutions were layered in a slim glass tube with ligand to metal 2:1 molar ratio. Firstly, a solution composed of the ligand in chloroform (1 mL) was added to the glass tube. After that, pure chloroform (1 mL) and pure ethanol (1 mL) were layered on the organic solution. Lastly, an ethanol solution (1 mL) of copper(II) salt was slowly dropped in the tube. The resulting four layers were allowed to diffuse within each other, and the resulting solution was left undisturbed to evaporate at room temperature. Yellow plate crystals of **btd-1** and dark brown crystals of **bsed-2** were formed over a period of one week. Red Plate crystals of **bsed-1** and green plate of **btd-2** were formed over a period of two weeks. The crystals were isolated by filtration and dried in air. The crystallographic data are reported in Appendix C.

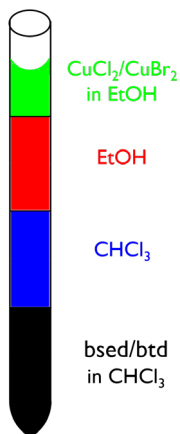


Figure 20. Hybrid crystallization method.

The crystal packing of **btd-1**, **bsd-1** and **btd-2** are shown in Figures 21-22. The three compounds are isomorphous with high crystallographic symmetry. The organic ligands occupy special positions, and the crystallographic mirror planes  $m$  of the space group ( $P2_1/m$ ) are also mirror planes of the organic ligand. In particular, these planes are perpendicular to the ligand plane and pass through the chalcogen atom (S, Se). Only one of the two symmetry planes of the isolated molecule (point group  $C_{2v}$ ) is kept as crystallographic symmetry element and then only half organic ligand molecule is independent.

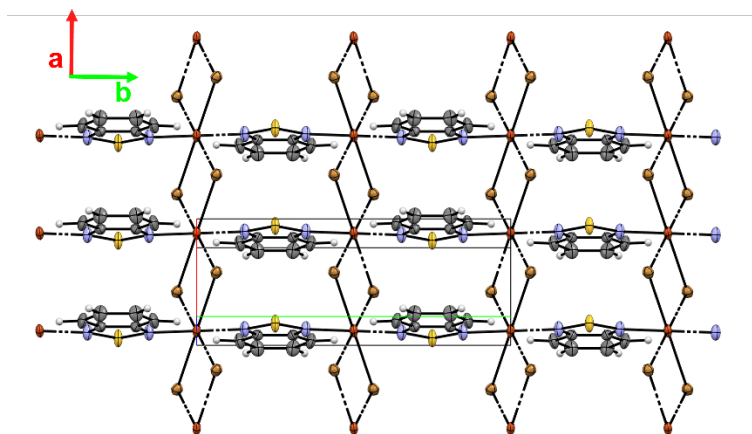


Figure 21. **btd-2** shows 2D layer in *ab* plane.

The crystal packing consists of 1-D  $\{\text{Cu}-(\mu\text{-Br})_2\}_n$  or  $\{\text{Cu}-(\mu\text{-Cl})_2\}$  linear chains running along the *a* axis linked via  $\mu\text{-btd}$  or  $\mu\text{-bsed}$  ligands along the *b* axis to afford an extended wavy 2-D layered network. For the three isomorphous complexes, the intrachain Cu  $\cdots$  Cu separations correspond to the *a* axis (**btd-1** 3.713(3) Å, **bsed-1** 3.897(3) Å and **btd-2** 3.897(3) Å) and the interchain Cu  $\cdots$  Cu separations correspond to half of *b*-axis (**btd-1** 6.277(6) Å, **bsed-1** 6.284(6) Å and **btd-2** 6.365(6) Å).

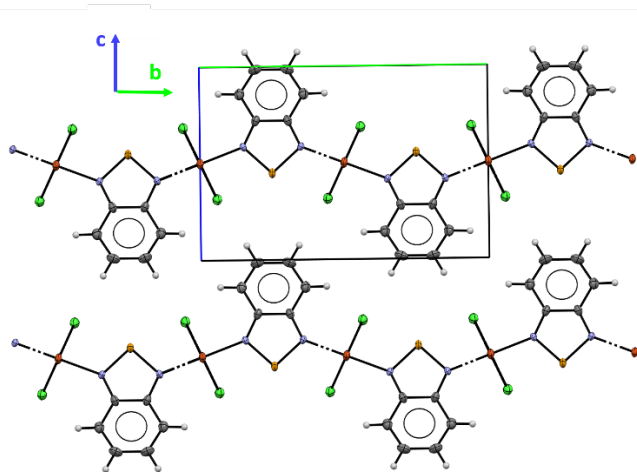


Figure 22. Packing diagram of **bsd-1**. View along *a* axis.

The Cu(II) atoms sit on inversion centres and the coordination geometry is octahedral with tetragonal distortion. The Jahn-Teller distortion is clear in the metal-halogen and metal-ligand distances, Table 5.

Table 5 Selected bond distance ( $\text{\AA}$ ) and angles ( $^\circ$ ). *a*:  $-x+1, -y+1, -z+1$ ; *b*:  $1-x, 1-y, 1-z$ , *c*:  $-1+x, y, z$ , *d*:  $-x, 1-y, 1-z$ .

<b>btd-1</b>		<b>bsd-1</b>		<b>btd-2</b>	
Cu1-Cl1	2.830(3)	Cu1-Br1	2.969(2)	Cu1-Cl1	2.277(2)
Cu1-Cl1 <sup>a</sup>	2.259(6)	Cu1-Br1 <sup>a</sup>	2.413(3)	Cu1-Cl1 <sup>a</sup>	2.833(2)
Cu1-N1	2.079(6)	Cu1-N1	2.081(6)	Cu1-N1	2.046(2)
N1-Cu1-Cl1	86.96(2)	N1-Cu1-Br1	86.98(2)	N1-Cu1-Cl1	89.77(2)
N1-Cu1-Cl1 <sup>a</sup>	89.09(2)	N1-Cu1-Br1 <sup>b</sup>	90.72(2)	N1-Cu1-Cl1 <sup>c</sup>	84.30(2)
N1-Cu1-Cl1 <sup>b</sup>	90.91(3)	N1-Cu1-Br1 <sup>c</sup>	89.28(2)	N1-Cu1-Cl1 <sup>d</sup>	90.23(2)
N1-Cu1-Cl1 <sup>d</sup>	93.04(2)	N1-Cu1-Br1 <sup>d</sup>	93.02(2)	N1-Cu1-Cl1 <sup>b</sup>	84.30(2)

Moreover, the variation of the coordination geometry around Cu(II) is strongly influenced by the strength of the chalcogen bond. In fact, comparing **btd-1** and

**bsed-1**, which differ only for the chalcogen atom, the outside shift of copper (II) atom from the organic ligand plane is higher in **bsed-1** than **btd-1**, 0.3965(5) Å and 0.2480(5) Å, respectively. Furthermore, the coordinative bond Cu-N is shorter in **bsed-1** (2.046(8) Å) than in **btd-1** (2.079(6) Å). Both the effects are cooperative to move the selenium atom of the five-membered ring closer to one of the two bridge chloride (Cl⋯S 3.358(4) Å and Cl⋯Se 3.168(3) Å). These two effects are highlighted in an increased waviness of the infinite chain along *b* axis of compound **bsed-1** (Figure 23), in according with the major strength of chalcogen bond of selenium as compared with sulphur.

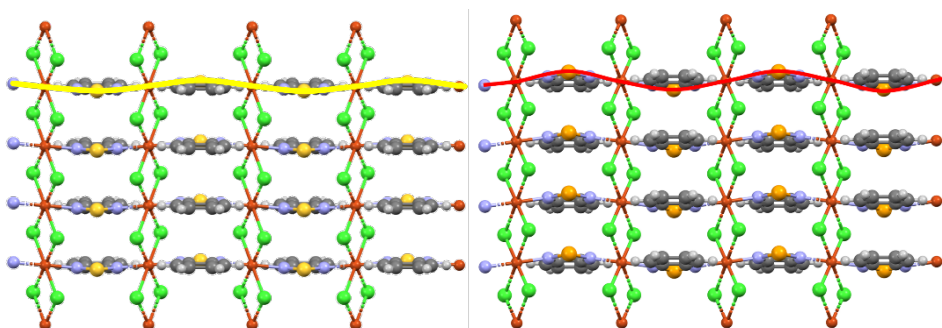


Figure 23. On the left **btd-1**, on the right **bsed-1**. Packing view along *c* axis. The yellow and red lines are plotted through each metal centre and chalcogen atom.

A characteristic structural feature common to free **bsed/btd** and the three isomorphous complexes is the existence of strong face-to-face intralayer stacking interactions between the organic ligands along *a* axis (Figures 21,24). The **btd** and **bsed** molecules form columns within the crystal lattice, with stacking distances being 3.812 Å and 3.546 Å, respectively.

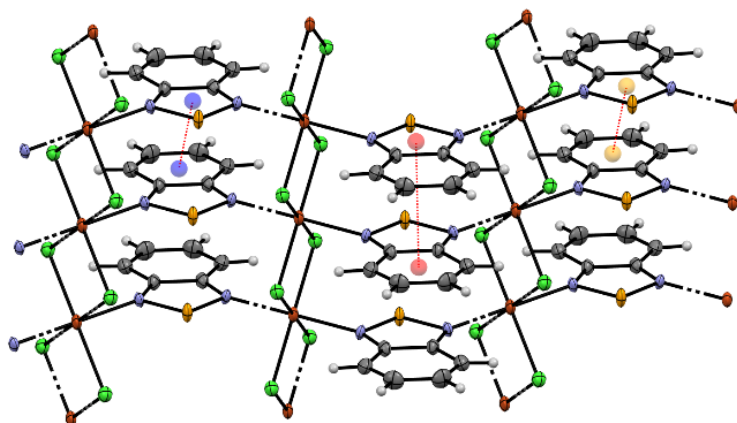


Figure 24. Side view of  $\pi \cdots \pi$  interactions between aromatic ligand molecules.

The columns of the **btd** and **bsed** molecules are oriented on alternating sides of each  $\{\text{Cu}(\mu\text{-X})_2\}_n$  chain. The organic ligands within a column stack off set such that the five-membered ring ( $\text{C}_2\text{N}_2\text{S}$ ,  $\text{C}_2\text{N}_2\text{Se}$ ) of one molecule forms  $\pi \cdots \pi$  stacking interaction with the phenyl ring of a neighbouring molecule. Within the stacks, each **btd** and **bsed** are shifted so that each chalcogen atom sits approximately over the middle of the five-membered ring below it. This is probably the reason why the interplanar distances are controlled not by the large size of the S atom but also by the common ring to ring interactions. Several 2D coordination network polymers with isostructural packing have been observed in the crystal structures of  $[\text{HgCl}_2(\text{bsed})_2]_n$ ,  $[\text{CoCl}_2(\text{btd})_2]_n$ , and  $[\text{CoBr}_2(\text{btd})_2]_n$ .<sup>65,66</sup> Complex **bsed-2** consists of 1D  $\{\text{Cu}(\mu\text{-Br})_3\}_n$  linear chains running along *a* axis and linked via  $\mu$ -**bsed** ligands along the *b* axis to afford an extended 2D layered network (Figure 25), with intralayer  $\text{Cu} \cdots \text{Cu}$  separations of 3.756(2) Å and interlayer  $\text{Cu} \cdots \text{Cu}$  separations of 10.319(2) Å. Each Cu(II) atom is pentacoordinated to 3 bromide ligands and two terminals **bsed** molecules. The Cu-Br distances are 2.396(2) Å, 2.440(2) Å, 3.010(3) Å and the Cu-N bond length is 2.000(10) Å. The **bsed** molecules within a column (*a* axis) are lightly tilted and

orientated on alternating sides of each  $\{\text{Cu}(\mu\text{-Br})_3\}_n$  and the neighbouring layers are further bridged in the second dimension through  $\text{N}\cdots\text{Se}$  interactions (Table 6).

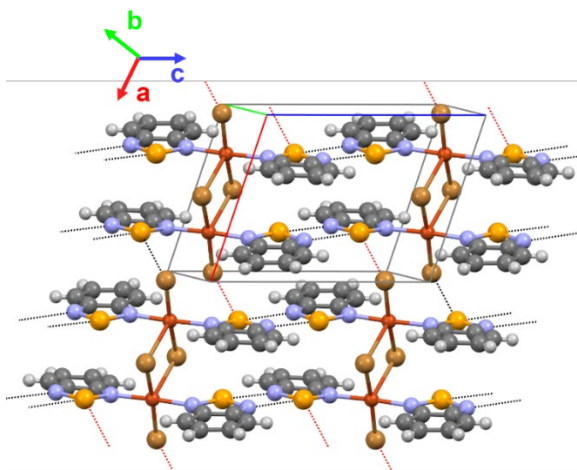


Figure 25 Crystal packing of **bsd-2**. Chalcogen bonding synthon  $[\text{Se-N}]_2$  black dashed lines, intramolecular chalcogen bonding interaction red dashed lines.

Each ligand molecule forms two complementary  $\text{N}\cdots\text{Se}$  interactions with a **bsd** molecule belonging to a neighbouring chain, giving a wave layer running parallel to the  $bc$  plane. Attachment of a Lewis acid to a nitrogen atom of the heterocycle enhances the electron acceptor ability of the chalcogen atom. This structural feature has also been observed in the crystal structure of  $[\text{MnCl}_2(\text{bsd})_2]_n$ ,  $[\text{CdCl}_2(\text{bsd})_2]_n$ ,  $[\text{HgCl}_2(\text{bsd})_2]_n$ ,<sup>67</sup> in which the chalcogen bonding effect is even stronger and manifests with the breaking of the polymeric chain network by the formation of supramolecular synthon  $[\text{Se-N}]_2$  that increases the dimensionality.

Table 6. Selected short interaction distances  $\text{\AA}$  of **bsd-2**.

Se2 $\cdots$ N1	2.944(9)
Se1 $\cdots$ N4	2.720(1)
Se1 $\cdots$ Se2	3.769(1)
N1 $\cdots$ N4	2.850(1)

The interaction density maps calculated on the difference between the crystal and the isolated molecules were performed for analysing weak bond interactions. This evaluation cannot be performed because in the crystal packing of the two systems, there is a continuous and an infinite chain  $\cdot\cdot$  **btd**—CuCl<sub>2</sub>— **btd**... (evolving in the adjacent cells). Every attempt in order to extract a single molecular cluster induces an electronic alteration of the bonds; indeed, these artefacts are generated by the arbitrary saturation of the dangling bond derived from the extraction procedure of the isolated molecule from the periodic crystal. For this reason, only the orbital values of **btd-1** and **bsed-1** have been analysed because they differ only for the chalcogen atom (Figure 26).

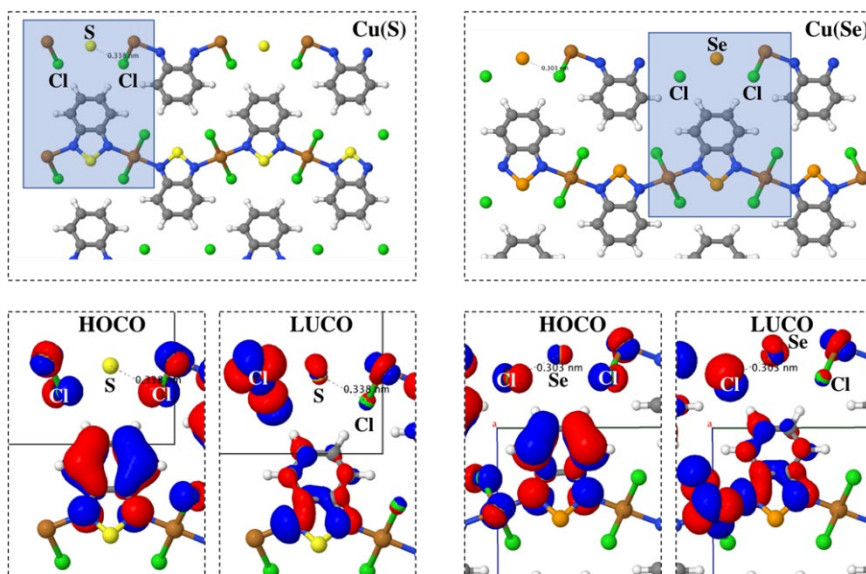


Figure 26. Top: crystal structure and electronic density maps. Bottom: **btd-1** (left) and **bsed-1** (right). For each system iso-surfaces, corresponding to 0.001 a.u., are reported for the highest occupied crystalline orbital (HOCO) and lower unoccupied crystalline orbital (LUCO).

Even if the orbital contribution is low in the Cl-S (**btd-1**) and Cl-Se (**bsed-1**) regions, the Highest Occupied Crystal Orbital (HOCO) and lowest

Unoccupied Crystal Orbital (LUCO) values in Cl-Se are higher than in the case of Cl-S. In particular, the value of HOCO around Sulphur is low, showing the lack of donor electrons. Otherwise, the compound **bsed-1** shows higher values of both HOCO and LUCO in the Cl-Se region. This feature allows supposing for compound **bsed-1** the constitution of a weak interaction like chalcogen HOCO-LUCO bond.

The vibrational properties can contribute to a meaningful interpretation of the Se-Cl interaction in terms of vibrational shifts. Calculated IR vibrational spectra are in accordance with calculated orbital values and crystal packing evidence. As shown in Figure 27, the difference of the main peaks between vibrational spectra of **btd-1** in black, **bsed-1** in red could be due only to the chalcogen mass. In fact the two systems are very similar and they differ only for the greater mass of the Selenium, inducing the red-shifting of some vibrational features. For this reason, the third spectrum in dotted blue line has been calculated in which the sulphur mass in compound **btd-1** is substituted with Selenium one, and it shows a quite overlapping band with pure compound **btd-1**. This isotopic substitution of the Sulphur (using the Selenium mass) is useful to separate the red-shifting effect due to the mass changing from the effect of electronic interaction derived from the chalcogen interaction. The main peaks of the spectra are not altered when the mass changes are performed. The peak at  $804\text{ cm}^{-1}$  (the most normalized intensity) are not affected by the isotopic substitution and it is strongly shifted ( $767$  versus  $804\text{ cm}^{-1}$ ) when the Selenium is present. So the difference between the black and red spectra is not due only to different masses but to slightly different bond patterns.

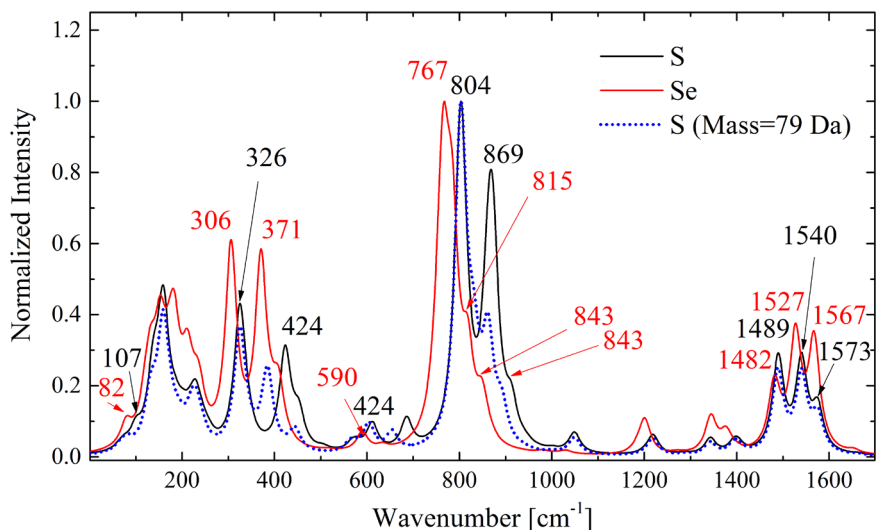


Figure 27. Calculated IR spectra of *btd-1* (black line), *bsd-1* (red line) and *btd-1* (blue dotted line), where the mass of sulphur has been substituted with the selenium one.

### 2.3.1 Preliminary Magnetic Characterization and Further Development

These hybrid coordination polymers are molecule-based magnetic<sup>68</sup> compounds exhibiting a spontaneous magnetization below a critical temperature ( $T_c$ ) and the coexistence of different magnetic orders. The goal is to establish the relationship between antiferromagnetic (AFM) and ferromagnetic (FM) orders in these compounds, possibly due to the presence of chiral spin order as observed in full-inorganic anhydrous cupric halides parent compounds. In the framework of 2D van der Waals magnets, they exhibit many important technological features like the modulation/tuning via coordination chemistry methodologies of their properties. High magnetization, electrical polarization, sensitivity to visible spectra and semiconducting behaviour are common, and just recently single-phase multiferroic in  $(C_6H_5C_2H_4NH_3)_2CuCl_4$  crystal was observed.<sup>69</sup> In this framework, these hybrids system could exhibit a spontaneous magnetization below a critical Curie Temperature ( $T_c$ ) while a Curie tail is seen at lower temperature.

Preliminary measurements of the magnetic susceptibility with an Oxford VSM Maglab on powders of **btd-1** confirm the experimental evidence in ref. 65: a broad maximum is observed at ca. 40 K, while a Curie tail is seen at 11 K (Figure 28). This effect provided by the axial bonding (via the chloro-bridges) should be negligible due to the low unpaired electron density along the  $d_z^2$  orbital in the axially elongated octahedral coordination around the  $\text{Cu}^{2+}$  atoms. Studies on the anhydrous  $\text{CuCl}_2$  and  $\text{CuBr}_2$  parent compounds, characterized by 1D-AFM behaviour, demonstrate a competition between FM nearest-neighbour and AFM next-nearest-neighbour spin-exchange interaction along the copper halide linear chain, stabilizing a helimagnetic ground state below 24 K and 73 K, respectively.<sup>70</sup> The spin spiral order propagates along the  $\text{CuCl}_2$  ribbon chain, but a spin flop is observed by applying a magnetic field along with them.

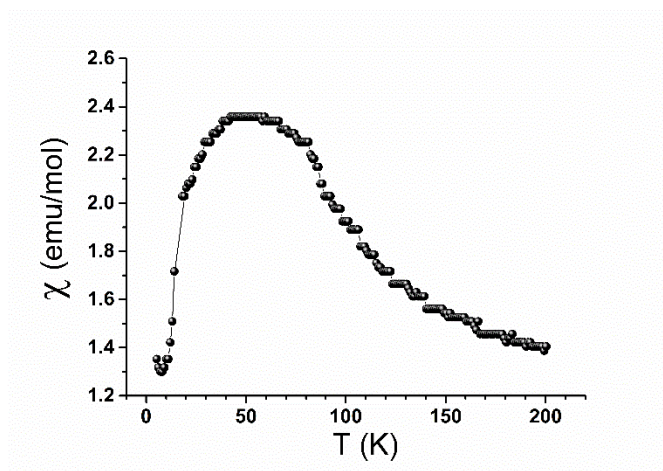


Figure 28. Plots of  $\chi_M$  vs  $T$  for a powder sample of **btd-1**.

Further developments on these systems likely to solve the electronic and magnetic properties demonstrating the presence of ferromagnetic in the 1D  $\{\text{Cu}-(\mu\text{-Cl})_2\}_n$  linear chains and/or weak ferromagnetic between the planes and deepening the presence of a frustrated antiferromagnetic inside the plane. Soft X-ray absorption spectroscopy could be an ideal tool to study the magnetic properties of 3d

transition metal compounds. In particular, circular dichroism can be used to probe the ferromagnetic order, while linear dichroism can be related both to anisotropic orbital occupation and to spin ordering in antiferromagnetic ordered samples.

## Chapter 3 N-Rich Heterocyclic Compounds

### 3.1 General aspects

Heterocyclic compounds, and nitrogen-rich hetero compounds, are widespread in nature and play numerous roles in the physiology of living organisms. They are present in vitamins, amino acids (proline, histidine and tryptophan), in biologically active compounds<sup>71</sup> such as chlorophyll and heme (structurally consisting of derivatives of porphyrins rings), in medicines (including anti-inflammatory, antimalarial, antimicrobial, antiviral, antidiabetic), synthetic agrochemicals (herbicides and insecticides) and natural bioactive substances such as alkaloids, caffeine, etc.

It is undoubtedly worth emphasizing the importance they have both as biological molecules constitutive of DNA and RNA, and at the same time, the emerging use of N-rich aromatics as building blocks for the construction of conjugated active molecules usable in various fields of advanced materials: semiconducting polymers<sup>72</sup>, organic field-effect transistors<sup>73</sup>, fluorescent sensors<sup>74</sup>, organic solar cells<sup>75,76</sup> and high-energy-density compounds<sup>77,78</sup>.

An intriguing and peculiar feature of many heterocyclic systems with high nitrogen content is tautomerism. Two compounds are defined as “tautomers” when they are constitutional isomers and they interconvert into each other by means of a chemical reaction called “tautomerization reaction”.<sup>79</sup> Tautomerization reactions usually involve the relocation of a single hydrogen atom, which is why they are typically associated with molecules containing acidic functional groups. This is significant with respect to crystal engineering: the position of a hydrogen atom in the molecule is of great importance to determine its capability to form hydrogen bonds, and so regarding to synthon formation and hence to the packing. Generally, tautomeric systems are such that one tautomer has higher relative stability than all the others which means that only one of them will be observed in the solid-state. In fact, they are very difficult to separate because, unlike other

types of isomers, they are in mobile equilibrium with each other and, in most of the cases, a mixture of all possible tautomeric forms is eventually recovered. The relative stability of the different forms is what determines the composition of the mixture: the more stable one form is, the more abundant it will be. Nonetheless, it is possible to shift the equilibrium towards one form over the others by altering the physico-chemical conditions. Quasi-degenerate tautomers are a fascinating occurrence. In this case, in fact, the equilibrium mixture contains appreciable amounts of all tautomers. Crystallization is one of the few ways to separate different tautomers because it is improbable to observe different tautomeric forms in the same crystal structure.<sup>80</sup> For quasi-degenerate tautomeric systems, co-crystallization of two tautomers in the same lattice is a possibility, but still a rare phenomenon; another possibility is the precipitation of different crystal forms, each with its own tautomer. These two occurrences account for no more than 0.5 % of molecules in the Cambridge Structural Database, which is another reason why quasi-degenerate tautomeric systems are particularly interesting. Several tautomeric systems have a high energy difference, about  $>3 \text{ kcal mol}^{-1}$ , and basically, only one form is dominant in solution and found in the crystals. However, in some cases, a tautomer with a higher energy is isolated in solid-state due to packing effects. By the way, the necessary but not sufficient condition to observe different tautomers in the solid-state is to reduce the difference in energy.

### 3.2 New Versatile N-Rich Heterocycle Ligand

Nitrogen-rich aromatic heterocycles where acidic N-H groups and basic N atoms coexist can exhibit tautomeric behaviour.<sup>81-85</sup> A correct interpretation of the chemical (and possibly even biological) behaviour of this class of compounds requires a good understanding of the factors that determine the relative stability of all tautomeric forms. The [1,2,4]triazolo[3,2-c][1,2,4]triazole fused-ring heterocycle is a particularly interesting system because of its rich tautomeric feature with several tautomeric forms (Chart 3).<sup>ii</sup>

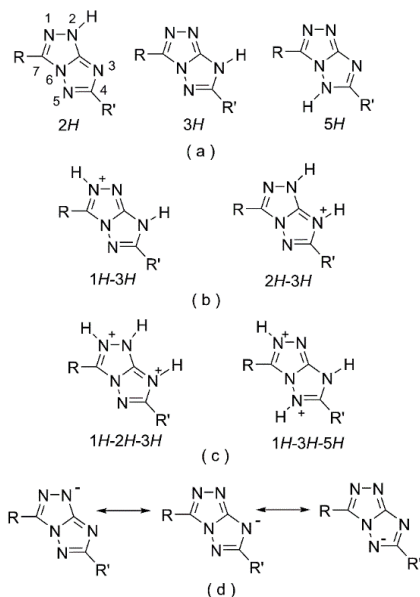
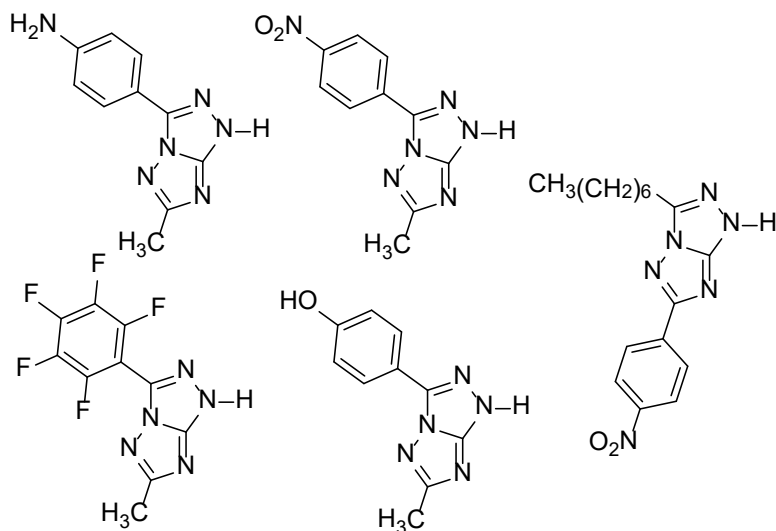


Chart 3. Chemical diagrams of triazolo-triazole compounds. (a) the three tautomers of the neutral compound; (b) the two most stable tautomers of the singly protonated species (only one canonical resonance form is shown); (c) the two most stable tautomers of the doubly protonated species (only one canonical resonance form is shown); (d) the three canonical resonance forms of the deprotonated species.

<sup>ii</sup> Parts of this chapter have been published in *Dalton Trans.*, 49, 14452-14462

Several triazolo-triazole systems were synthesized and characterized by my research group (Scheme 1).

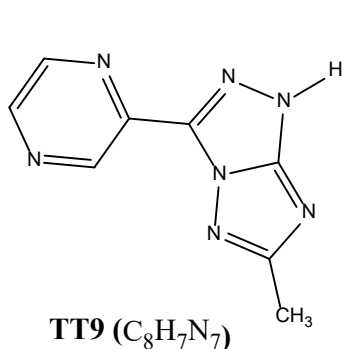


*Scheme 1 Triazolo-triazole fused-ring studied. Ref 81 and 82.*

The relative energy of the three tautomers of the neutral molecule can be significantly modulated by acting on the electronic character of the substituent in position 7 or/and on solvent polarity. In all the cases investigated before, the *2H* tautomer is always the most stable, while, for the singly protonated species, the two tautomers *1H-3H* and *2H-3H* have energy close to each other and their order can be reversed depending on the substitution pattern.<sup>82,83</sup> In some cases, the calculated energy of the *3H* tautomer is greater than *2H* tautomer by less than 1 kcal mol<sup>-1</sup>, but despite that, the *3H* tautomer has never been detected in the solid-state before for any of the triazolo-triazoles fused-ring investigated up to now.

Another attractive feature of this system is its amphoteric acid-base character. The acidity of the heterobicycle N-H proton, which can be modulated by the substitution at position 7, is remarkable, in some cases approaching the acid strength of carboxylic acids.<sup>83</sup> With the purpose of exploring the role of the

interaction with metals on the tautomeric behaviour of triazolo-triazole, a new derivative, henceforth compound **TT9** (Chart 4), has been synthesized and deeply characterized. The experimental work has been supported by computational analysis of the relative stability of the different tautomeric forms.



- 1  $C_8H_7N_7 \cdot ^{++}O_2$
- 2  $(C_8H_8N_7)Cl$
- 3  $(C_8H_9N_7)ZnCl_4$
- 4  $(C_8H_9N_7)SnCl_6 \cdot 2H_2O$
- 5  $Na(C_8H_6N_7)(H_2O)_3$
- 6  $Cu_2(C_8H_7N_7)_2Cl_4 \cdot H_2O$
- 7  $Zn_2(C_8H_7N_7)_2(H_2O)_6(Zn_2Br_6)_2 \cdot 2H_2O$
- 8  $[CuBr(C_8H_7N_7)_2(H_2O)]Br \cdot 3H_2O$
- 9  $[ZnBr_2(C_8H_7N_7)_2] \cdot H_2O$

Chart 4. Chemical diagram of 4-methyl-7-(pyrazin-2-yl)-2H-[1,2,4]triazolo[3,2-c][1,2,4]triazole (TT9) and chemical formulas, with numbering of the compound studied.

Compound TT9, a pyrazine residue is attached to the heterobicycle in position 7, has the highest N content (48.7 % by weight) within the similar compounds already studied. In this system, the study of the protonation sites is more attractive because the two nitrogen atoms of the pyrazine group must also be considered, in addition to those of the heterobicycle. Moreover, the ortho N atom of pyrazine should enhance the ligand properties of TT9, allowing for the formation of chelate complexes both for the neutral and deprotonated form. Different chelation modes can be expected depending on the conformation of the molecule, and, in the case of the neutral ligand, the formation of chelate complexes could also influence the relative stability of the tautomers.

### 3.2.1 Analysis in solution

**TT9** absorption spectra recorded at different pH values show a significant dependence on the pH: by increasing pH a bathochromic shift is observed, and  $\lambda_{\max}$  increases from 286 nm to 334 nm in the  $0.6 < \text{pH} < 12$  range. This is probably related to the high resonance stabilization of the deprotonated anion (Chart 4). In fact, the presence of electron-withdrawing groups in position 7 of heterobicycle increases the bathochromic shift, in compliance with the ref. 81. The two equilibria of Table 7 can account for the changes in the absorption spectra: neutral **TT9** (HL) can accept one proton, forming the cationic species  $\text{H}_2\text{L}^+$ , and can release one proton, forming the species  $\text{L}^-$ . In figure 29 are reported the spectra at different pH.

Table 7 Acid Constants, in the form of pKa, for **TT9** (HL). The constants are measured at  $T = 25^\circ\text{C}$ , in NaCl 0.5 M/ethanol 4% (v/v).

Equilibrium	pKa
$\text{H}_2\text{L}^+ + \text{H}_2\text{O} \rightleftharpoons \text{H}_3\text{O}^+ + \text{HL}$	$\text{pKa}_1 = 0.98(3)$
$\text{HL} + \text{H}_2\text{O} \rightleftharpoons \text{H}_3\text{O}^+ + \text{L}^-$	$\text{pKa}_2 = 5.85(3)$

The data in Table 7 show that **TT9** can be classified among the most acidic organic compounds in which Nitrogen delivers the acidic proton instead of Oxygen. The  $^1\text{H-NMR}$  spectra of **TT9**, in which the resonance signal of the N-H proton is shift to higher ppm (Appendix A), is in agreement with the remarkable acidity of the neutral. The equilibrium involving the formation of the diprotonated species was not observed in the pH interval studied,  $0.6 < \text{pH} < 13$ .

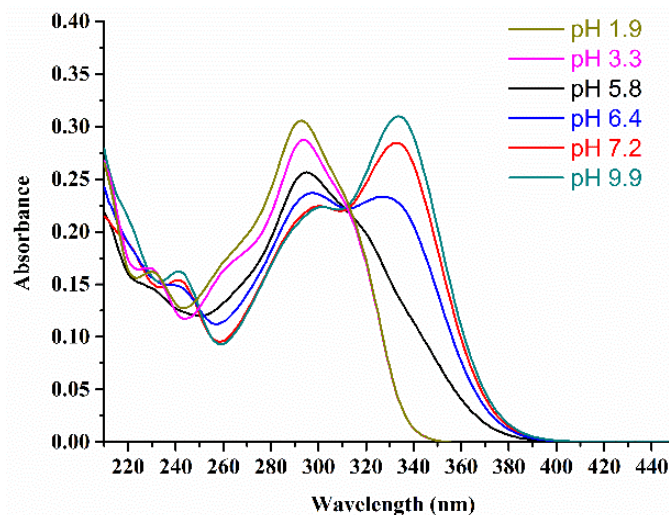


Figure 29. UV-vis absorption spectra of **TT9** at constant total concentration,  $C_M = 3.0 \times 10^{-5} M$ , in NaCl 0.5 M/ethanol 4% (v/v) recorded at  $0.6 \leq \text{pH} \leq 9.9$ .

### 3.2.2 Crystallographic and computational analysis

The complex tautomeric behaviour of the triazolo-triazole system has been further investigated by considering the effect of metal coordination on the selection of tautomers. The presence of the 2-pyrazinyl group in position 7 of the bicycle allows for the formation of chelate complexes and introduces a conformational variability between *s-trans* and *s-cis* conformers (chart 5).

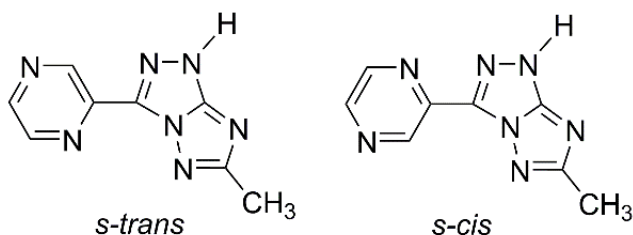


Chart 5. The two planar conformers of 2H tautomer of **TT9**.

A preliminary computational analysis of the relative stability of the different tautomeric forms of **TT9** was performed and the obtained results well compare with the previously reported data on similar compounds.<sup>82,83,85</sup>

Table 8 shows that the most stable tautomer of the neutral species is *2H* both in the gas phase and in water (*3H* and *5H* have higher energy), and the two conformers, and are almost isoenergetic in water. Tautomers in which the proton is bonded to N atoms of the pyrazinic ring have also been considered. However, they show prohibitively high energy. The relative stability of singly protonated tautomers of **TT9** has been investigated due to their organic base character. Its six sites available for protonation may give rise to several protonated tautomers. For the isolated gas-phase singly protonated molecule-ion, the most stable tautomer is *1H-3H s-cis*. The *s-trans* conformer is highly destabilized by a close 1...6 contact between the N1-H and the ortho C-H of the pyrazine ring. Otherwise, in water, three different tautomers-conformers are predicted with a population higher than 10% (*1H-3H s-cis*, *2H-3H s-trans* and *2H-3H s-cis* in order of stability).

Table 8 Computed relative energies about neutral and singly protonated tautomers **TT9**. Protonation at meta(*m*) N atoms of the pyrazine ring is also considered.

Tautomer of neutral <b>TT9</b>	Energy (kcal mol <sup>-1</sup> ) gas	Energy (kcal mol <sup>-1</sup> ) water	Tautomer of <b>TT9</b> cation	Energy (kcal mol <sup>-1</sup> ) gas	Energy (kcal mol <sup>-1</sup> ) water
<i>2H s-trans</i>	0.6	0.1	<i>1H-3H s-cis</i>	0.0	0.0
<i>2Hs-cis</i>	0.0	0.0	<i>1H-3H s-trans</i>	6.2	3.2
<i>3Hs-trans</i>	6.5	1.4	<i>2H-3H s-cis</i>	9.3	1.7
<i>3Hs-cis</i>	8.6	1.9	<i>2H-3H s-trans</i>	7.5	1.1
<i>5Hs-trans</i>	12.7	7.8	<i>2H-5H s-cis</i>	16.7	10.6
<i>5H s-cis</i>	22.7	13.3	<i>2H-5H s-trans</i>	5.2	4.4
			<i>3H-m s-cis</i>	16.9	5.0
			<i>3H-m s-trans</i>	13.0	4.1

The X-Ray molecular structure of **TT9** is reported in Figure 30. The neutral compound crystallizes as the monohydrate *2H s-trans* tautomer, and this is in accordance with the computational previously discussed.

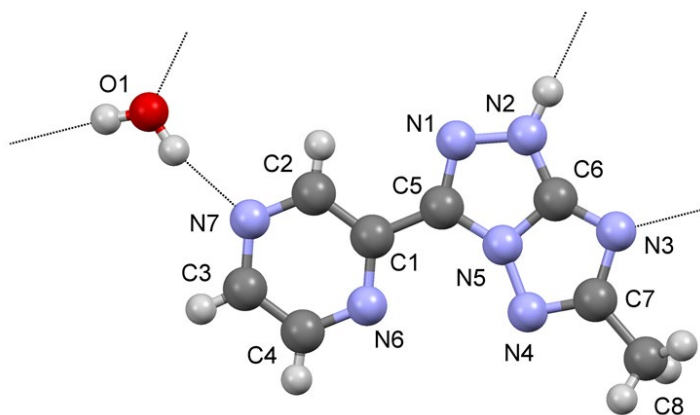


Figure 30. X-ray molecular structure of **1**. Dashed lines indicate strong H bonds.

The relative orientation of pyrazyl and triazolo-triazole rings is *s-trans*, and the two rings are almost coplanar with a dihedral angle  $\tau=3.74(6)^\circ$  between the average planes. The crystal packing is shown in Figure 31. Molecules are arranged in planar layers through strong H bonding involving N-H and O-H water donors and O and N acceptors and weak H-bonding between C-H donors and ring N acceptors. The layers are parallel to the lattice planes  $\bar{1}2\bar{2}$ , and their stacking distance is  $d = 3.247 \text{ \AA}$ . The water molecule heads to a classic H bonding pattern between strong donor acceptors groups (Figure 31).

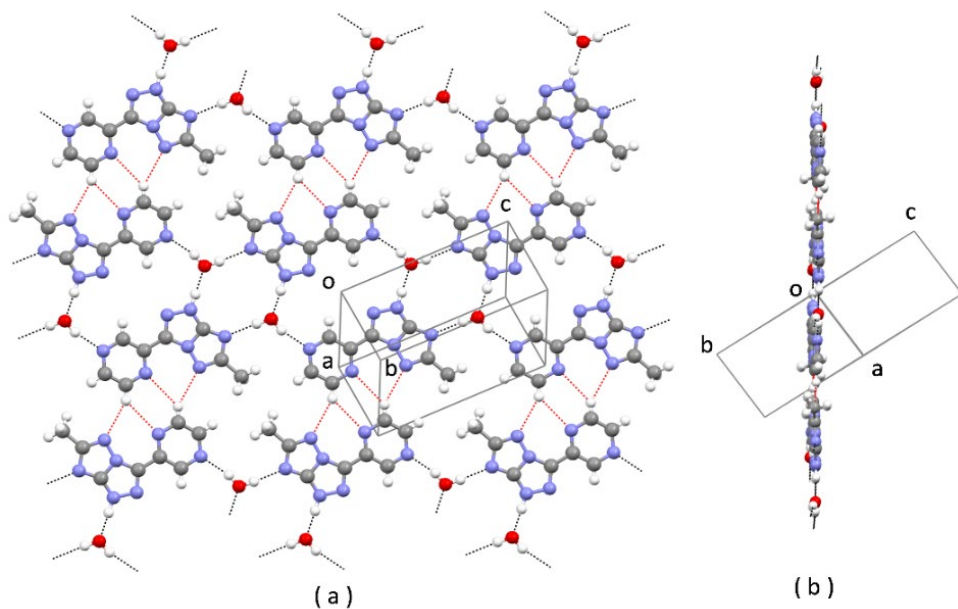


Figure 31. Crystal packing of **1**. (a) front view of a planar layer; (b) edge view of the same layer. Tetramolecular ring-patterns  $R_4^4(12)$  and  $R_4^4(18)$  are formed

Crystal structure has been solved for singly protonated **TT9** as well. As shown in Figure 32, the monoprotonated species (**2**) crystallizes as the *2H-3H s-trans* tautomer, and the conformation is unchanged as compared with the neutral compound (dihedral angle  $\tau$  is  $2.98(4)^\circ$ ).

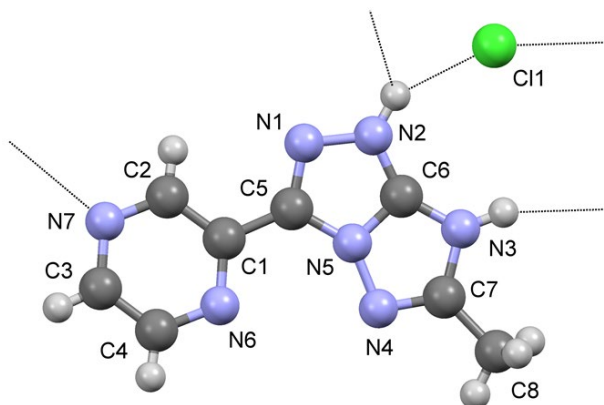


Figure 32. X-ray molecular structure of **2**. Dashed lines indicate strong H bonds.

The tautomer conformer found in the solid-state is predicted 1.1 kcal mol<sup>-1</sup> higher in energy than the most stable one, *1H-3H s-cis*. As reported for similar compounds studied in previous works, when the group in position 7 is an EWG, the most stable tautomer of singly protonated species is *2H-3H*, while with an electron donor substituent, the most stable tautomer is *1H-3H*. In this case, the pyrazyl ring has an electron-withdrawing character which makes the *2H-3H* as the most stable tautomer.<sup>82,83,85</sup> However, the isolated tautomer-conformer *1H-3H s-cis* is stabilized by an intramolecular interaction between the protonated N1-H donor and the ortho N acceptor of the pyrazine ring, and by a weak intramolecular H bond between ortho C-H of pyrazine and N4. The formation of intermolecular H-bonds can promote the stabilization of the less stable tautomer, especially in presence of strong H-bonding competitors (water molecules, chloride ions), as shown in Figure 33.

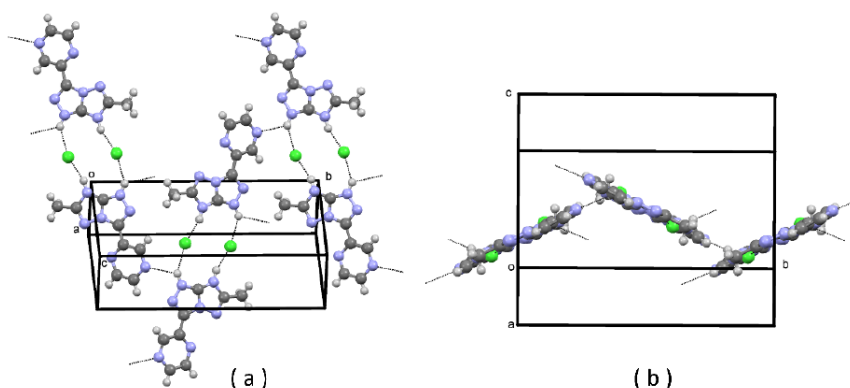


Figure 33. Crystal packing of 2. a) face view b) edge view.

The high versatility of **TT9** as a molecular building block is confirmed by the synthesis of hybrid organic-inorganic salts with tetrahedral and octahedral complex anions (structures **3** and **4** of Chart 4). The doubly protonated cation of **TT9** has been crystallised in the form of tetrachlorozincate salt (**3**) (Figure 34). The dication crystallizes as the *2H-3H-7H s-trans* tautomer/conformer ( $\tau$  is  $11.3(3)^\circ$  and  $11.5(3)^\circ$  in the two independent cations). The placement of the additional H atom on N7 can be understood if we notice that N7 is the acceptor atom farthest away from both N2 and N3. The crystal packing shows layers of organic cations sandwiched between layers of tetrahedral inorganic complex anions, which is a feature typical of hybrid organic-inorganic salt structures. The crystal structure is stabilized by many N-H $\cdots$ Cl hydrogen bonds that, due to the formation of the *2H-3H-7H* tautomer, are distributed over the entire length of the organic molecule-ion.

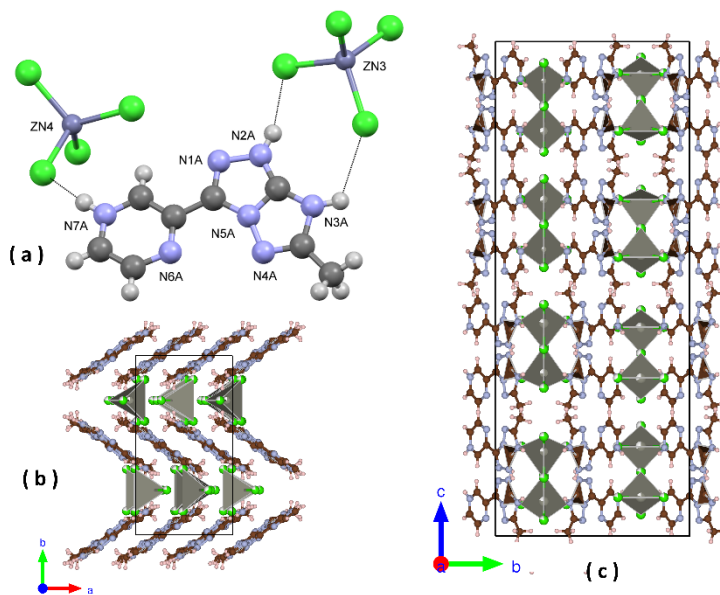


Figure 34. X-ray molecular structure of **3**. Dashed lines indicate strong H bonds. Half of the independent unit is shown for clarity. (b) crystal packing viewed down *c*; (c) crystal packing viewed down *a*.

The doubly protonated cation of **TT9** was also crystallized with complex octahedral anions,  $\text{SnCl}_6^{2-}$  (Figure 35). Also in this case, the *2H-3H-7H s-trans* tautomer is observed ( $\tau = 9.2(2)^\circ$ ).

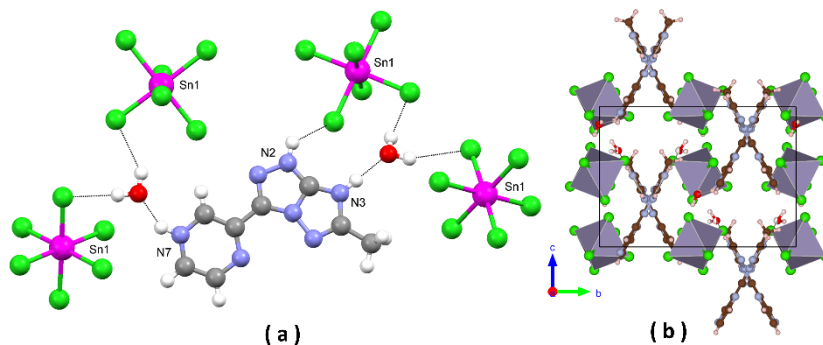


Figure 35 a) X-ray molecular structure of **4**. Strong H bonds are indicated by dashed lines; (b) crystal packing viewed down *a*. Only the most populated component of one disordered water molecule is shown.

The crystal structure of the deprotonated form of **TT9** has been investigated as well. The sodium triazolate crystallizes as trihydrate (Figure 36). The conformation around C1-C5 is again *s-trans* and the Na<sup>+</sup> cation is chelated by N4 and N6 atoms of the ligand, forming a six-membered ring ( $\tau=8.07(8)^\circ$ ). The coordination geometry around Na<sup>+</sup> is distorted trigonal bipyramid (N6-Na1-O1=  $177.89(6)^\circ$ ). A five-membered chelate ring could have formed with N1 and N6 donor atoms and the anion in *s-cis* conformation. However, according to the resonance forms of Chart 6, no negative charge is present on N1, so the (N4, N6, *s-trans*) chelation mode is favoured for the anionic ligand.

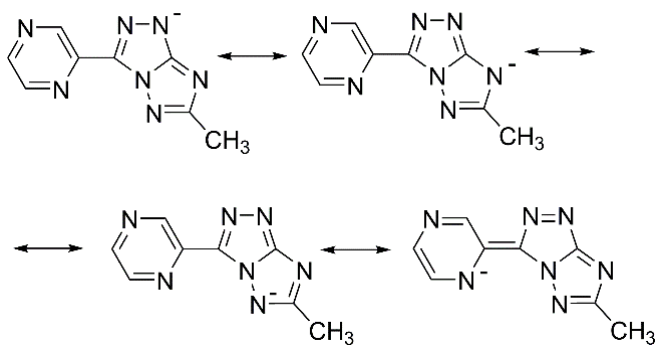


Chart 6 Resonance forms for the deprotonated anion of **TT9**.

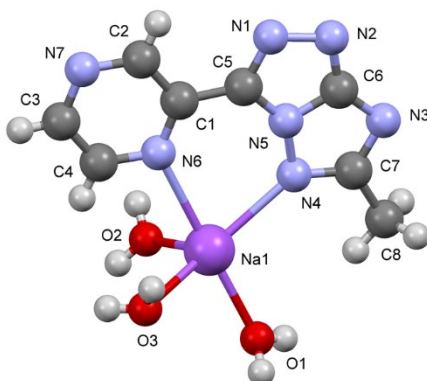


Figure 36 X-ray molecular structure of **5**. H bonds are not indicated for clarity

The sodium triazolate forms infinite ribbon chains along the *b* axis held by H bonding between N7 and water hydrogen atoms. Along the *a* axis, the organic molecules are not stacked and each layer is held by strong H bonding between the oxygen atoms and hydrogen atoms up and down the triazolate molecule, and weak H bonding as well in the plane (Figure 37).

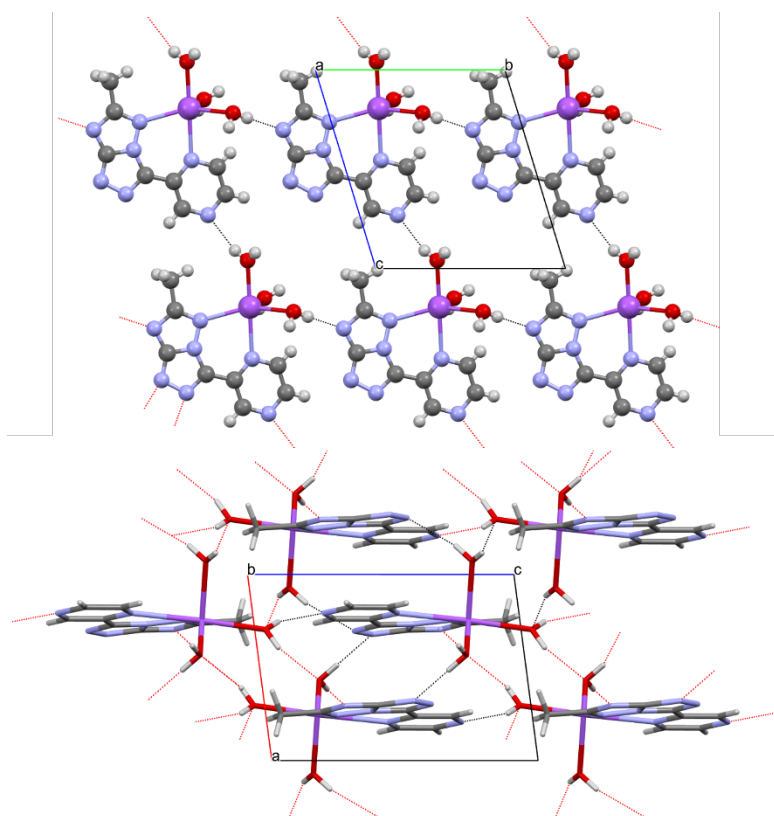


Figure 37 Crystal packing of 5

In the case of the neutral ligand, the chelation mode (N1, N6, *s-cis*) should be considered competitive with (N4, N6, *s-trans*). Thus, four metal complexes with different metal-to-neutral ligand ratio were isolated. Complexes 6 and 7 were obtained using a 1:1 M-to-L ratio, while for 8 and 9 the ratio 1:2. The X-Ray

molecular structure of  $\text{Cu}_2(\text{TT9})_2\text{Cl}_4$  (**6**) shows the (N1,N6, *s-cis*) chelation mode, with the ligand almost planar and the dihedral angle  $\tau$  being  $1.5(2)^\circ$  and  $2.2(2)^\circ$  in the two crystallographically independent units (Figure 38). Each neutral ligand acts as tridentate ligand because the N2 of the fused heterobicycle is also coordinated to another metal centre by promoting centrosymmetric dimers. In this way, the acidic N-H proton switches from N2 to N3, so allowing the elusive *3H* tautomer to be isolated for the first time. The *3H s-cis* tautomer has energy  $1.8 \text{ kcal mol}^{-1}$  higher energy than the *2H s-trans*.

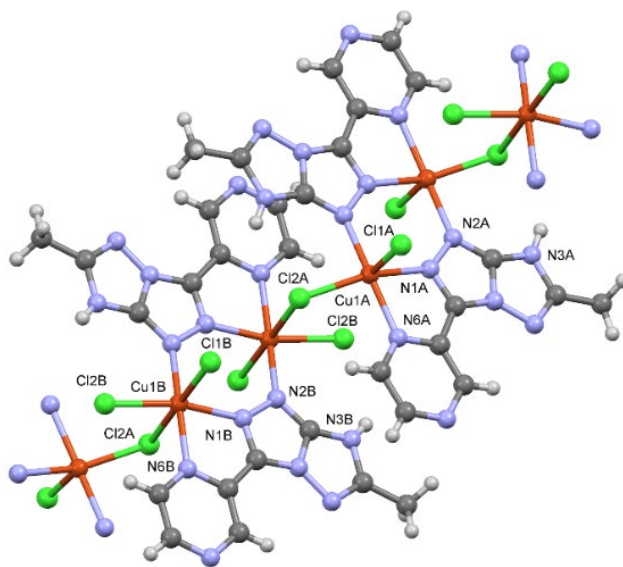


Figure 38. X-ray structure of  $\text{Cu}_2(\text{TT9})_2\text{Cl}_4 \cdot 5\text{H}_2\text{O}$ . Water molecules are omitted for clarity. Labels are shown only for N, Cl and Cu atoms for clarity.

The two crystallographically independent Copper atoms show different coordination geometries: Cu1B is octahedral with strong tetragonal distortion (the four in-plane bond lengths are in the range  $1.981(3) - 2.2497(11) \text{ \AA}$ ), while the two *trans*-elongated bond lengths are  $\text{Cu1B-Cl1B } 2.668(8)$  and  $\text{Cu1B-Cl2A } 2.950(1) \text{ \AA}$ ; Cu1A is square pyramidal because the strong distortion does not

allow Cl2B to bind Cu1A (Cu1A-Cl2B=3.294(1) Å. Both the observed coordination geometries can be related to Jahn-Teller distortions.

The X-Ray structure of  $Zn_2(TT9)_2(H_2O)_6(Zn_2Br_6)_2$  dihydrate (**7**) also shows the presence of the *3H* elusive tautomer (Figure 39). The chelation mode is again *s-cis* and the formation of centrosymmetric dimers is the same as for complex **6**, although in this complex **TT9** acts as a tetradentate ligand because also N7 of pyrazyl ring is coordinated, but to a zinc bromide anionic unit. In view of these results, metal coordination can be considered a reliable way to allow the isolation of elusive tautomers with a narrow energy gap ( $\Delta E < 2\text{kcal mol}^{-1}$  Table 8). This is further confirmed by the structural analysis of complexes **8** and **9**, with an M/L ratio of 1:2.

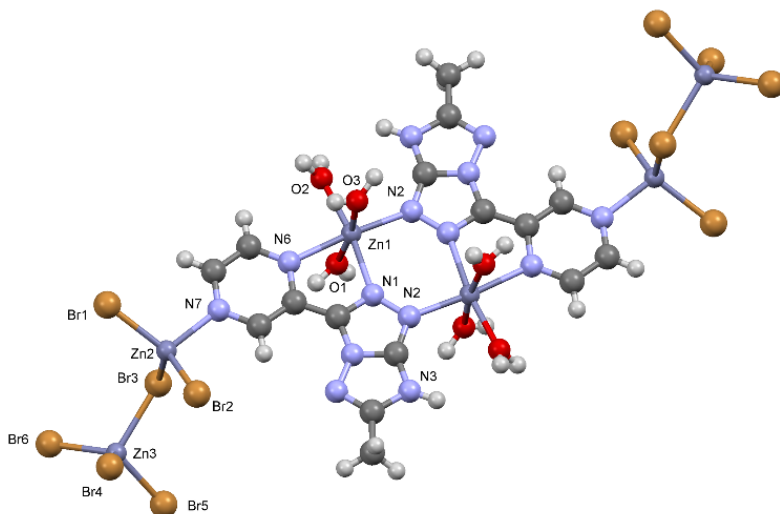


Figure 39. X-ray structure of  $Zn_2(TT9)_2(H_2O)_6(Zn_2Br_6)_2$  dihydrate. Non-coordinated water molecules are omitted for clarity. Labels are shown only for N, Cl and Cu atoms for clarity

In the crystal structure of  $Cu(TT9)_2Br_2 \cdot 3H_2O$  (**8**) (Figure 40), two *3H s-cis* **TT9** molecules are coordinated to Copper (II). Both the ligands are bidentate chelate in a square-planar arrangement, with *s-cis* conformation. The four metal-to-ligand

distances in the equatorial plane show distorted square planar geometry (Table 9). One water molecule and one bromide ion complete the octahedral coordination geometry of Cu(II) with tetragonal distortion. The selection of the elusive tautomer is presumably due to the strong preference of Copper (II) for square planar coordination with N-donor atoms and the strong H bonding interactions between N-H donors and N-atom acceptors on the rim of the coordinated ligands (Table 9).

*Table 9 Coordination and hydrogen bonds list for 8.*

<b><i>Bond list</i></b>	<b>Bond Length (Å)</b>	<b>D-H...A list</b>	<b>H...A (Å)</b>
<i>Cu-N6A</i>	2.117(5)	N3A-H3NA...O2	1.82(3)
<i>Cu-N6B</i>	2.125(5)	N3B-H3NB...Br2	2.34(3)
<i>Cu-N1A</i>	1.953(5)	N3B-H3NB...O1W	1.85(3)
<i>Cu-N1B</i>	1.951(5)		
<i>Cu-O</i>	2.410(5)		
<i>Cu-Br</i>	2.7466(12)		

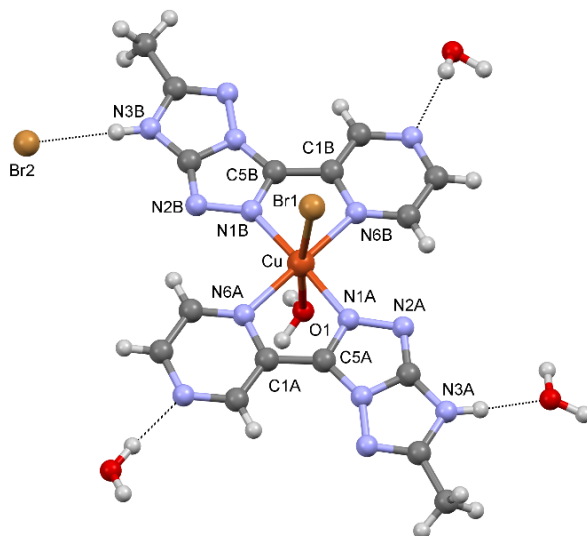
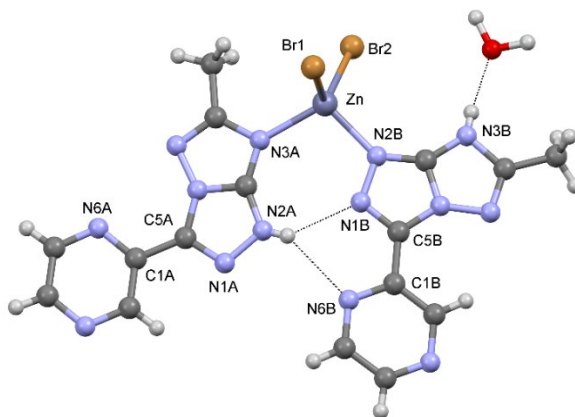


Figure 40. X-ray molecular structure of **8**. Dashed lines indicate H-bonds. Labels are shown only for C, N, Br and Cu atoms for clarity.

The X-ray molecular structure of  $\text{Zn}(\text{TT9})_2\text{Br}_2 \cdot \text{H}_2\text{O}$  (**9**) shows different features (Figure 41). The two **TT9** neutral ligands are both monodentate but they are present in different tautomer/conformers: ligand A is in the most stable tautomer/conformer, *2H s-trans*, while ligand B is in the elusive tautomer *3H s-cis*. The coordination geometry around Zinc(II) is tetrahedral and is completed by two bromide ions (Table 10).

Table 10 Coordination and hydrogen bonds list for **9**.

<b>Bond list</b>	<b>Bond Length (Å)</b>	<b>D-H...A list</b>	<b>H...A (Å)</b>
<i>Zn-Br1</i>	2.4017(11)	N2A-H2NA...N1B	2.09(4)
<i>Zn-Br2</i>	2.3581(9)	N2A-H2NA...N6B	2.39(4)
<i>Zn-N3A</i>	2.059(4)	N3B-H3NB...O1W	1.85(3)
<i>Zn-N2B</i>	2.018(4)		



*Figure 41. Molecular structure of complex 9. H bonds are indicated by dashed lines*

In the crystal structure, the two different tautomeric forms are bonded to each other through a strong bifurcated hydrogen bond. This is the first evidence in literature of two different tautomeric forms of a neutral ligand coordinated to the same metal centre. A deep analysis of this crystal structure can highlight some basic rules for the rational design of the mixed-tautomeric ligand complexes:

1. The two tautomeric forms should have similar energy so that both are present in similar amounts in solution, and they should have similar ligand donor capability.
2. The two tautomeric forms need to have complementary functional groups to give stable mixed adducts by SBIs
3. The mixed adducts should be featured a pocket, suitable for with dimensions and presence of donor atoms, to bind metal ions.

The combination of all these points makes the idea about the rarity of the phenomenon. **TT9** is, therefore, an extremely versatile binder and an excellent candidate for the formation of heterotautomeric complexes. In fact, by only considering the four tautomer/conformers at lower energy, out of the 10 possible

combinations between them, in four cases it is possible to form H-bonded dimers. In all of them, a strong bifurcated H bond is present between the N-H donor of a tautomer and the two *s-cis* N acceptor atoms of the other (Chart 7).<sup>iii</sup>

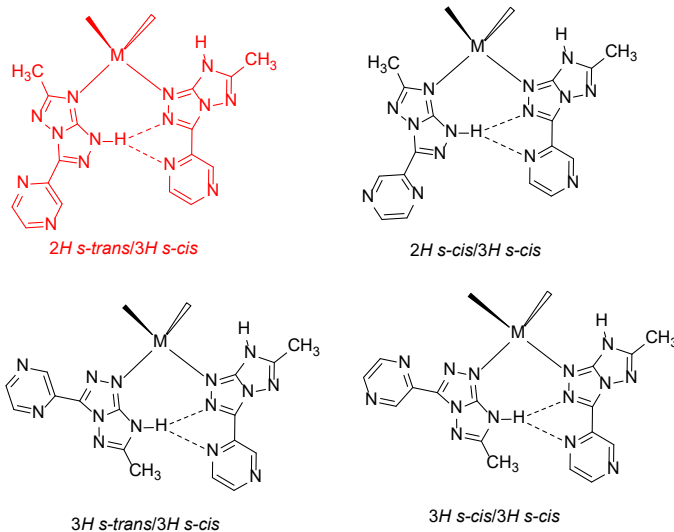


Chart 7. H-bonded dimers of **TT9**. Highlighted in red is the dimer found in complex **9**

<sup>iii</sup> Parts of this chapter have been published in *Acta Cryst.*, 2021, C77, 395-401.

### 3.3 High-Energy-Density Materials

#### 3.3.1 General aspects

Traditional energetic materials (TNT, RDX, HMX) are widely used for military and civil applications as high-energy components of explosives, gunpowders, propellants or pyrotechnics. In the recent years, several new synthetic materials, such as TKX-50 and CL-20 have been reported, attracting considerable attention.<sup>86</sup> Hence, one the development topic of HEDMs involves the study of novel materials with high nitrogen contents, from which a considerable amount of energy can be obtained due to the heat of formation instead of energy released from intermolecular oxidation of carbon backbone in a nitro group or nitrate.<sup>87-89</sup> In figure 42 are reported some traditional explosives replaced with high-nitrogen compounds.<sup>90</sup> Reducing C and H contents in compounds can increase the density. These materials have a higher fraction of nitrogen by mass than classical explosives, so that they derive their energy output from this factor, rather than exploiting the redox reactions of fuel elements (carbon, hydrogen) as in the case of classical ones. Furthermore, high thermal stability, high heat of formation and high density combined with high detonation pressure and detonation velocity are fundamental properties of novel HEDMs. Energetic materials usually release energy when they decompose because of oxidation processes. Nitrogen-rich heterocyclic compounds are no exception: they contain nitrogen atoms which usually take part in single or double bonds; when the molecule decomposes, N<sub>2</sub> is formed. The great amount of energy released by the process is a consequence of the fact that the bond energy of the N-N triple bond (954 kJ/mol) is much higher than that of a double or single bond (418 kJ/mol and 160 kJ/mol respectively).

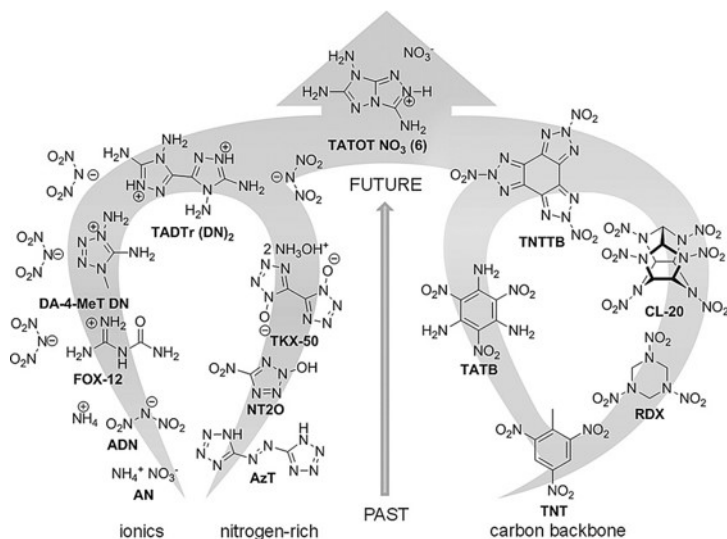


Figure 42. Selected chemical structures of secondary explosives which give an overview of different concepts and research strategies used during the development of new secondary explosives. Ionic compounds (*AN*, *ADN*, *FOX-12*, *DA-4-MeTDN*); N-rich heterocycles (*AzT*) with N-oxides (*NT20*, *TKX-50*); introduction of amino- (*TADTr (DN)<sub>2</sub>*, *TATB*), nitro- (*TNT*, *TATB*), and nitramino functional groups (*RDX*, *CL-20*); HB network (*FOX-12*, *TATB*) caged (*CL-20*) and fused (*TNITB*, *TATOT*) molecules. Figure taken from ref. 90.

The advantage of N-rich heterocyclic compounds is the presence of acidic or basic moieties (usually basic N atoms or acidic N-H groups) which can be exploited to form salts where the main N-rich heterocycle molecule is in the form of a cation or anion. These salts have intrinsically low volatility, an increased energy content coming from the high energy of the ionic lattice, and their properties can be tuned in principle by suitable choice of the counterion and by crystal engineering approaches.

Here is reported the synthesis and characterization of HEDMs based on the N-rich heterocyclic compound 1*H*,4'*H*-[3,3'-bi(1,2,4-triazole)]-4',5,5'-triamine (henceforth **bTT**) shown in Chart 8. It belongs to the class of 1,2,4-triazoles,

which have been widely explored in recent years,<sup>90–93</sup> and has a high N content (69.6 % wt).<sup>iv</sup>

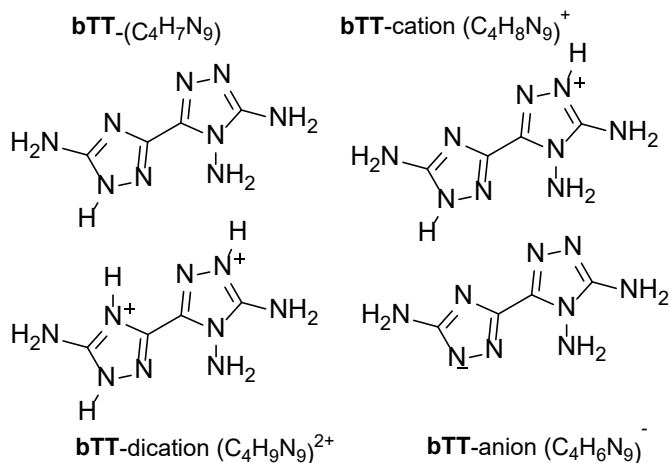


Chart 8. Neutral, singly protonated, doubly protonated, and deprotonated forms of **bTT**. Only one tautomeric form is shown for the neutral and cationic species. For the anion, only one resonance form is shown.

A rich acid-base behaviour of **bTT** can be expected due to the three amino electron-donor groups by promoting the line-up of cationic and anionic forms (Chart 8). So, at variance with most of the energetic N-rich compounds studied so far, with **bTT** it is possible, in theory, to prepare salts in which the N-rich heterocycle is present as anionic/protonated/double protonated forms. Indeed, those salts have been prepared and characterized in solution and solid-state, including measurements of sensitivities in the solid-state for the energetic compounds. Some energetic salts of **bTT** have been recently studied by Shreeve<sup>94</sup> and Cheng/Yang,<sup>95</sup> with a possible application as gas generating agents, propellants, or explosives. As already seen for **TT9**, **bTT** system is potentially tautomeric. The tautomeric forms of the protonated and neutral species are

<sup>iv</sup> Parts of this chapter have been published in *Inorg. Chem.*, 60, 21, 16213-16222.

reported in chart 9. Also for this system there are two potential conformations (*s-cis* and *s-trans*) for each tautomer.

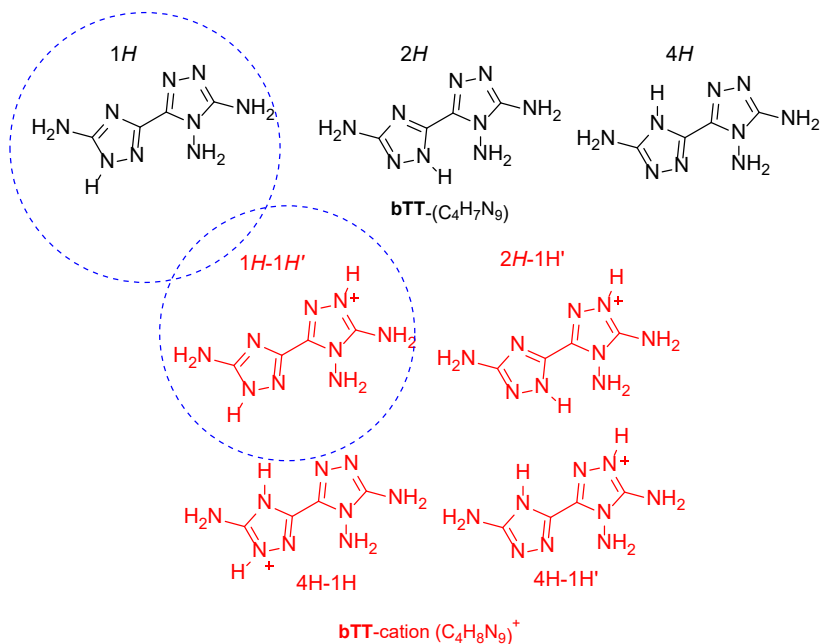


Chart 9 Some possible tautomers of *s-trans* **bTT** (in black). In red Singly protonated **bTT**. Blue dashed circles highlight the most stable predicted tautomers/conformers.

The computational data for **bTT** are reported in table 11. The most stable predicted for the neutral form in polar medium, is *1H/s-trans*. The *2H* tautomer, however, follows quite close in energy both in the *s-trans* and, mostly, in *s-cis* conformation. The *2H/s-cis* is predicted as the most stable tautomer/conformer, probably due to intramolecular N-H...N interaction, and in polar medium the energy of *2H/s-cis* is only 0.5 kcal/mol higher than *1H/s-trans*, a value which is within the accuracy of the method used in the calculations. Contrary, the *4H* conformer has substantially higher energy. As concerns singly protonated species, data of Table 11 show that tautomer *1H-1'H* is the most stable both in the gas phase and in polar medium. The other tautomers all have significantly higher energy. For the doubly protonated cation, computational analysis was not performed because the doubly

protonated tautomer in Chart 8 is the only possibility for both positive charges on nitrogen atoms adjacent to C-NH<sub>2</sub> groups.

Table 11. Computed relative energies (kcal/mol) of tautomers/conformers of neutral and singly protonated **bTT**. a: Interconverts in conformer *s-cis* upon geometry optimization.

Tautomer	Gas		Water	
	<i>s-cis</i>	<i>s-trans</i>	<i>s-cis</i>	<i>s-trans</i>
1H	6.7	6.3	0.4	0.0
2H	0.0	9.2	0.5	1.3
4H	18.2	6.4	5.2	3.5
1H-1'H	0.4	0.0	0.5	0.0
2H-1'H	3.6	Not stable <sup>a</sup>	3.0	7.1
4H-1'H	23.2	7.2	7.6	5.0
1H-4H	18.2	13.8	6.1	7.8

### 3.3.2 Analysis in solution

The protolytic equilibria of **bTT** were studied by UV-Vis absorption spectroscopy at 25° C in constant ionic medium NaCl 0.5M. The spectra were recorded in the 0.7 ≤ pH ≤ 9.8 range with constant total concentration 5.01 · 10<sup>-5</sup> M of **bTT** (Figure 43). There is a non-monotonic dependence of λ<sub>max</sub> from the pH. Starting from the acidic value of pH (pH=0.7, λ<sub>max</sub> =257 nm) an hypsochromic shift up to pH=2.9 (λ<sub>max</sub> =248 nm) is observed. Then, by increasing pH up to 6.6, the shift of λ<sub>max</sub> is always bathochromic (λ<sub>max</sub> =257 nm), and further on to pH= 9.8 (λ<sub>max</sub> =264 nm). The changes in the absorption spectra can be accounted for by the three equilibria of Table 12. As shown in the table, **bTT** can accept up to two protons (H<sub>3</sub>L<sup>2+</sup> and H<sub>2</sub>L<sup>+</sup>) and release one proton (L<sup>-</sup>)

Table 12. Acid constants in the form of pK<sub>a</sub> (at 25 °C in 0.5 M NaCl) for **bTT** (HL).

Equilibrium	pK <sub>a</sub>

$\text{H}_3\text{L}^{2+} + \text{H}_2\text{O} = \text{H}_3\text{O}^+ + \text{H}_2\text{L}^+$	$\text{pK}_{\text{a}1}=1.31(2)$
$\text{H}_2\text{L}^+ + \text{H}_2\text{O} = \text{H}_3\text{O}^+ + \text{HL}$	$\text{pK}_{\text{a}2}=4.56(2)$
$\text{HL} + \text{H}_2\text{O} = \text{H}_3\text{O}^+ + \text{L}^-$	$\text{pK}_{\text{a}3}=9.25(5)$

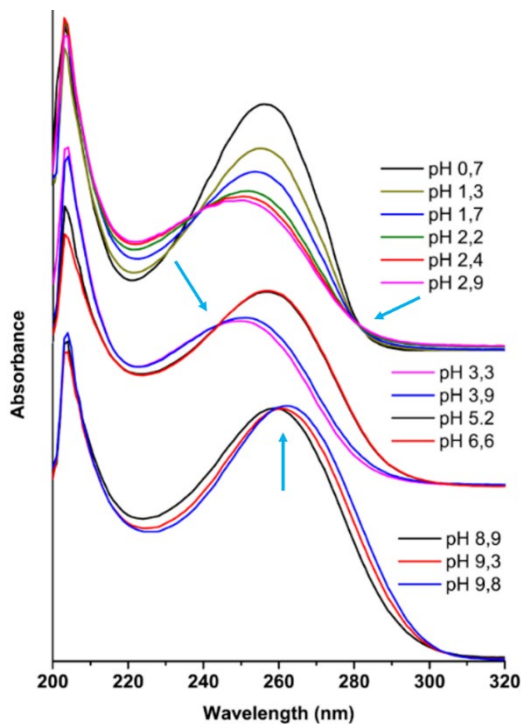


Figure 43. UV-VIS absorption spectra of **bTT** at constant total concentration  $c = 5.01 \times 10^{-5} \text{ M}$ , in  $\text{NaCl } 0.5 \text{ M}$  recorded at  $0.7 \leq \text{pH} \leq 9.8$ . The spectra have been grouped in three sets of curves arbitrarily shifted along the vertical axis for easier lecture. Cyan arrows highlight isobestic points.

From the calculated constants, it is possible to derive the distribution diagram for **bTT** (Figure 44). Each of the four forms is predominant in the defined pH range with a molar fraction  $\geq 90 \%$ . For this reason, it is possible to crystallize salts of each ionic species from solutions.

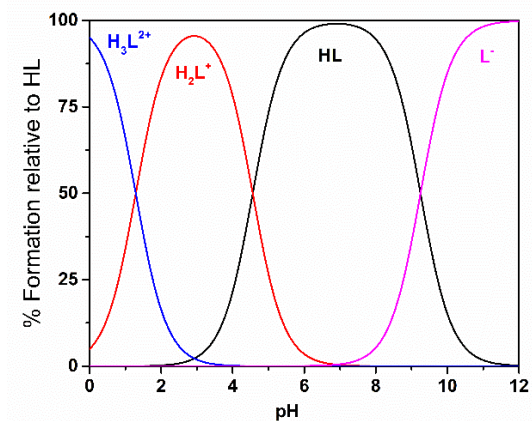


Figure 44 Distribution diagram of **bTT** (HL), calculated using the constants of Table 12.

Based on the distribution diagram, the isosbestic points at  $\lambda$  [282 nm, 244 nm and 259 nm] in Figure 45, are related, respectively, with the three equilibria:

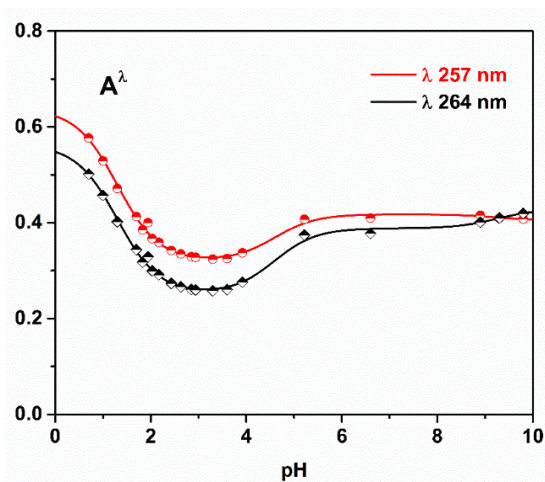
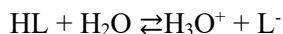
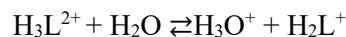


Figure 45. UV-Vis titration curves of **bTT**, at two different wavelengths. The continuous curves have been constructed by fitting the experimental points (absorbance vs pH data taken from Figure 42) with the Bouger-Lambert-Beer equation.

### 3.3.3 Crystallographic and computational analysis

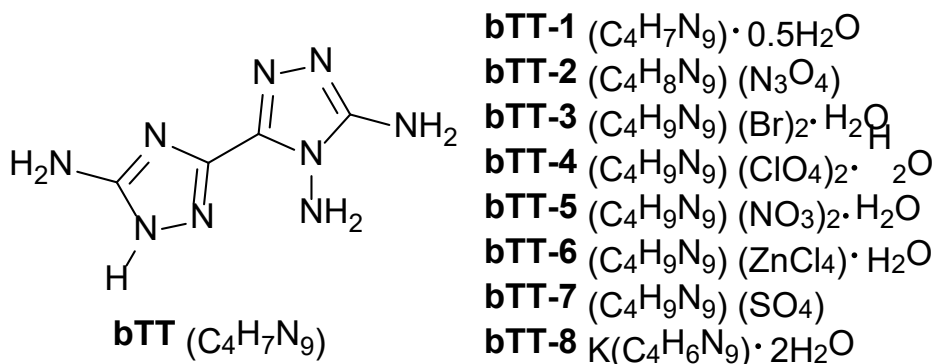


Chart 10. **bTT** isolated crystal structure.

The speciation study in solution has simplified the crystallization of all four **bTT** protolytic species (Chart 10). Except for **bTT-8**, in which **bTT** is anionic, the characterized crystal structures show several strong hydrogen bonding on the rim of the molecule (C-NH<sub>2</sub> or N<sup>+</sup>-H groups). These in-plane H-bonding acceptor and donor groups drive to the formation of stacked structures in which H-bonded molecules are piled up.

Neutral **bTT** crystallizes in triclinic P-1 space group as hemihydrate (**bTT-1**). The most stable tautomer *1H* predicted by computational analysis (Table 11) is clearly evidenced in the crystal structure (Figure 46). There are four crystallographically independent molecules, *Z*=8, in *s-trans* conformation with a dihedral angle  $\tau$  between the average planes of the two rings ranging between  $4.2(1)^\circ < \tau < 11.8(1)^\circ$ . The bond geometry around amino N atoms is relevant for the packing because they are H-bonding donors. The geometry is pyramidal for (N)-NH<sub>2</sub> atoms (the sum of the valence angles around amino N atom ranges between  $320(3)^\circ$  and  $327(2)^\circ$  for the four independent molecules). This result basically holds unchanged in all the structures determined. The geometry around

(C)-NH<sub>2</sub> nitrogen atoms is still pyramidal, but flatter, because the conjugation with the aromatic ring (the sum of the valence angles around amino N atom ranging, in this case, between 341(2)° and 358(3)° for the four independent molecules).

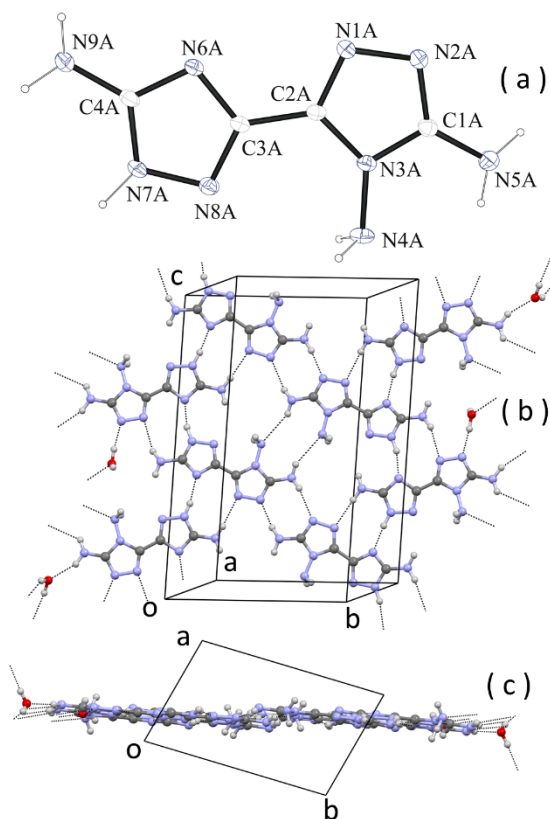


Figure 46. (a) Ortep diagram of one of the four crystallographically independent molecules of **bTT-I**; (b) H-bonding pattern intra layer; (c) the same layer viewed down *c*. Some H-bonds are indicated by dashed lines.

Molecules in the crystal form infinite planar layers parallel to the lattice planes  $2\bar{1}0$ , through H-bonds involving the many N-H donor and N acceptors present in the molecules of **bTT** and the water molecules (Figure 46(b),(c)). The stacking distance,  $d_{2\bar{1}0}=3.12 \text{ \AA}$ , of the layers is achieved through H-bonds between

adjacent layers. The high density of the crystal,  $\rho=1.629 \text{ g/cm}^3$  at  $-100 \text{ }^\circ\text{C}$ , is due to the extended network of strong H-bonds.

The dinitramide salt of **bTT** monocation, **bTT-2**, was obtained by metathesis reaction of the perchlorate salt, **bTT-4**, with potassium dinitramide. For **bTT-2** the crystallographic analysis shows unambiguously the presence of the  $1H\text{-}1H'$  *s-trans* conformer/tautomer in agreement with computational analysis (Figure 47).

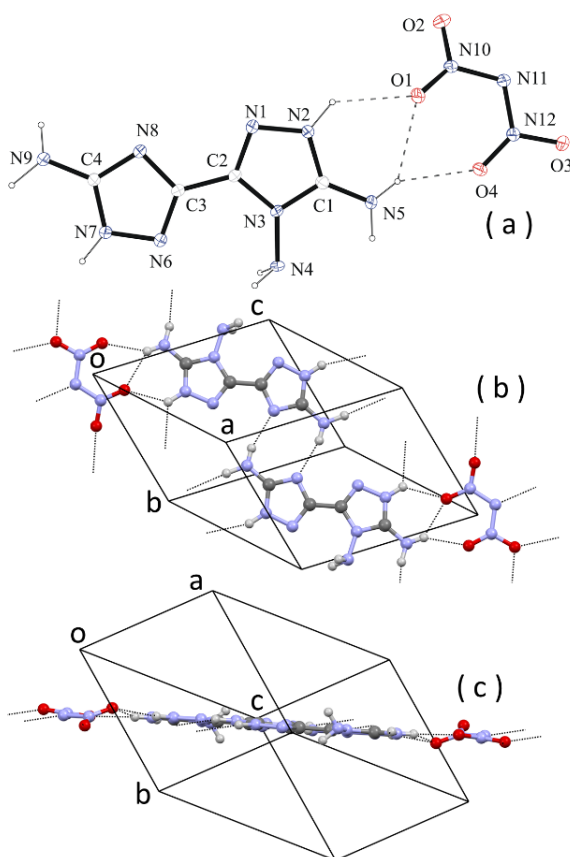


Figure 47. (a) Ortep diagram of the independent crystallographic unit of **bTT-2**; (b) face view of a layer of H-bonded molecules; (c) edge-view of the same layer. Some H-bonds are indicated by dashed lines.

The conformation of the cation is basically flat, the dihedral angle between the average planes of the two rings being  $5.2(2)^\circ$ . The geometry around amino (N)-

NH<sub>2</sub> atom is pyramidal (sum of valence angles is 319(4)°). As compared with neutral **bTT**, full planarization of the geometry around (C)-NH<sub>2</sub> Nitrogen atoms is observed, the sum of valence angles being 360(5)° and 359(5)°. The molecules in the crystal form planar ionic/H-bonded layers through N-H donor and N acceptors from the cation molecule and O and N acceptors from the dinitramide anion. The layers are parallel, as **bTT-1**, to the lattice planes  $1\bar{2}1$  with a stacking distance of  $d_{1\bar{2}1}=3.11 \text{ \AA}$ . Also in this case, the presence of several strong H-bonds and the ionic interactions between cations and anions accounts for the significantly higher density of the crystal,  $\rho=1.837 \text{ g/cm}^3$  at -100 °C.

The double protonated cation of **bTT** is present in 5 different crystalline structures, **bTT-3** – **bTT-7**. The crystallizations were performed by dissolving neutral **bTT** in water solution of hydrobromic, perchloric, nitric and sulphuric acid, respectively (Appendix A). In all the 5 crystal structures, the dication is present as the *1H-1'H-4H s-trans* tautomer/conformer in agreement with the calculations. The single or double protonation of **bTT** is always at the ring N atoms and this can be rationalized by the fact that amino groups have electron donor character and hence they can stabilize the positive charge of the cation. This is the reason why the geometry around the amino (C)-NH<sub>2</sub> nitrogen atoms is planar trigonal in all the 5 structures in which the double protonated form of **bTT** is present.

**bTT-3** crystallizes in triclinic P-1 space group (Figure 48). The crystal packing shows layers of cations **bTT**<sup>2+</sup> and bromide ion held together by strong H-bonds between bromide ion acceptor and N-NH<sub>2</sub> donor groups, with the formation of  $R_4^2(8)$  ring patterns. The layers are parallel to the lattice plane  $1\bar{2}2$ , with a short stacking distance of  $d_{1\bar{2}2}=3.13 \text{ \AA}$ .

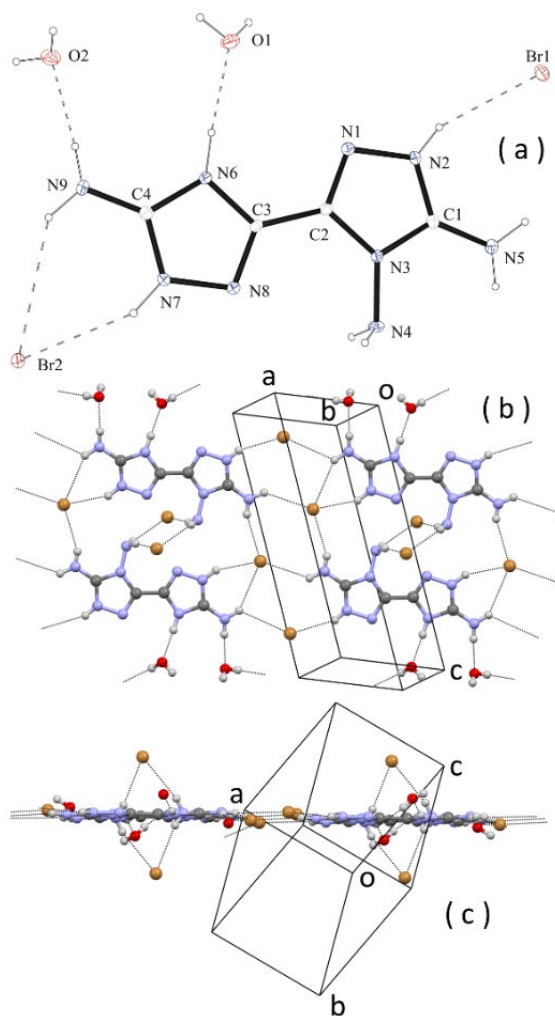


Figure 48. Crystal structure of **bTT-3**. (a) Ortep diagram of the crystallographic independent unit; (b) face view of a layer of ionic/H-bonded molecules; (c) edge-view of the same layer. Some H-bonds are indicated by dashed lines. Some hanging H-bonds have been omitted for clarity.

In both the crystal structures of **bTT-4**, Figure 49, and **bTT-5**, Figure 50, the dications are surrounded by oxidizing tetrahedral perchlorate and trigonal planar nitrate anions, respectively. For **bTT-4**, the layers of ionic/H-bonded molecules are parallel to the lattice planes  $11\bar{2}$ , with a stacking distance of  $d_{11\bar{2}} = 3.22 \text{ \AA}$ . In

**bTT-5**, the dication shows the maximum deviation from the planarity, within the set of investigated compounds, with a dihedral angle between the two pentatomic rings of  $\tau=15.0(2)^\circ$ . The layers of ionic/H-bonded molecules are parallel to the lattice planes 211, with a slightly longer stacking distance  $d_{211}=3.32 \text{ \AA}$ .

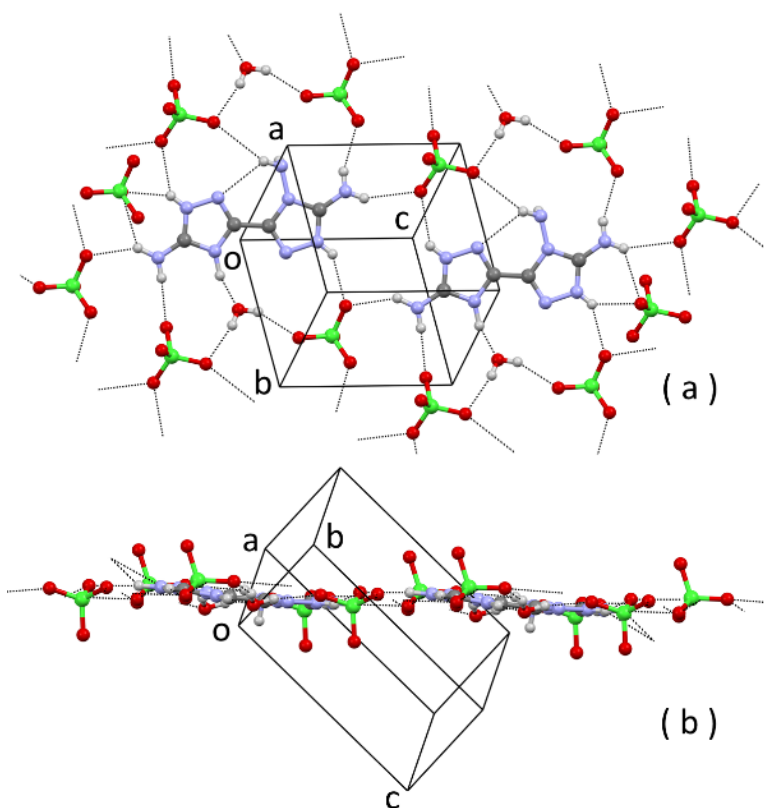


Figure 49. Partial packing of **bTT-4**. (a) face view of a layer of ionic/H-bonded molecules; (b) edge view of the same layer. H-bonds are indicated by dashed lines. Some hanging H-bonds have been omitted for clarity.

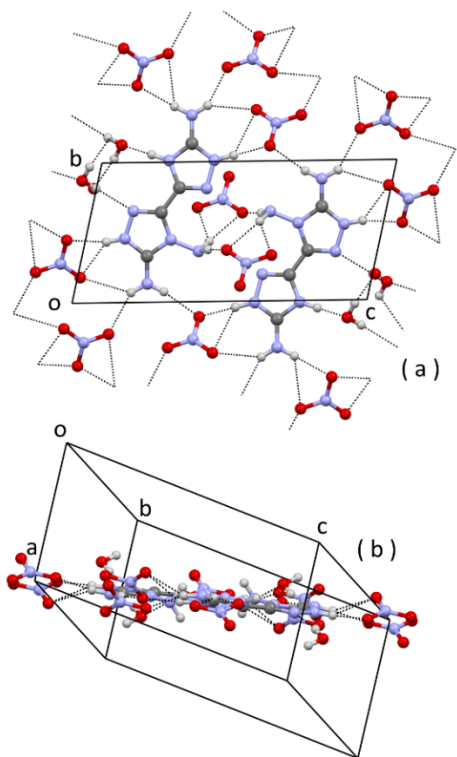


Figure 50. Partial packing of **bTT-5**. (a) face view of a layer of ionic/H-bonded molecules; (b) edge view of the same layer. H-bonds are indicated by dashed lines. Some hanging H-bonds have been omitted for clarity.

The tetrachlorozincate salt of **bTT** dication is shown in Figure 51. The crystal structure of **bTT-6** is characterized by layers of **bTT**<sup>2+</sup> and  $ZnCl_4^{2-}$  held together by a pattern of H-bonds between N-H/O-H donor and chloride/oxygen acceptor groups. There are no N-H $\cdots$ N interactions. The stacking distance between the layers is  $d_{102}=3.16$  Å. Crystal packing of **bTT-7** is shown in Figure 52. Molecules are arranged in a way that maximizes the number of N-H $\cdots$ O hydrogen bonds. As in **bTT-6**, also in this structure, N-H $\cdots$ N interactions are not present. Each Sulphate anion interacts with four close dication molecules by N-H $\cdots$ O bonds in which O is bifurcated acceptor. In this way, perovskite-like motifs in which sulphate ions space out infinite layers of **bTT**<sup>2+</sup> cations are obtained.

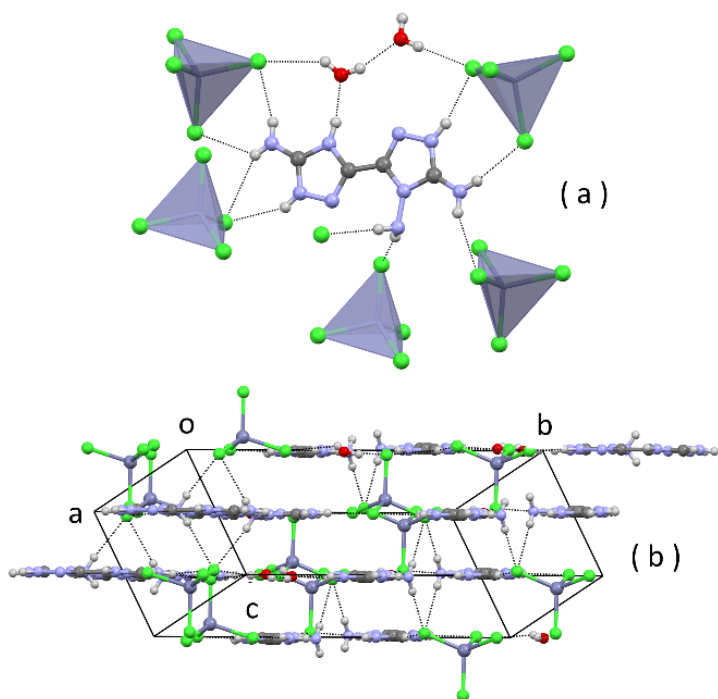


Figure 51. Crystal structure of **bTT-6**. (a) View of the cation, of water molecules and of some H-bonded tetrachlorozincate anions; (b) edge-view of layers of ionic/H-bonded ions. Hanging contacts have been omitted for clarity.

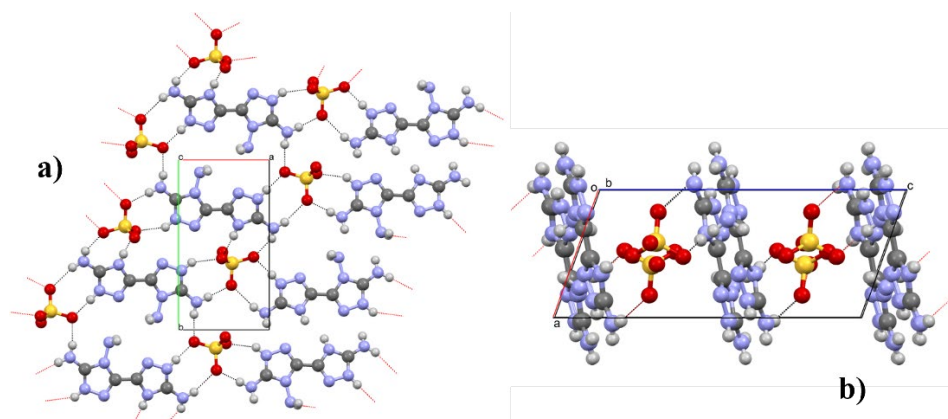


Figure 52 Crystal structure of **bTT-7**. (a) View of the cation and of H-bonding interaction with sulphate anions; (b) edge-view of layers of **bTT**<sup>2+</sup> and Sulphate anions. H-bond are indicated with dashed lines.

In the molecular structure of the potassium salt of **bTT** anion, the geometry around (C)-NH<sub>2</sub> nitrogen is again pyramidal (sum of valence angles is 337(2)° and 347(2)°), and this is expected because the electron excess of the anion reduces the conjugation of (C)-NH<sub>2</sub> amino groups towards the rings. The tendency to the formation of layers is no longer observed because the packing is mainly driven by the coordination geometry of the anionic ligand to the metal ion. Each **bTT** anion acts as tetradentate ligand by four ring N atoms. One N atom is  $\mu_2$  between two K<sup>+</sup> ions, and a water molecule is also  $\mu_2$  bridging between the same metal cations. In this manner, infinite chains running along *a* are established by simple translation (Figure 53a). The glide operation of the space group *P2<sub>1</sub>/c*, allows the formation of chains also along *c* (Figure 53b). In this way, an overall 2D coordination network polymer is formed.

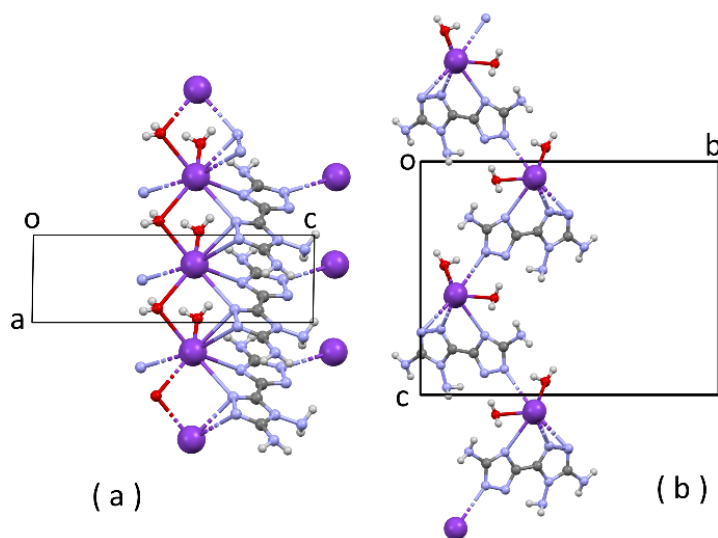


Figure 53. Partial packing of **bTT-8**; (a) projection down *b*; (b) projection down *a*.

Attempts to crystallise **bTT** in basic ammonia-water solution did not return the potentially interesting salt of **bTT** anion with ammonium cation that would feature an increased N content. In fact, crystallization of neutral **bTT** from aqueous ammonia yielded crystals of hydrated neutral **bTT-1**. This result can be

rationalized if we observe that the product of the acid constant of **bTT** ( $K_{a3}$  in Table 12) and of  $K_b$  of ammonia ( $1.774 \cdot 10^{-5}$  at  $25\text{ }^\circ\text{C}$ )<sup>96</sup> is almost equal to  $K_w$ , and so the equilibrium constant of the reaction between ammonia and **bTT** is almost unitary.

### 3.3.4 Thermal and sensitivity analysis

TGA analysis of **bTT** and its energetic salts with oxidizing anions are reported in Figure 54.

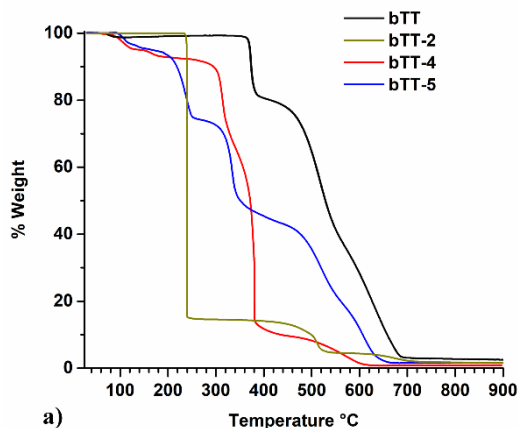


Figure 54. TGA of **bTT** and of some of its salts, in air. Heating rate 10 K/min.

Thermogravimetric curve of **bTT** shows remarkable thermal stability in air up to 347 °C, classifying **bTT** as the most stable N-rich triazole, among those already reported in the literature.<sup>92</sup> The thermal stability of the salts of the dication (perchlorate and nitrate) is lower. The dinitramide salt, in which triamine is present as monocation, has a neat TGA curve: it is fully stable up to 230 °C, when it suddenly decomposes, losing 85 % by weight, with an almost vertical TGA curve. Hence, **bTT-2** show remarkable thermal stability even greater than several N-rich dinitramide salts reported so far in literature as energetic materials,<sup>92</sup> (FOX-12 (N-guanylurea dinitramide),  $T_d=215$  °C).<sup>97</sup>

The friction (FS), impact (IS), and electrostatic discharge (ESD) sensitivities of **bTT** and some of its energetic salts were measured experimentally (grain size 100-500  $\mu\text{m}$ ) and are reported in table 13. These measurements were performed in collaboration with Professor Thomas Klapoetke of the Ludwig Maximilian University of Munich.

Table 13 a) Crystallographic density at -100 °C; b) Calculated density at 298 K, according to ref.<sup>98</sup>; c) Decomposition temperature (onset) for the anhydrous sample in the TGA curves; d) Impact sensitivity (BAM drop hammer); e) Friction sensitivity (BAM friction tester); f) Electrostatic discharge sensitivity; g) Calculated detonation velocity; h) Calculated detonation pressure; i) Calculated heat of detonation; l) Data taken from ref. 89; m) Data taken from ref. 34.

Compound	$\rho$ (g/cm <sup>3</sup> ) <sup>a</sup>	$\rho$ (g/cm <sup>3</sup> ) <sup>b</sup>	T <sub>d</sub> (°C) <sup>c</sup>	IS (J) <sup>d</sup>	FS (N) <sup>e</sup>	ESD (J) <sup>f</sup>	V <sub>oD</sub> (m/s) <sup>g</sup>	P <sub>C-J</sub> (kbar) <sup>h</sup>	Q <sub>ex</sub> (kJ/kg) <sup>i</sup>
<b>bTT</b>	1.629	1.599	347	> 40	>360	1	7681	194	-2378
<b>bTT-2</b>	1.837	1.803	230	4	>360	0.1	8948	311	-4496
<b>bTT-4</b>	1.908	1.873	270	4	192	0.1	7033	191	-1711
<b>bTT-5</b>	1.773	1.740	210	>25	> 360	0.6	8092	246	-3289
<b>RDX<sup>l</sup></b>	1.806		204	7.5	120	0.20	8861	345	-5845
<b>HAT-DN<sup>m</sup></b>	1.856		117	2	20	0.75	9429	384	-6186
<b>5-ATN<sup>m</sup></b>		1.807	190	10	>324	-	8898	357	-4603

The detonation parameters (V<sub>oD</sub> = velocity of detonation, P<sub>C-J</sub> = detonation pressure, Q<sub>ex</sub> = heat of detonation) were calculated with the EXPLO5 program<sup>99</sup> by using computed enthalpies of formation (Appendix B).

Since the development of RDX (1,3,5-Trinitro-1,3,5-triazacyclohexane or cyclonite), any newly synthesized energetic compound must face RDX, particularly in terms of detonation pressure and detonation velocity, which are very important parameters in secondary explosives. For these reasons, the energetic properties of RDX and two reference energetic salts containing inorganic anions have been added in Tab 13 for direct comparison. Also two reference energetic salts containing inorganic anions were added: 5-aminotetrazolium dinitramide (HAT-DN) and 5-aminotetrazolium nitrate (5-ATN). Energetic compounds should also be stable concerning temperature and high density, safe to handle, and cheap to synthesize. In terms of thermal stability, both **bTT** and **bTT-2** exceed the 200 °C benchmarks, and so vastly outperform RDX, as well as HAT-DN and 5-ATN. **bTT-2** slightly outperforms RDX and 5-ATN in detonation velocity, while its performance in detonation pressure is slightly lower. Concerning the experimentally determined sensitivities, **bTT** is insensitive to impact and friction while **bTT-2** is impact sensitive, with a

measured value in the range observed for other N-rich dinitramides: ammonium dinitramide (ADN) 5 J, triaminoguanidinium dinitramide (TAGDN) 2 J<sup>6</sup> and HAT-DN. On the other hand, **bTT-2** is friction insensitive, a significant result, inasmuch as other N-rich dinitramides, including HAT-DN, have high sensitivity towards friction (ADN 72 N, TAGDN 24 N).<sup>92</sup> **bTT-4** is impact sensitive and moderately sensitive to friction, while **bTT-5** is impact and friction insensitive and so is better performing than nitrate 5-ATN. Nitramide **bTT-2** can be considered as the most interesting energetic material within the set investigated, although its impact sensitiveness hinders use as main explosive. Altogether, the salt compounds described here could be of potential interest as propellant charges or as additives in propellant charges or gas generators.

## Chapter 4 Organic Polar Crystals

### 4.1 General aspects

In recent scenarios, human habits have changed dramatically due to the vertical development of information technology and telecommunications. Much attention has been paid to the investigation and development of new electro-optic materials and device fabrication techniques. In particular, the nonlinear optical (NLO) field is currently one of the most attractive research fields because of its constructive applications in optoelectronics, sensors, photonics, optical information processing, and disk storage.<sup>100–105</sup> The first interesting results of NLO applications were achieved by Franken *et al.* in 1961<sup>106</sup>, which showed the limited amount of materials suitable for non-linear frequency conversion. Nowadays, great efforts have been made in easy and fast delivery of information, which are achieved by introducing optical fibre.<sup>107,108</sup> In this technology, the information is enhanced between two electronic devices through the optical fibre channel, so requiring translation of the electronic to optic information. The translation can be performed by exploiting the Pockels effect, *i.e.* change of the index of refraction of a material by applying an external electric field. The Pockels effect is a typical second order (or quadratic) NLO effect. Another typical second order NLO effect is Second Harmonic Generation (SHG): the propagation of an electromagnetic wave of frequency  $\omega$  in a NLO active medium produces the wave with the same coherence but frequency  $2\omega$ . As for all NLO effects, the basic symmetry requirement is the absence of the inversion centre. To date, acentric inorganic crystals are widely used because of their high nonlinear optical properties, easy crystal growth, wide optical transparency domain and fast optical response time.<sup>109–111</sup> Moreover, inorganic NLO crystals usually have good thermal stability, high melting point and high mechanical strength. LiNbO<sub>3</sub>, KNbO<sub>3</sub> and BCB, among others, have been studied for device applications.<sup>111–113</sup> These materials have also been successfully used in commercial electro-optic modulators,

frequency doublers, mixers and parametric generators to give coherent laser radiation with high-frequency conversion efficiency in new regions of the spectrum, which is inaccessible by other conventional nonlinear crystal sources. However, the critical point is developing new materials with an increasingly high transmission rate maintaining a high electro-optic transmission efficiency. For this reason, the research on organic acentric crystals is more and more attractive because of highly polarized conjugate fractions that could meet the demands of a high electro-optical conversion rate.

Organic NLO materials are promising candidates for use in electro-optic modulators, optical switches, or all-optical signal processing due to the fast intrinsic response time, ease of processability, low optical loss, and high-molecular nonlinearity. Moreover, the molecular second-order optical nonlinearity (i.e. first hyperpolarizability) can be enhanced by increasing the length of the  $\pi$ -conjugation bridge and/or introducing stronger electron donor and acceptor groups into the constituting molecules. The necessary condition for the second-order NLO activity is the absence of the centre of symmetry. Anyway, obtaining crystals for NLO applications is generally tricky since, in addition to being polar and acentric, in terms of space group, the molecules of the compound must be oriented appropriately with respect to the relevant symmetry elements, in particular about the orientation of molecular directions which correspond to high coefficients of molecular nonlinearity in polar nonlinear molecules.<sup>114</sup> When using a chemical modification for developing novel organic NLO crystals, one of the main challenges is obtaining acentric crystal structures, i.e. structures with a non-centrosymmetric molecular alignment in the crystalline state. Analysing several NLO organic crystals with the highest second-order optical nonlinearity known to date, a common chemical structure, the so-called ‘acentric core structure’,<sup>33,115,116</sup> is apparent in many of these crystals as shown in Figure 55. When different

constituting molecules possess such an identical acentric core structure, the corresponding crystals show a strong tendency to form acentric crystal structures.

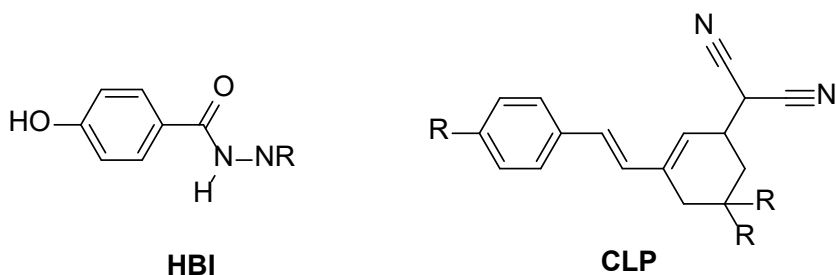


Figure 55. Acentric core structures of nonlinear optical organic crystals: HBI core: 4-hydroxybenzohydrazide, CLP core: configurationally locked polyene based on phenyltriene

The task of obtaining a non-centrosymmetric crystalline structure is a hard one and even more difficult is obtaining a non-centrosymmetric crystal that is also polar. In a polar crystal, there is one direction, at least, that is not transformed in the opposite direction by any of the symmetry operation allowed by the space group. That direction is the polar axis of the crystal. Since the centre of symmetry transforms each direction in the opposite one, polar crystals are non-centrosymmetric. However, not any acentric crystal is also polar, so that polar crystals are a subset of acentric crystals. Out of the 32 crystal classes, 20 match to non-centrosymmetric crystals (Hermann-Mauguin notation):

- **1, 2, m, 222, mm2, 4, -4, 422, 4mm, -42m, 3, 32, 3m, 6, -6, 622, 6mm, -62m, 23, -43m**

Of the non-centrosymmetric crystalline classes, only 10 are polar and are highlighted in red bold in the list above. Only 10-15% of acentric organic compounds do crystallize in acentric space groups.<sup>117</sup> In the search for acentric compounds, the simplest solution is to resort to chiral compounds. Also in this case, however, the probability of obtaining polar crystals is low, due to the fact

that the most frequent acentric space group for chiral compounds is  $P2_12_12_1$  (class 222) which is acentric but not polar.<sup>118</sup> Moreover, even within the set of compounds that do crystallize in a polar space group (e.g.  $P2_1$ ,  $Pca2_1$ , and  $Pna2_1$ ), in many cases, the independent molecule is placed with its charge transfer axis perpendicular to the polar binary screw axis,<sup>119–121</sup> giving rise to vanishing bulk nonlinearities.<sup>114</sup> In this context, the importance of crystal engineering can be fundamental. The characteristics of the molecular alignment in organic molecular crystals depend on both their secondary-bonding sites and the shape of the constituting molecules. These include utilizing strong directional intermolecular interactions, like H-bonding<sup>122,123</sup> and halogen-bonding<sup>124,125</sup>, or supramolecular method as inclusion compounds and co-crystals.<sup>126,127</sup> This is because electron-donor and electron-acceptor groups, utilized to promote molecular hyperpolarizability, through the contribute of first order electric dipole, possess partially positively charged atoms ( $\delta^+$ ) and partially negatively charged atoms ( $\delta^-$ ), respectively. However, as can be inferred, obtaining acentric polar crystals is still tricky.

## 4.2 Imines for NLO applications

4-hydroxybenzohydrazide (**HBI**) represents an example of acentric core structure. In literature are reported several imines obtained by condensation of **HBI** with aldehydes and aliphatic ketones that show the tendency to crystallize in acentric polar space groups, like  $Pna2_1$  or  $Cc$ . In some of them, polymorphism is present with an additional non-polar centrosymmetric phase. All the imine compounds, studied so far in our group, show at least one polar polymorph (Chart 11). This class of compounds could show potential piezoelectricity and NLO properties. In the case of imines with polymorphism, it has been studied that transition between different polar polymorphs can be topotactic (i.e. Single-crystal-to-single-crystal SCSC).<sup>34</sup> The role of **HBI** as a promoter for crystallization of compounds in polar space group is confirmed by the crystal structures reported on CSD. By using the

acentric core system **HBI**, as a quest (in which R group is any element or group), 149 hits are found. Now, if we exclude from this set 75 crystal structures that are solvates, which are crystalline solids that contains the molecules of solvent inside their crystal structure, or the same structure repeated at different temperatures, there remain 74 hits of which 24 are acentric polar (CSD REF CODES: BEXTAB, CABWUA, GITBAN, GOBMIV, GOBMIV01, HUCVIL, MAQVUX, MAQWIM, MAQXAF, MAQXEJ, MOSPEQ, MOSPEQ01, NUPPEU, OROQET, OYUGIA, PAQJID, PEDGOW, POYLAT, TEWLAL, VAJLAW, WACVON, QAHJEB). Thus, the frequency of acentric structures is about 31.6 %. This frequency is significantly higher than the global frequency of acentric crystal structures reported in CSD, which is about 22% (238,154 on 1,106,766 total determined structures).

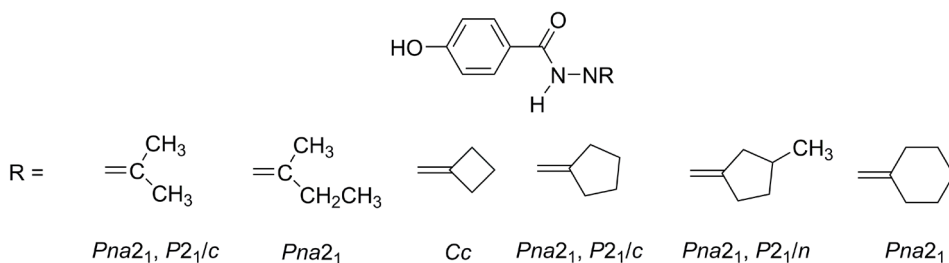
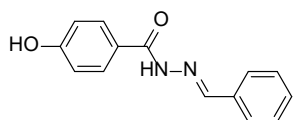


*Chart 11. Imines obtained by reaction of **HBI** with aliphatic ketones*

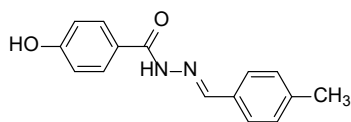
Moreover, it should be considered that the global datum of 22% for acentric structures in the CSD is overestimated because it also includes chiral compounds for which, of course, centrosymmetric space groups are not allowed.

In order to search for other non-centrosymmetric crystal structures that exploit the **HBI** core with potential NLO properties, 5 imines were synthesised by reaction of **HBI** with five aromatic aldehydes (Appendix A), as shown in chart 12.



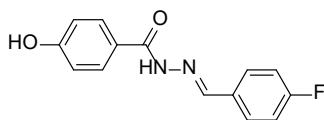
**Benzim**

(*E*)-*N'*-benzylidene-4-hydroxybenzohydrazide



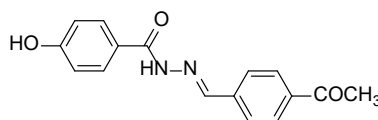
**Toluim**

(*E*)-4-hydroxy-*N'*-(4-methylbenzylidene)benzohydrazide



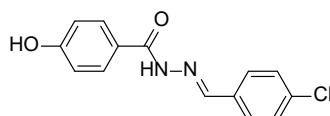
**Fluorim**

(*E*)-*N'*-(4-fluorobenzylidene)-4-hydroxybenzohydrazide



**Metoxim**

(*E*)-*N'*-(4-acetylbenzylidene)-4-hydroxybenzohydrazide



**Chlorim**

(*E*)-*N'*-(4-chlorobenzylidene)-4-hydroxybenzohydrazide

Chart 12 Imines obtained by the reaction of **HBI** with: benzaldehyde (**BENZIM**), 4-methylbenzaldehyde (**TOLUIM**), 4-fluorobenzaldehyde (**FLUORIM**), *p*-anisaldehyde (**METOXIM**), 4-chlorobenzaldehyde (**CHLORIM**).

**Benzim**, **Toluim** and **Fluorim**, are new compounds. The crystal structures of **Metoxim** and **Chlorim** are already described in literature<sup>128,129</sup> and the crystal structures reported are centrosymmetric (Ref Codes: HUCWOS, CECZOB). However, the thermal analysis and SHG measurement performed on the powder, prepared by us, give clues on the possibility of polymorphism for both compounds and, in particular, are the presence of one acentric polymorph.

#### 4.2.1 Thermal and crystallographic analysis

DSC measurements were performed on the five synthesized imines (Figure 56-60).

All DSC show a narrow endothermic peak at reported temperature in table 14.

Table 14. Fusion temperature of analysed compounds extracted from DSC curves.

Imines	$T_m$
<b>Benzim</b>	230°C
<b>Toluim</b>	250°C
<b>Fluorim</b>	237 & 250°C
<b>Metoxim</b>	220°C & 230°C
<b>Chlorim</b>	242 °C

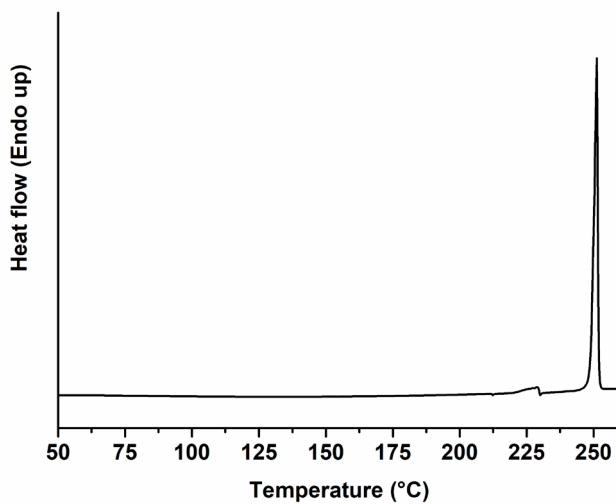


Figure 56. DSC curve of **Benzim**. Heating rate 10 K/min.

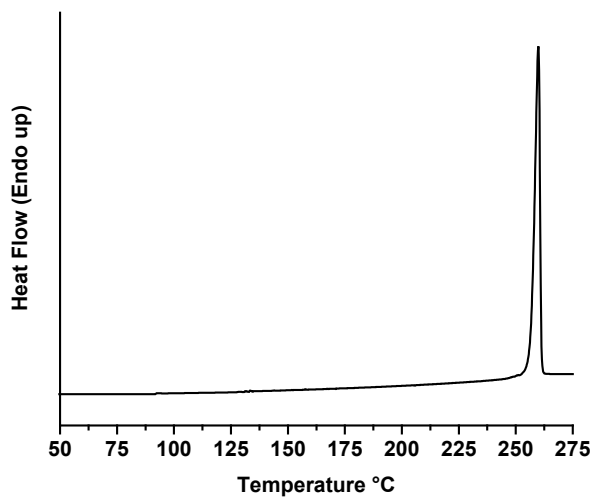


Figure 57. DSC curve of **Toluim**. Heating rate 10 K/min.

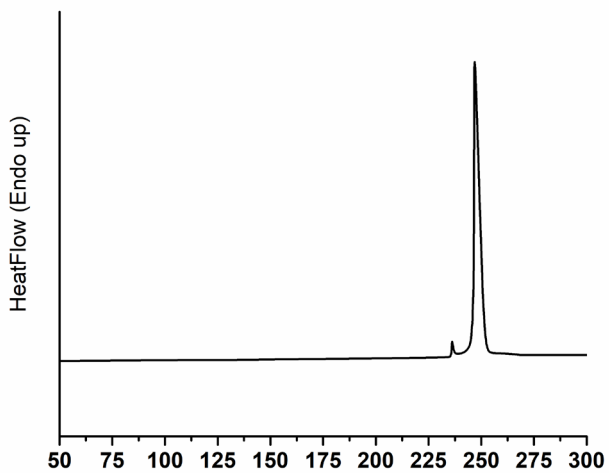


Figure 58. DSC curve of **Fluorim**. Heating rate 10 K/min.

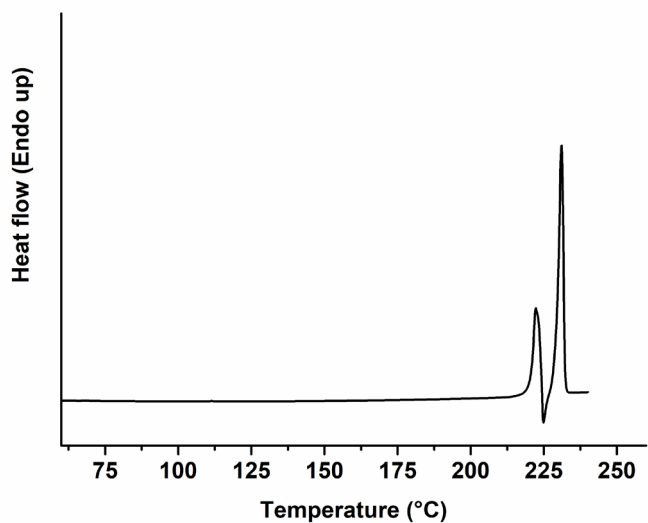


Figure 59. DSC curve of **Metoxim**. Heating rate 10 K/min.

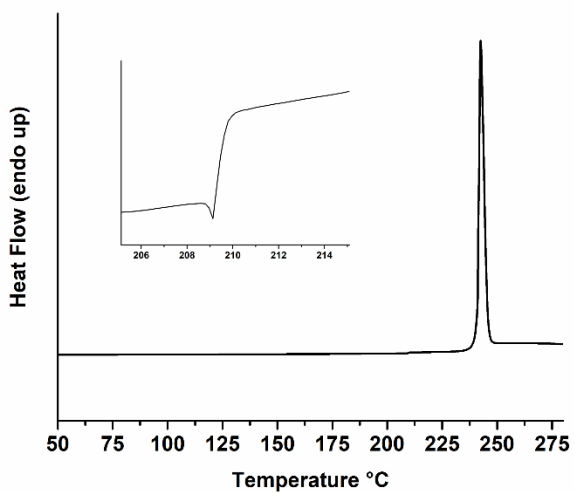


Figure 60. DSC curve of **Chlorim**. Heating rate 10 K/min.

From the DSC analysis, it is possible to highlight only for **Metoxim** clear evidence of polymorphism. In fact, there is a first endothermic peak at 220°C, followed by an exothermic crystallization with a final endothermal at 230°C. This suggests that for the analysed sample, there was more than one crystal phase. The optical analysis in polarised light (POM), performed with a polarizer microscope ZEISS Axiolab supported with a Mettler Toledo FP90 heating stage, also supported this suggestion. The observation carried out in temperature has evidenced the partial fusion and a successive complete fusion to the temperatures brought back from the DSC curve of **Metoxim**. However, despite several crystallization tests, it was not possible to obtain suitable single crystals to perform XRD on the supposed polymorphic phase. For **Benzim, Toluim, Fluorim and Chlorim** the optical analysis did not show anomalies with respect to DSC thermograms. The acentric core backbone, **HIB**, is characterized by the alternance of potential H-bonding donor (D) and acceptor (A) groups (Figure 61).

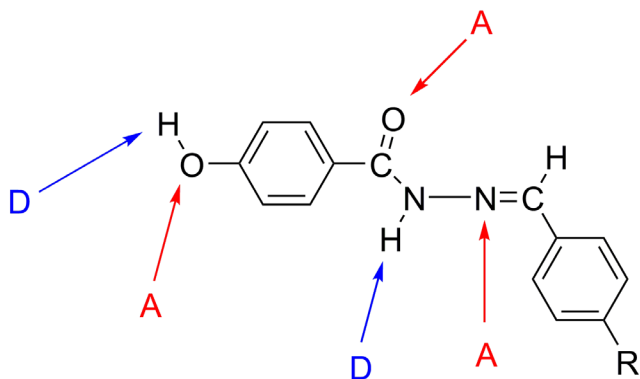


Figure 61. Potential H-bonding acceptor (A) and donor (D) groups for **HIB**.

However, it can be considered, preliminary, that the acceptor strength of phenolic O-H is reduced by the partial conjugation with the benzene ring. Similarly, the iminic nitrogen is sterically hindered and poorly accessible by possible donors, due to the presence of the hydrogen atom on the ortho position of phenyl ring,

coplanar with the imine group because of the  $\pi$  conjugation. Therefore, there are two donors in the molecules and only one acceptor that will most likely act as a bifurcated double acceptor.

The X-ray molecular structure of orthorhombic  $Pna2_1$  **Benzim** is shown in Figure 62. In both the packing views of **Benzim**, Figure 62 b,c is clearly evident the polar packing. In fact, the asymmetric unit is slightly tilted compared to the polar  $c$  axis and then the end-to-end molecule vectors are basically iso-oriented. The ORTEP diagram highlights the torsion angle,  $158(4)^\circ$ , between the phenyl ring and carbonyl group, with a dihedral angle between phenyl least-square planes of  $\tau = 27.0(2)^\circ$ . The molecule exists in trans configuration with respect to the C8=N2 (1.280(2) Å) bond and the torsion angle C9-C8-N2-N1 =  $176.3(3)^\circ$ . As can be seen from the packing diagram, intermolecular N-H $\cdots$ O, O-H $\cdots$ O and C-H $\cdots$ O hydrogen bonds (Table 15) link the molecules and these hydrogen bonds may be effective in the stabilization of the crystal structure bond.

Table 15 H- bonding geometry of **Benzim**. symmetry code list: i)  $-\frac{1}{2} + x, \frac{1}{2} + y, z$  ii)  $1-x, -y, 1/2 + z$

<b>D-H<math>\cdots</math>A</b>	<b>Distances Å</b>	<b>D-H<math>\cdots</math>A angle</b>
<i>N1-H1N<math>\cdots</math>O2<sup>i</sup></i>	2.150(4)	165(4) °
<i>C8-H8<math>\cdots</math>O2<sup>i</sup></i>	2.689(3)	149(3) °
<i>O1-H1O<math>\cdots</math>O2<sup>iii</sup></i>	1.930(5)	162(4) °

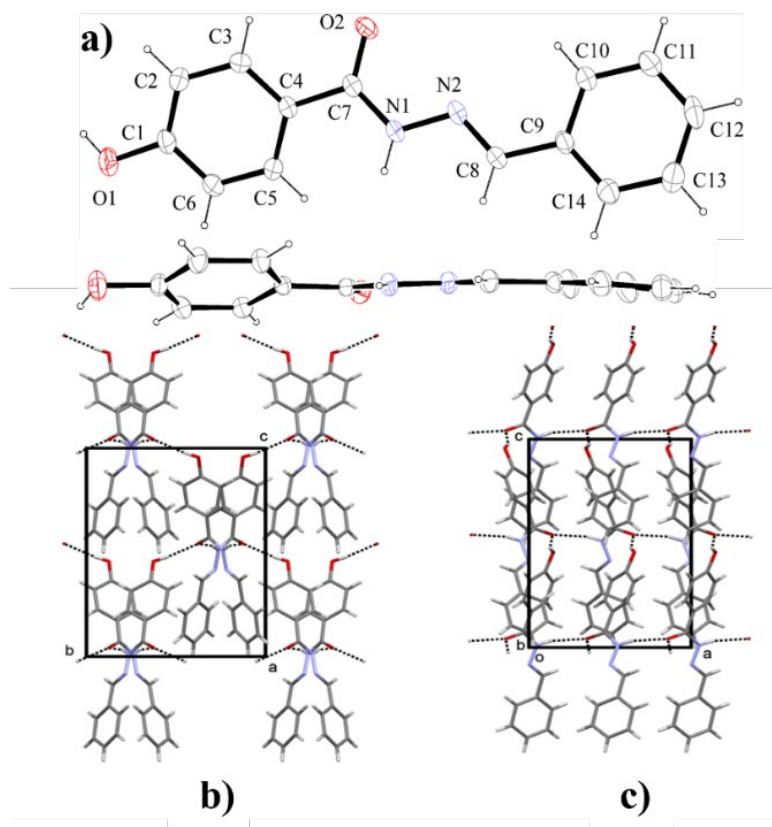


Figure 62. a) Ortep images of **Benzim**. In both case, thermal ellipsoids are drawn at 30% of probability level. b) packing along *a* axis c) packing along *b* axis.

Amide-like chains formed by H bonding between the N1–H donor and the O2 acceptor run along *a*; the glide plane perpendicular generates them to the *b* axis. Other chains are generated through H bonding between the O1–H donor and the imino O2 acceptor. These chains run parallel to *c* and are wrapped around the  $2_1$  screw axis.

The X-Ray molecular structure of orthorhombic  $P2_12_12_1$  **Toluim** is shown in Figure 63. In this structure, which is non centrosymmetric, the arrangement of end-to-end molecule vectors is non-polar due to the three mutually orthogonal  $2_1$  screw axes. Also here, the molecule is in *trans* configuration with respect to the

C8=N2 (1.271(6) Å) bond. The two phenyl rings are twisted with dihedral angle  $\tau = 71.68(4)^\circ$ . The H-bonding pattern involves the same acceptor and donor groups of **Benzim**.

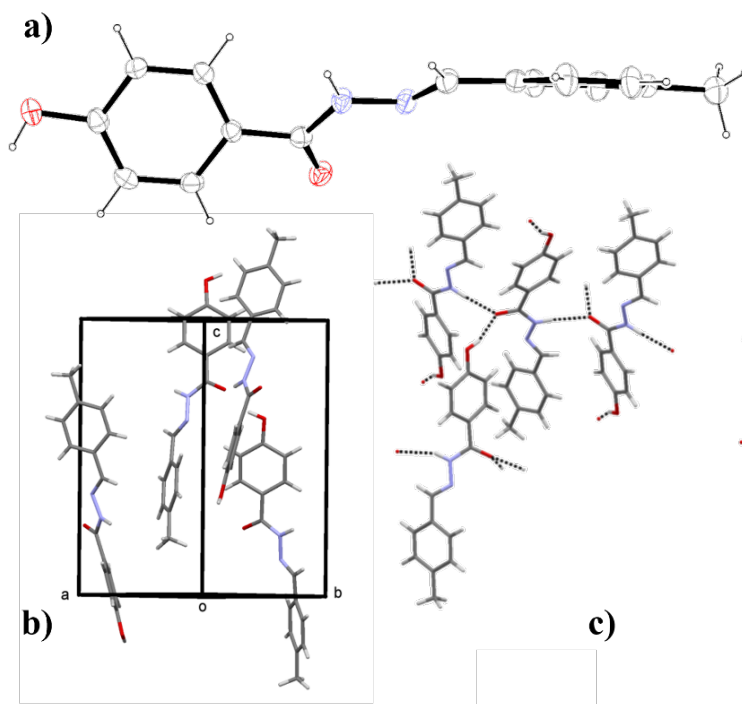


Figure 63. a) Ortep images of **Toluim**. Thermal ellipsoids are drawn at 30% of probability level. b) packing along  $a+b$  axis c) H-bonding pattern.

Differently from **Benzim** and **Toluim**, **Fluorim** crystallizes in the centrosymmetric space group, *Pbca*, with two independent molecules (Figure 64). The arrangement of end-to-end vectors is anti-parallel. The *trans* conformation, C8=N2 (1.265(3) Å) and C22=N4 (1.268(2) Å), is still persistent, while the two phenyl ring are slightly tilted with a dihedral angle of  $\tau_1 = 11.76(3)^\circ$  and  $\tau_2 = 23.5(4)^\circ$ .

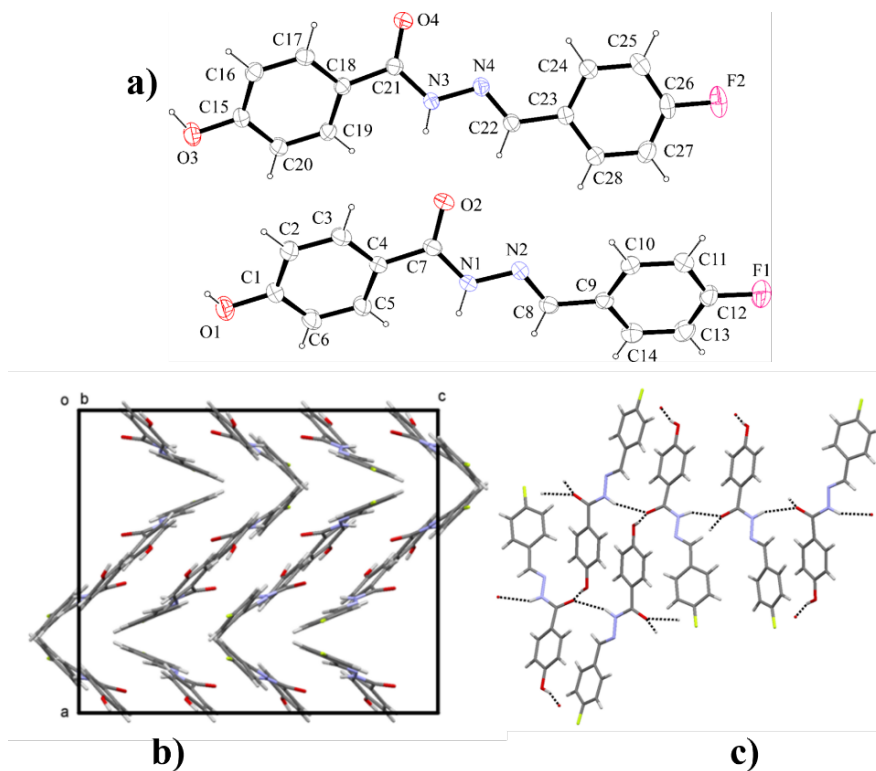


Figure 64. a) ORTEP images of **Fluorim**. Thermal ellipsoids are drawn at 30% of probability level. b) packing along b axis c) H-bonding pattern.

The molecules are held together by strong H-bonding between N-H and O-H donor groups and bifurcated acceptor carbonyl oxygen atoms (Table 16).

Table 16 H- bonding geometry of **Fluorim**, symmetry code list: i)  $x, y, z$  ii)  $1-x, -\frac{1}{2} + y, -\frac{1}{2} - z$ , iii)  $1-x, \frac{1}{2} + y, -\frac{1}{2} - z$ , iv)  $x, \frac{1}{2} - y, \frac{1}{2} + z$

<b>D-H...A</b>	<b>Distances Å</b>	<b>D-H...A angle</b>
$N3-H3N...O2^i$	2.240(4)	149(2) °
$O3-H3...O2^{ii}$	1.876(2)	164(2) °
$O1-H1O...O4^{iii}$	1.933(5)	172(3) °
$N1-H1N...O4^{iii}$	2.314 (3)	154(2) °

#### 4.2.2 SHG measurements

All non-centrosymmetric molecular crystals are potential candidates for quadratic nonlinear optical (NLO) materials because they can show second harmonic generation (SHG), electro-optic modulation (Pockel effect).<sup>130</sup> Anyway, not all materials are suitable for applications due to their non-optimal secondary properties, like low optical damage threshold, sublimation, fragility, low hardness and photochemical stabilities, narrow transparency window and occurrence of phase transition. However, acentric materials must be first screened for their SHG response and, if this response is good, then an effort to study and accurately characterize their NLO properties is justified. SHG measurements were hence performed, as preliminary NLO characterization, on the powder compounds. The second harmonic generation (SHG) measurements were performed via a home-built optical setup designed for polarization-resolved SHG, allowing to control the polarization state of the impinging linearly polarized fundamental wave and monitoring the independent component of the second harmonic electric field (APPENDIX B). The quantitative results obtained from the SHG investigation are reported in the histogram (Figure 65). The data use urea ( $\text{CO}(\text{NH}_2)_2$ ) as the reference substance.

The histograms indicate the SHG signal effective value, proportional to the measured second harmonic intensity divided by the square of the fundamental beam energy and choosing units that assign a value of 100 to the reference sample. Equivalently, the effective second harmonic efficiencies are expressed as % units with respect to the urea sample.

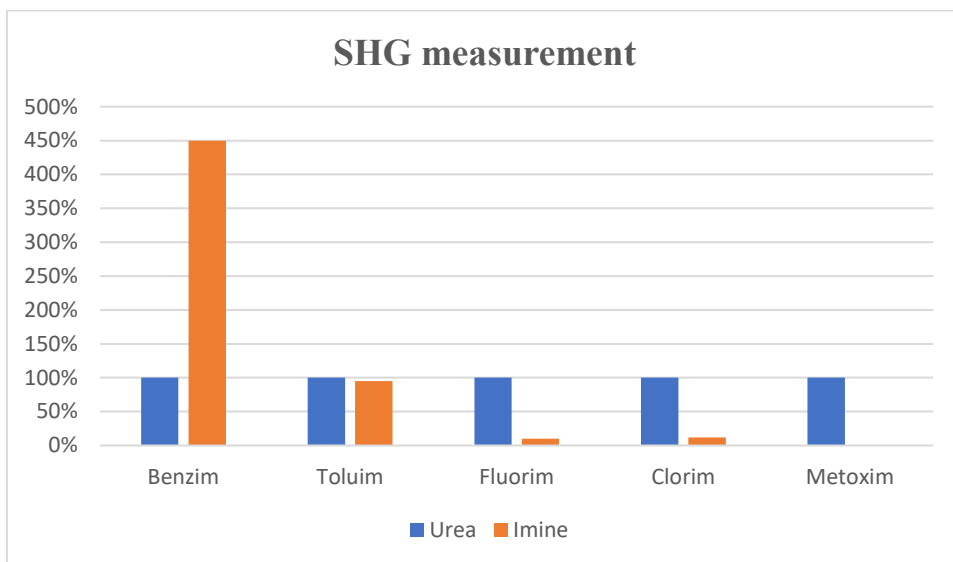


Figure 65 SHG measurement performed of imines powder samples. Urea is the used reference.

Out of the five analyzed imines, only **Metoxim** do not show SHG signal. This result indicates that the second crystal phase, evidenced by the DSC analysis, is also centrosymmetric. **Fluorim** and **Chlorim**, on the other hand, show a weak but detectable SHG signal, 0.47% and 2%, respectively, even though the known crystal structures are centrosymmetric in both cases. This could be a clue of the presence of a second non-centrosymmetric polymorphic phase for **Fluorim** and **Chlorim**. Actually, some evidence of polymorphism is present in the DSC thermograms of Figures 58 and 60, but any crystallization attempt has given the centrosymmetric phase. **Toluim** and **Benzim**, show a remarkable SHG signal because the samples investigated only contain the acentric phase. **Benzim**, in particular, exhibits an interesting SHG signal. This coupled with the possibility of growing large and regular shaped crystals, Figure 66, makes **Benzim** a potential compound for further measurements, for instance Terahertz (THz) wave generation. THz photonics is a relatively new photonic field based on THz electromagnetic waves with a frequencies ranging from 0.1 to 30 THz.

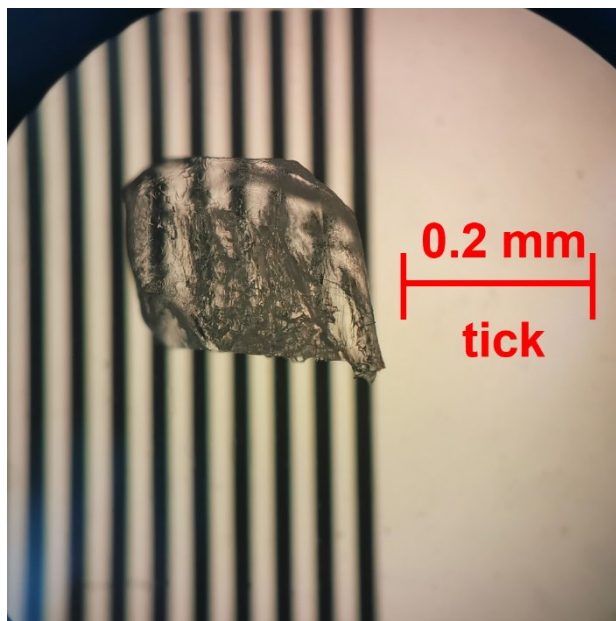


Figure 66. *Benzim* Single crystal POM view.

## 4.3 Mechanically Responsive Molecular Crystals

### 4.3.1 General aspects

Molecular crystals have been long studied by chemists from a crystallographic or crystal engineering perspective, but they are only recently being recognized for their potential as dynamic materials that can be incorporated into devices.<sup>37,131–133</sup> During the dynamic processes, strong covalent bonds are conserved while weaker intermolecular interactions can be broken and reshaped at a relatively low energy cost. In this way, dynamic crystals have a unique set of properties that adds a new class of materials to the global materials property space.<sup>134</sup> The long-range three-dimensional ordered structure of molecular crystals enables fast or even ultrafast transduction of energy that results in rapid progression of externally induced mechanical, electrical, or other perturbations across the material. For instance, a recent analysis of martensitic organic crystals as soft and lightweight actuators<sup>135</sup> has shown that these materials can convert thermal energy into work with forces on the order of 10–100 mN and force-to-weight ratio on the order of  $10^4$  with a very rapid transition.<sup>136</sup> An important and rarely recognized asset of organic crystals is their lightweight, which may be useful in applications that require minimal weight per volume material. If implemented in devices, such crystals could take the role of actuators, valves, gates, fuses or semi-conductors with piezoelectric and electromagnetic properties.<sup>137,138</sup> Application of molecular crystals as optical waveguides is being extensively explored recently.<sup>139,140</sup> The amplification of microscopic molecular motions so as to produce a controlled macroscopic body effect is a challenging task because it requires the coherent, collective and ordered movement of each molecule of a whole macroscopic set.<sup>141</sup> Actually, this is just what happens in single-crystal-to-single-crystal (hereafter SCSC) transitions.<sup>142</sup> The mechanical deformation of the crystal associated with a SCSC transition can lead to the appearance of impressive dynamical phenomena:

reshaping, bending, twisting, hopping, explosion and scattering of the debris (Figure 67).<sup>143–146</sup>

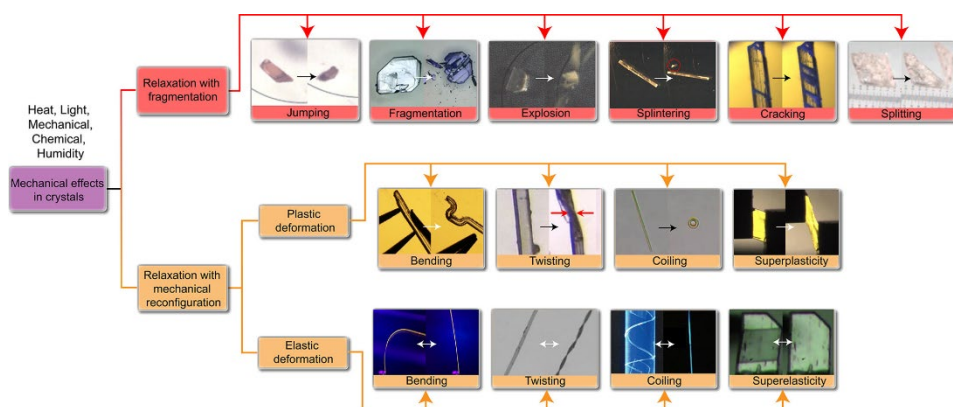


Figure 67. General classification of mechanical effects of molecular crystals. Figure taken from ref. 131.

In the case of SCSC transitions, the external action producing the body motion is the latent heat of transition (thermosalient crystals), but it can also be light, as in the case of photosalient crystals.<sup>147</sup> Studies into the macroscopic manifestation of these dynamic effects were initially driven by curiosity and serendipity, and since then have evolved as one of the most vibrant research directions of crystal engineering and solid-state chemistry. There are many open problems with mechanically responsive molecular crystals. For instance, the role of specific intermolecular interactions, *i. e.* soft and non-directional vs hard and directional, in triggering and coherently propagating the molecular displacements that actuate the transition, the relation between the packings of the phases involved in the transition and the dynamic phenomena recorded at the macroscopic level. Moreover, a challenging issue preliminary to any possible application in devices, is the gaining of strict control of the mechanical effects associated with the transition.

Here is reported the study of a new dynamic crystal of **Toluim** solvate with NMP, henceforth **Tol\_NMP** (Chart 13).

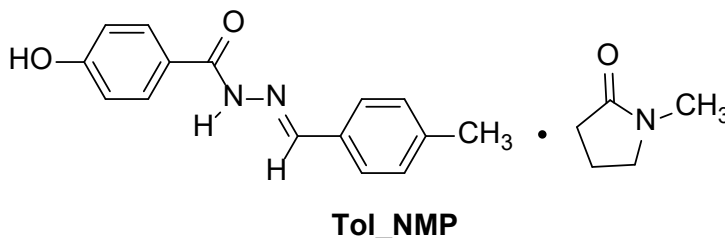


Chart 13. *Toluim* solvate with NMP

This solvate crystal is a chemical analogue to the thermosalient crystal 4-hydroxy-*N'*-(2-propylidene)benzohydrazide already described.<sup>148</sup> The compound is trimorphic and the phase transition of one of its polymorphs occurs between 100–115 °C by retention of the single crystal form, and is accompanied by snake-like crystal deformation. The phase transition, which occurs between centrosymmetric and non-centrosymmetric phase, is reflected in the switching in the non-linear optical properties of the material. The fast switching could find application as actuator in NLO materials.

#### 4.3.2 Crystallographic analysis of Tol\_NMP phases

Three polymorphic phases of **Tolu\_NMP** have been determined:

- I. **Tol\_NMP1** crystallizes in orthorhombic space group  $P2_12_12_1$
- II. **Tol\_NMP2** crystallizes in monoclinic space group  $P2_1/c$  with two independent imine and NMP molecules
- III. **Tol\_NMP3** crystallizes in triclinic space group  $P-1$  with two imine and NMP independent molecules

In the elementary cell of **Tol\_NMP1**, the four molecules have different orientations with a packing highly influenced by strong H-bonds between O-H and N-H donor and imine and NMP carbonyl C=O acceptor groups (Figure 64).

This pattern of hydrogen bonds and the basic conformational feature of the imine molecule, is kept in all three polymorphs. The undulation of the layers is mainly due to NMP molecules being not coplanar with the imine molecules they form hydrogen bond with, as evidenced in Figures 68 (a) and (b).

Table 17 H-bonding geometry of *Tol\_NMP1*, symmetry code list:*i* -*x*, - $\frac{1}{2}$ + *y*,  $\frac{1}{2}$ - *z* ii) *x*, *y*, *z*.

<i>D-H...A</i>	Distances Å	D–H...A angle
<i>O1-H1N...O2<sup>i</sup></i>	1.765(2)	166.0(3) °
<i>N1-H1A...O3<sup>ii</sup></i>	2.689(3)	175.0(4) °

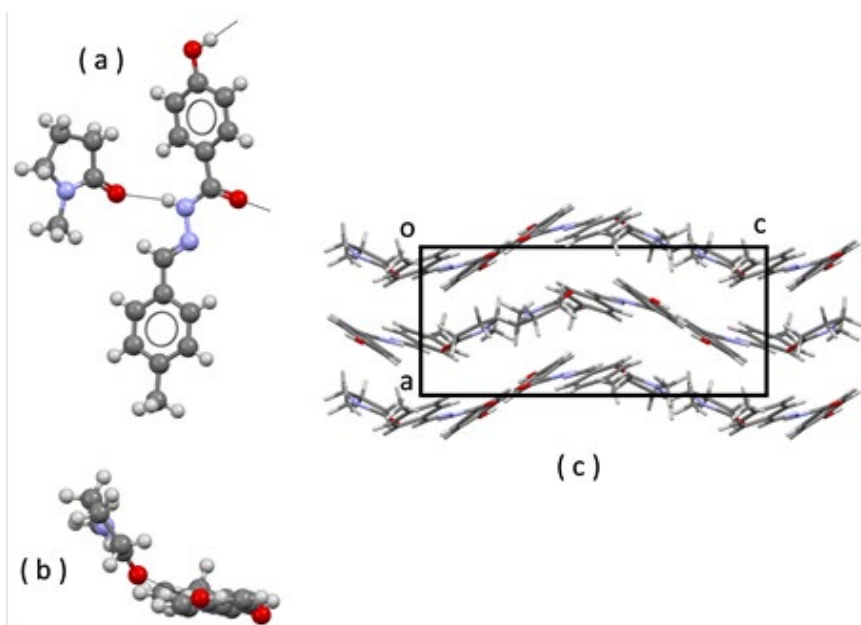


Figure 68. Crystal structure of *Tol\_NMP1*. (a) face view of the independent unit; (b) independent unit viewed approximately along the line from the phenolic oxygen to the terminal C methyl; (c) packing of *Tol\_NMP1* viewed down *b*.

**Tol\_NMP2** crystal structure has two imine molecules and two (disordered) NMP molecules crystallographically independent. In the crystal, molecules are all

parallel to each other. The NMP molecules that form H-bond with N-H of imine molecules are almost coplanar with them. As in **Tol\_NMP1**, the structure is characterized by layers of molecules that, however, are no longer undulated but basically flat, and are piled along the diagonal *a-c*, as shown in Figure 69(c).

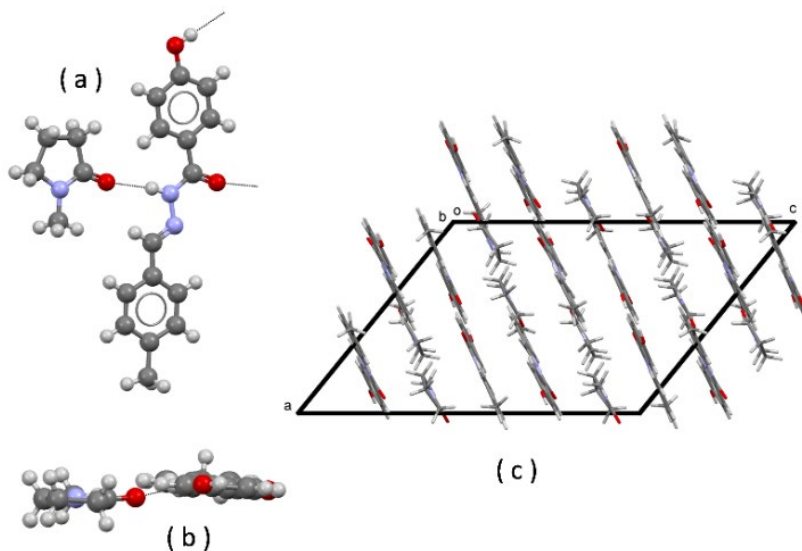


Figure 69. Crystal structure of **Tol\_NMP2**. (a) face view of half of the independent unit (only one position of the disordered NMP molecule is shown); (b) independent unit viewed approximately along the line from the phenolic oxygen to the terminal C methyl; (c) packing of **Tol\_NMP2** viewed down b.

The SCSC transition takes place between these two polymorphic phases. Due to SCSS nature of transition, it is possible to find for **Tol\_NMP1** a monoclinic supercell analogous to the unit cell of **Tol\_NMP2**. The lattice vectors of the supercell are obtained by applying the matrix transformation *M* to the column of the orthorhombic lattice vectors:

$$(1) \quad M = \begin{pmatrix} 2 & 0 & 0 \\ 0 & 1 & 0 \\ -2 & 0 & 1 \end{pmatrix}$$

The lattice parameters of **Tol\_NMP** in the new supercell are (at -100 °C)  $a=14.758(2)$  Å,  $b=14.380(2)$  Å,  $c=22.658(3)$  Å,  $\beta=130.644(6)^\circ$ ,  $V=3648.5(9)$  Å<sup>3</sup>, and the space group would be  $P2_1$ . This unit cell is analogous to **Tol\_NMP2** (Appendix C). Some hints for the transition mechanism can be deduced by the analysis of Figure 70.

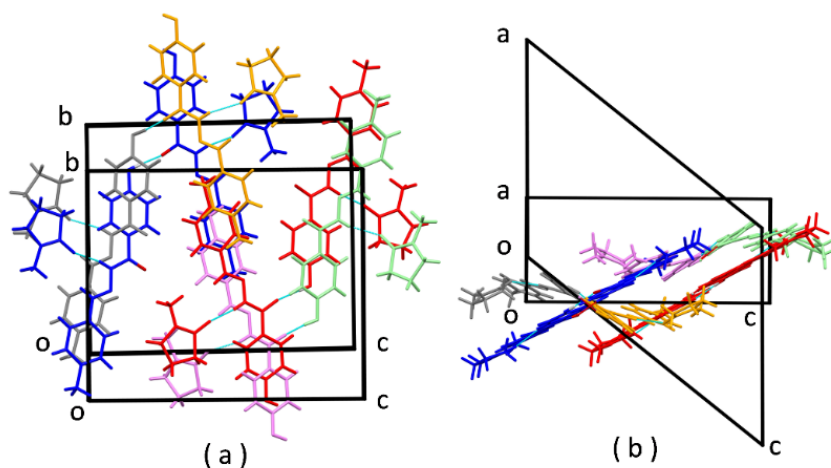


Figure 70. Superposition of unit cells of **Tol\_NMP1** (at -100 °C) and **Tol\_NMP2** (at -100 °C). (a) projection down  $a$ ; (b) projection down  $b$ .

The four molecules present in the cell of the orthorhombic  $P2_12_12_1$  phase are represented with different colours: grey (independent molecule), light green (generated by the  $2_1$  axis parallel to  $a$ ), orange (generated by the  $2_1$  axis parallel to  $b$ ), violet (generated by the  $2_1$  axis parallel to  $c$ ). The two independent molecules of the monoclinic  $P2_1/c$  **Tol\_NMP2** are represented with blue and red colours. The orthorhombic and monoclinic cells are indicated in the correct relative orientation given by the matrix transformation (Eq. 1 in the main text); moreover, the  $2_1$  axis parallel to  $b$  of the orthorhombic cell has been put in coincidence with a  $2_1$  axis of the monoclinic lattice, in particular the  $2_1$  axis having  $a = 0$  and  $c = 0.25$ , as it is evident from Figure 70 (b).

The grey and orange molecules of the orthorhombic phase (related by  $2_1$  around  $b$  and H-bonded to each other through  $\text{O—H}\cdots\text{O=C}$ ) can go onto two H-bonded blue molecules of **Tol\_NMP2** by a skew rotation around the  $2_1$  axis (about  $30^\circ$ ) followed by a skew translation parallel to the  $2_1$  axis (about  $2.5 \text{ \AA}$ ). On the other hand, the green and violet molecules of the orthorhombic phase (H-bonded to each other through  $\text{O—H}\cdots\text{O=C}$ ) can go onto two H-bonded red molecules of **Tol\_NMP2** mainly by a skew translation parallel to  $b$  (about  $2.5 \text{ \AA}$ ), but in the opposite direction as for the grey and orange molecules, followed by small rotation perpendicular to  $b$ , around  $a+c$ . During these movements, there is room for the NMP molecules to undergo a  $180^\circ$  rotation around the direction of the H-bond  $\text{C=O}\cdots\text{H—N}$ , so becoming disordered in the monoclinic phase. Moreover, during these small movements, the topology of H bonds is kept. The transition can be considered non-diffusive and displacive. In Figure 71, a rational picture of the SCSC transition at a molecular level in a stop-motion frame is reported. Single crystals of **Tol\_NMP1** can be easily grown in the form of prisms elongated in the direction of the crystallographic  $a$  axis (Appendix B). During the transition, the disposition of the layers piled up on each other is kept, and the layers become flat. However, in **Tol\_NMP1** the layers are piled along  $a$ , while in **Tol\_NMP2** they are piled along  $a-c$  of the monoclinic cell. So, in the *locus* in which the transition starts, the front of **Tol\_NMP2** grows and advances along  $a-c$ , therefore forming an angle with respect to the crystal of **Tol\_NMP1** which is exactly defined, because it is the angle,  $30^\circ$ , between the axes  $a$  and  $a-c$ .

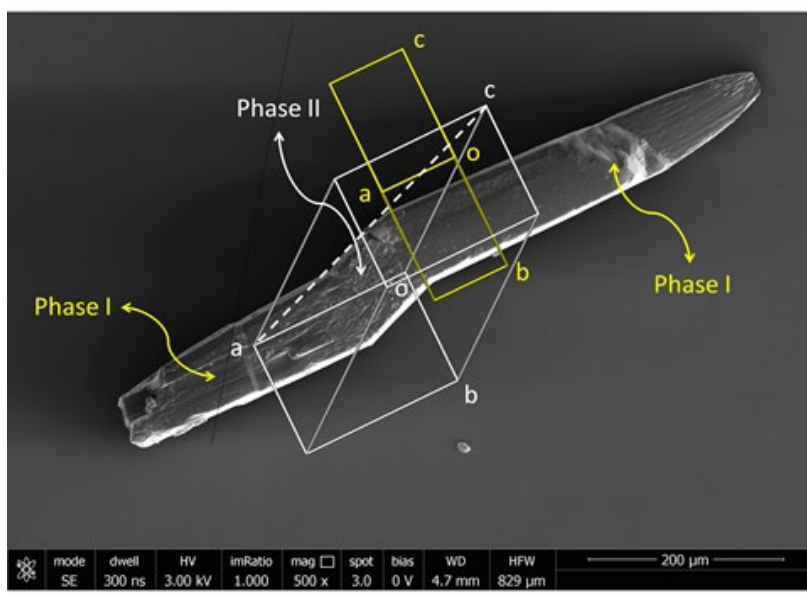


Figure 71. SEM image of a triphasic crystal of **Tol\_NMP** frozen during the transition from phase I to phase II. Superimposed are the unit cells of phase I (in yellow) and phase II (in white), in the correct relative orientation. The dashed line corresponds to the *a-c* direction of the monoclinic unit cell.

After the SCSC transition is completed, the final orientation of the single crystal of **Tol\_NMP2** is rotated exactly of  $30^\circ$  as compared to the initial position of the single crystal of **Tol\_NMP1**. So, there is strict, accurate and absolute control of the macroscopic rotation angle. This, of course, is due to the fact that in the amplification from the micro to the macro scale, angles between crystallographic directions (or planes) are unchanged, while distances between points are not. So, in the present case, the rotation angle is exactly preserved in the amplification from the micro to the macro scale.

The crystal structure of **Tol\_NMP3**, which is not immediately relevant to the dynamic properties, was also determined (Figure 72). The unit cell of **Tol\_NMP3** is similar to **Tol\_NMP1**, although there is no relation between the two lattices, neither with **Tol\_NMP2**. The pattern of H bonds is analogous to the other two polymorphic phases, and the arrangement of NMP molecules is like **Tol\_NMP2**.

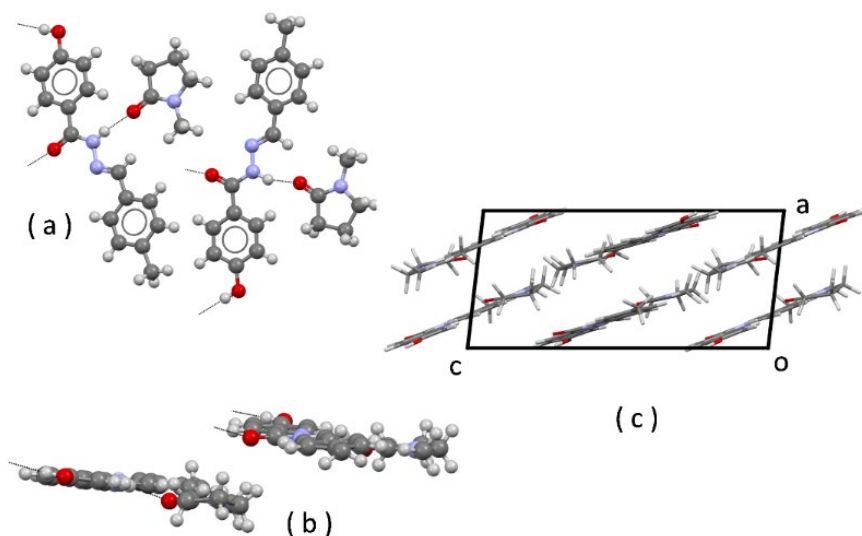
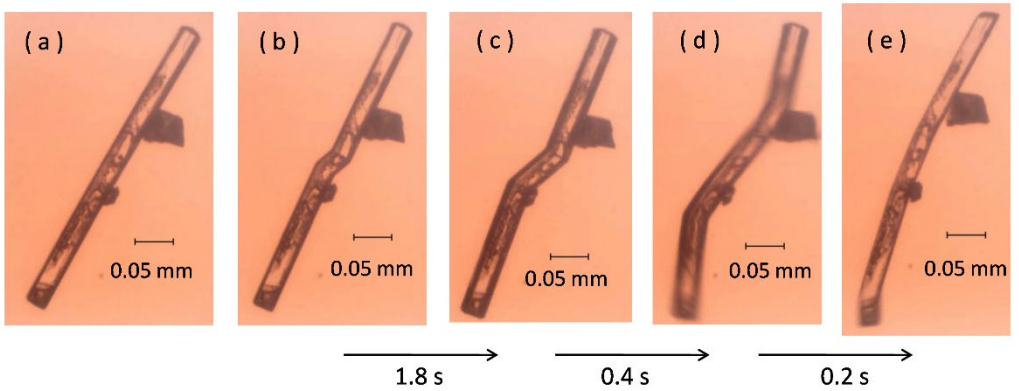


Figure 72. Crystal structure of *Tol\_NMP3*. (a) face view of the independent unit (b) independent unit viewed approximately along the line from the phenolic oxygen to the terminal C methyl; (c) packing of *Tol\_NMP3* viewed down b.

### 4.3.3 Dynamic behaviour

The transition was observed in the temperature range 110-120 °C depending on the morphological features of the crystal specimen (thickness, polish, regularity). The dynamic behaviour of crystals at the transition I-II is manifold and strongly depends on several factors that include the morphology of single crystals, the way they are constrained, the face the crystal is standing on, the degree of perfection of the crystals and, therefore, the temperature of transition, and also how long the transition lasts. Best dynamic performances are observed in slender single crystals, as compared with thicker ones.

In some cases, the transition starts in the middle of the crystal and propagates towards the tips (Figure 73 and Figure 74), also producing a flipping (Figure 74(e), (f)).



*Figure 73 Snapshots taken during the transition I-II of the single crystal. The time interval between some consecutive snapshots is also indicated. Photo (a) shows the crystal in phase I before the transition.*

In the case of thin, long crystals, with the transition starting at one tip, the whole movement of the crystal is a rotation of about  $30^\circ$  around the fixed tip. This is accomplished through lateral shifts of consecutive slices of the crystal, in a sort of snake-like motion. When both the tips are fixed, the bending deformation propagates along the crystal, leaving, in the end, the crystal in its original position

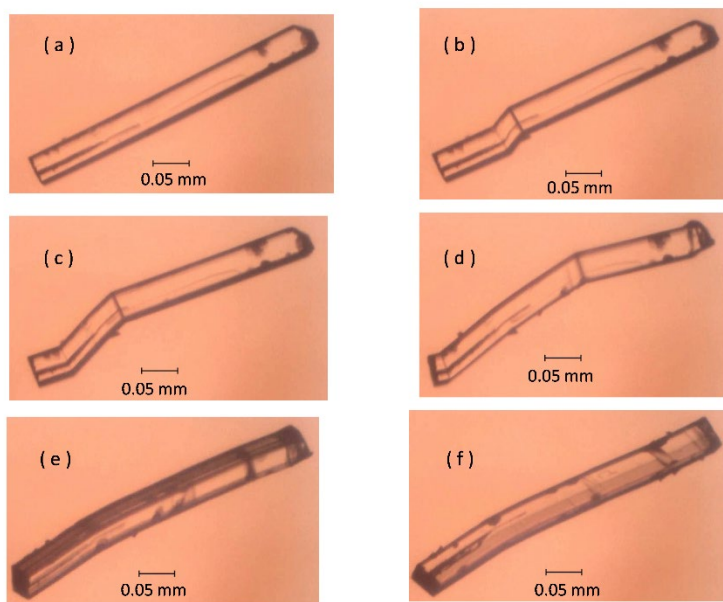


Figure 74. Snapshots taken during the transition I-II of the single crystal of movie 2. The time interval between some consecutive snapshots is (b)  $\rightarrow$  (c) 2.4 s; (c)  $\rightarrow$  (d) 1.1 s; (d)  $\rightarrow$  (e) 1.3 s; (e)  $\rightarrow$  (f) 1.9 s. Photo (a) shows the crystal in **Tol\_NMP1** before the transition.

In other specimens, the transition occurs very rapidly, and in this case, the crystal undergoes rapid movements, eventually breaking apart. The transition was confirmed by DSC analysis (Figure 75). The endothermic signal centred at 118 °C in the first heating run has  $\Delta H = 2.2$  kJ/mol and is related to the SCSC transition from **Tol\_NMP1** to **Tol\_NMP2**; the DSC analysis also demonstrates that the transition is monotropic because it is no longer observed either on cooling or in the second heating run. A comparison with the TGA analysis (Figure 76) is also useful. The TGA run of crystals of **Tol\_NMP1** shows a first weight loss (29 %) in the range 130-150 °C, which clearly corresponds to the loss of N-methylpyrrolidone solvent (the theoretical value is 28 %). After the loss of the solvent, the sample is stable up to melting (275 °C).

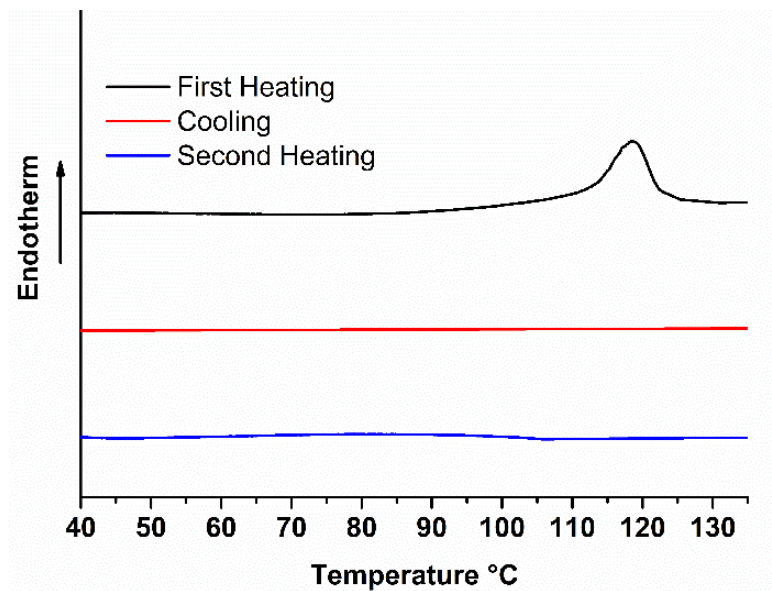


Figure 75 DSC thermograms of single crystals of **Tol\_NMP1**. Scanning rate 10 K/min, under N<sub>2</sub> flowing atmosphere.

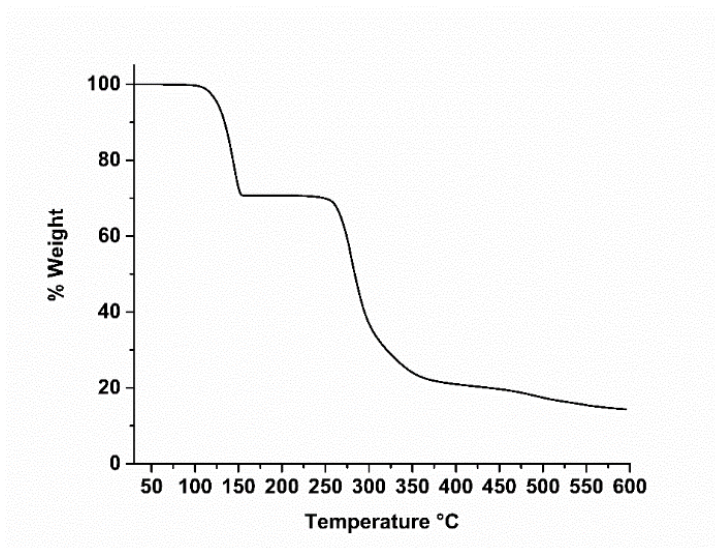


Figure 76 TGA analysis of **TolNMP1**. Heating rate 10 K/min under flowing N<sub>2</sub>.

## Chapter 5 Conclusions

The thesis reports on the synthesis and characterization of several novel compounds for advanced materials applications, including non-linear optics, high-energy density materials compounds, photoreactive materials, and mechanically responsive crystals. The materials have been designed and prepared through a careful analysis of the supramolecular synthons, showing the power of the Crystal Engineering approach, which proves to be an interesting tool and with a wide application range. The rational design of the novel materials is achieved with the employment of noncovalent interaction network, *i.e.* hydrogen bonds and chalcogen bonds, in order to have a preferential organization of molecules and ions in the solid-state. The fine manipulation of the molecular self-assembly represents the heart of this project thesis culminating with the design of materials with desired properties that represents the ultimate goal of crystal engineering. Designing a novel material with targeted properties demands a deep understanding of the crystal material features in relation to its mechanical properties. Thus, it is possible to state that the concept of this doctoral thesis strictly follows the three logical steps of crystal engineering: the study of molecular interactions, the study of crystal packing and the study of crystal properties. Firstly, in Chapter 2, the effect of chalcogen bonding on the structure and packing of fused-ring heteroaromatics and coordination polymers was discussed. A deeper and more fine understanding of this noncovalent interaction could be useful for the realization of different materials in which the presence of a chalcogen atom in the molecular backbone could change the basic paradigm of crystal packing of fused-ring hydrocarbons. In fact, for the 2D coordination network polymers the chalcogen bonds interaction works on both the crystal packing and the coordination geometry of the Copper(II) metal centres.

In Chapter 3, the tautomeric behaviour of N-rich heterocyclic compounds and their application was investigated. The ligand properties of a pyrazine

functionalized triazolo-triazole derivative (**TT9**) were proven in solution, and stable complexes were isolated and characterized in the solid-state. A computational analysis predicted the most stable tautomer/conformer of the neutral free ligand as the *2H/s-trans*, and this result was indeed experimentally confirmed by solving its structure in the solid-state. In addition, by tailoring a proper metal coordination it was possible to isolate the elusive *3H* tautomer. The high versatility and potentiality of **TT9** as molecular building block is accomplished by the observation of hybrid organic-inorganic salts structurally arranged in perovskite like motifs. Another N-Rich triamino-bistriazole derivative (**bTT**) was deeply investigated regarding its tautomerism and acid-base properties. The well-defined pH range in which every single form is predominant in solution allowed the selective crystallization of the different ionic forms. With the aim of obtaining high-energy-density materials (HEDMs), the rational design of **bTT** based salts was performed: all the ionic species of **bTT** were obtained and structurally characterized by XRD. For some of them containing energetic counterions, the sensitivities were experimentally determined, and the detonation parameters were computed.

Lastly, Chapter 4 was focused on the crystal engineering of acentric polar crystals and dynamic crystals for applications in photonics and mechanically responsive materials. Also in this research field, crystal engineering plays a fundamental role because these materials are made up of organic conjugated molecules and held together by intermolecular interactions, like  $\pi$ - $\pi$  interactions and H-bonding. In this context, new NLO active materials were obtained. Moreover, an organic co-crystal of **Toluim** with N-methyl pyrrolidone shows SCSC transition with a snake-like motion. SCSC phases in which the switching of the structures is initiated by heat represents one of the most searched dynamic effects. Several recent studies have explored the exploitation of these phase changes, like **Tol\_NMP**, in organic crystals for application as actuators and sensors.



## Appendix A: Synthesis and Crystallization

### *Synthesis of NTD*

2,3-diaminonaphthalene (2.50 g, 13.7 mmol) and triethylamine (7.26 g) were dissolved in 50 mL of dichloromethane. The system, kept under nitrogen flux, was cooled at 0 °C and then a solution composed of thionyl chloride (4.08 g, 34.4 mmol) in 10 mL of dichloromethane was added dropwise. The reaction mixture was kept at 0 °C for 30 min and then was stirred at reflux for 3 h. After, the mixture was poured in 300 mL of hydrochloric acid 0.4 M and then extracted with dichloromethane and dried over sodium sulfate. The solvent was finally evaporated under reduced pressure. The crude product was treated with boiling heptane and the undissolved impurities were filtered off. The solvent was evaporated under reduced pressure and a bright orange-brown crystalline solid was obtained (yield 70 %). m.p. (dec.): 100 °C.

<sup>1</sup>H-NMR (400 MHz, DMSO-d<sub>6</sub>) δ 7.41 (q, 2H), 7.94 (q, 2H), 8.57 (s, 2H).

<sup>13</sup>C- NMR (100 MHz, DMSO-d<sub>6</sub>) δ 118.2, 126.5, 128.8, 134.2, 152.5.

The synthetic procedure is similar to the first synthetic report of NTD.<sup>59</sup>

### *Synthesis of NSeD*

2,3-diaminonaphthalene (1.00 g, 6.34 mmol) was dissolved in 250 mL of 0.1 M Hydrochloric Acid. Selenium dioxide (0.774 g, 10 % excess), dissolved in 100 mL of 0.1 M hydrochloric acid, was added. A bright red precipitate appeared almost immediately. After 10 minutes, the precipitate was separated by filtration, dried at room temperature and recrystallized from petroleum ether (40-60 °C) to afford large red needles. m.p. 275 °C (dec.).

<sup>1</sup>H-NMR (400 MHz, CDCl<sub>3</sub>) δ 7.31 (q, 2H), 7.81 (q, 2H), 8.41 (s, 2H).

<sup>13</sup>C- NMR (100 MHz, CDCl<sub>3</sub>) δ 119.6, 126.7, 129.1, 134.8, 158.9 .

The synthetic procedure closely follows that reported in the study of the luminescence of some piazselenols.

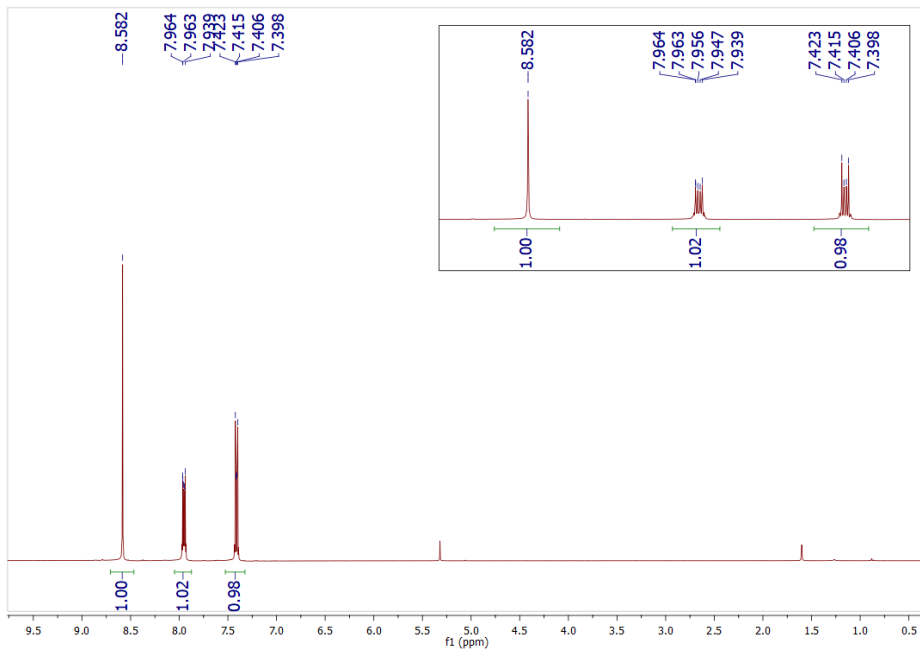


Figure 77  $^1\text{H-NMR}$  spectrum of NTD in  $\text{CD}_2\text{Cl}_2$ . The signal at 5.32 ppm is due to residual  $\text{CH}_2\text{Cl}_2$ , and the signal at 1.52 ppm is due to water.

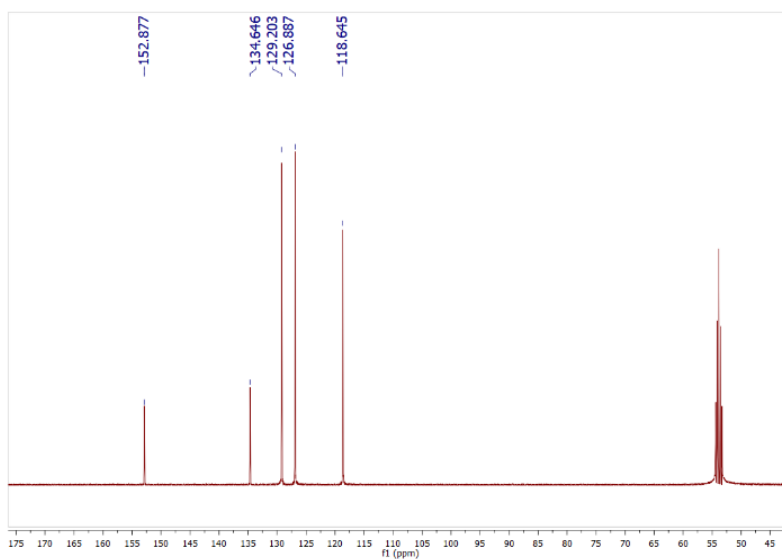


Figure 78  $^{13}\text{C}$ -NMR spectrum of **NTD** in  $\text{CD}_2\text{Cl}_2$ . The signal at 54 ppm is due to the solvent.

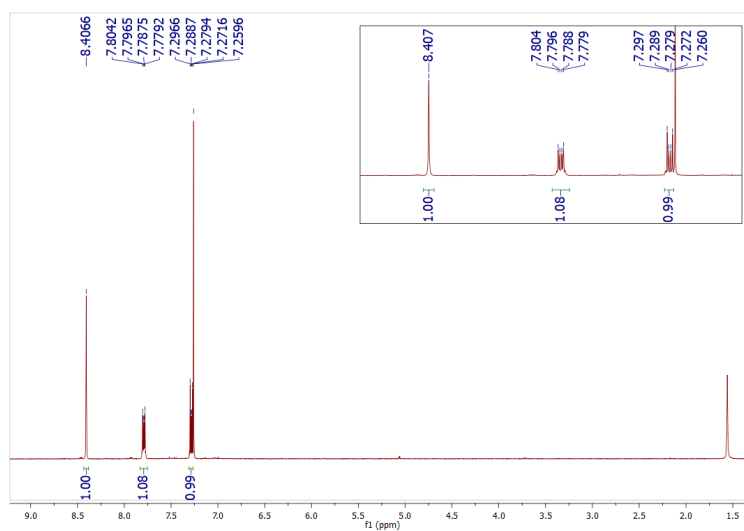


Figure 79  $^1\text{H}$ -NMR spectrum of **NSeD** in  $\text{CDCl}_3$ . The signal at 7.26 ppm is due to residual  $\text{CHCl}_3$ , and the signal at 1.55 ppm is due to water.

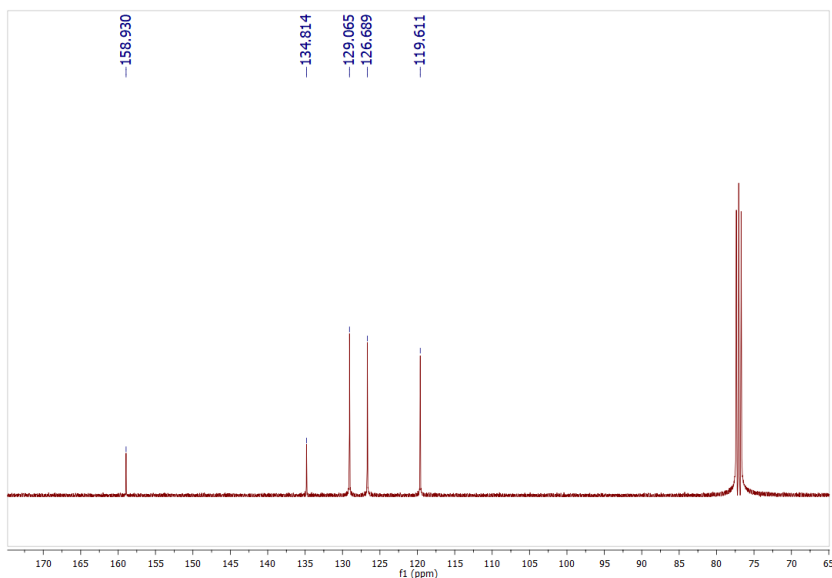


Figure 80.  $^{13}\text{C}$ -NMR spectrum of **NSeD** in  $\text{CDCl}_3$ . The signal at 77.2 ppm is due to the solvent.

### **Synthesis of bsd**

Synthesis of **bsd** was performed according to literature procedure<sup>149</sup>.

2.031 g of o-phenyldiamine (18.8 mmol) e 2.328 g of  $\text{SeO}_2$  (20.9 mmol, 10% excess) were dissolved in 20 ml of ethanol. The reaction was left under reflux for 20 minutes and then the solvent was removed under vacuo. The solid was recovered with water and filtered under vacuo giving 3.048 g of a pale pink solid (yield 89 %).  $T_f = 71\text{-}76\text{ }^\circ\text{C}$ .

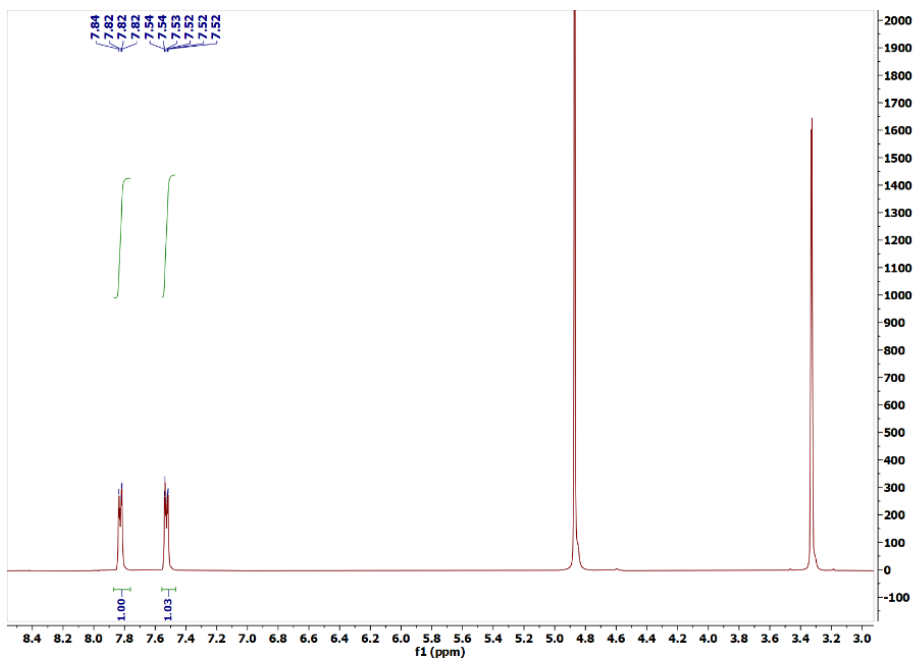


Figure 81.  $^1\text{H-NMR}$  spectrum of *bsd* in  $d_6\text{-DMSO}$ , at  $25\text{ }^\circ\text{C}$ . The signals at 2.51 ppm and at 3.35 ppm are due to the solvent and water respectively.

### Synthesis of TT9

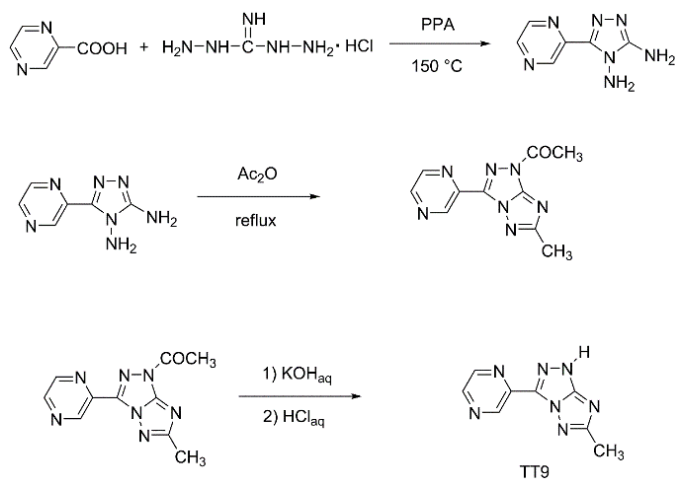


Chart 14 Synthetic Procedure for TT9 compound.

### **Synthesis of 5-(2-pyrazinyl)-3,4-diamino-1,2,4-triazole**

Commercial 2-pyrazinic acid (5.00 g,  $4.03 \times 10^{-2}$  mol) and diaminoguanidine monohydrochloride (6.58 g,  $5.24 \times 10^{-2}$  mol, 30% excess by mol) were finely ground in a mortar. The mixture was added in portions, under mechanical stirring, to a beaker containing polyphosphoric acid (PPA, 40 g) at 100 °C. After few minutes, evolution of gaseous HCl was observed from the reaction mixture. The temperature of the pasty reaction mixture was increased to 150 °C and the mixture reacted for 12 h, under stirring. Afterwards, the mixture was poured into cold water (100 ml) and the pH of the resulting solution was increased to 5 by addition of a concentrated solution of NaOH. A pale orange solid was obtained, filtered, washed with water, and dried in oven at 100 °C. Yield: 5.84 g (83%). M.p.: 277 °C.  $^1\text{H}$  NMR (400 MHz,  $d_6$ -DMSO)  $\delta$  5.94 (s, 2H), 6.00 (s, 2H), 8.62 (d, 1H), 8.67 (d, 1H), 9.17 (s, 1H).  $^{13}\text{C}$  NMR (100 MHz,  $d_6$ -DMSO)  $\delta$  143.2, 143.9, 144.0, 144.15, 145.2, 157.3.

### **Synthesis of 4-methyl-7-(pyrazin-2-yl)-2H-[1,2,4]triazolo[3,2-c][1,2,4]triazole (TT9)**

5-(2-pyrazinyl)-3,4-diamino-1,2,4-triazole (1.98 g,  $1.92 \times 10^{-2}$  mol) and acetic anhydride (40 mL) were placed in a round bottomed flask equipped with a condenser. The mixture was heated at reflux for 3 h under stirring. Afterwards, the brown solution was cooled to room temperature and poured into water (200 mL). The resultant solution was kept under gentle boiling till the volume reduced to 20 mL. Upon cooling to room temperature, a pale-yellow solid formed which was filtered and dried in oven at 100 °C. The solid was suspended in 120 mL of an aqueous solution of KOH (10% by weight) in a round bottomed flask equipped with a condenser and a magnetic stirrer. The mixture was refluxed under stirring and, after few minutes, a colourless solution was obtained. The solution was kept under reflux for 2 h. Afterwards, it was cooled to room temperature and poured into water (70 mL). The pH of the resulting solution was adjusted to 4 by dropwise

addition of 37 % HCl and a pale pink solid formed that was filtered, washed with water and dried in oven at 100 °C. Yield: 0.545 g (44 %). M.p.: 278 °C. <sup>1</sup>H NMR (400 MHz, d<sub>6</sub>-DMSO) δ 2.39 (s, 3H), 8.77 (d, 1H), 8.83 (d, 1H), 9.39 (s, 1H), 14.11(s, 1H). <sup>13</sup>C NMR (100 MHz, d<sub>6</sub>-DMSO) δ 15.4, 135.8, 141.3, 142.8, 145.3, 145.8, 157.8, 168.3. MS m/z: 202.1 [M<sup>+</sup>H]<sup>+</sup>.

#### **Synthesis and crystallization of the complex Cu<sub>2</sub>(TT9)<sub>2</sub>Cl<sub>4</sub>**

CuCl<sub>2</sub> dihydrate (13.0 mg, 7.63x10<sup>-5</sup> mol) was dissolved in 1 mL of ethanol and added to 3mL of a hot solution of TT9 (15.3 mg, 7.63x10<sup>-5</sup> mmol) in 50:50 Ethanol/water. One drop of HCl 37% was added. Prismatic greenish crystals of Cu<sub>2</sub>(C<sub>8</sub>H<sub>7</sub>N<sub>7</sub>)<sub>2</sub>Cl<sub>4</sub>· 5H<sub>2</sub>O were obtained by slow evaporation of the solvent at constant temperature (30° C) in 24 hours. Yield 45%. Anal. calc. C 25.24 %, H 3.18 %, N 25.76 %. Found C 25.09 %, H 3.03 %, N 25.69 %.

#### **Synthesis and crystallization of the complex Zn<sub>2</sub>(TT9)<sub>2</sub>(H<sub>2</sub>O)<sub>6</sub>(Zn<sub>2</sub>Br<sub>6</sub>)<sub>2</sub> dihydrate**

Colourless flat crystals of the complex were grown in two days by slow evaporation of a clear 50:50 water-ethanol solution containing equimolar amounts of ZnBr<sub>2</sub> (14 mg, 0.01 mmol) and TT9 (20 mg, 0.01 mmol), at room temperature with quantitative yield. Anal. calc. C 10.32 %, H 1.41 %, N 10.53 %. Found C 9.84 %, H 1.17 %, N 10.51 %.

#### **Synthesis and crystallization of the complex salt (TT9)ZnCl<sub>4</sub>**

TT9 (20 mg, 0.1 mmol) was dissolved in 1 ml of water. The solution was added to another solution containing ZnCl<sub>2</sub> (14 mg, 0.1 mmol), ethanol (1 mL) and 5 drops of concentrated HCl solution (37%). The solution was left undisturbed, and pale-yellow lozenge crystals of the salt were obtained in two days, with 75% yields. Anal. Calc. C 31.32 %, H 2.96 %, N 31.96 %. Found C 30.74 %, H 2.72 %, N 31.94 %.

### **Synthesis and crystallization of the complex salt (TT9)SnCl<sub>6</sub>·2H<sub>2</sub>O**

Brown prismatic crystals of (TT9)SnCl<sub>6</sub> dihydrate salt were grown in a week by slow evaporation of a clear 50:50 water-ethanol solution containing equimolar amounts of SnCl<sub>4</sub> (26 mg, 0.01 mmol) and TT9 (20 mg, 0.01 mmol) and 5 drops of HCl 37% solution at room temperature with quantitative yield. Anal. calc. C 24.83 %, H 2.87 %, N 25.34 %. Found C 24.71 %, H 2.84 %, N 25.31 %.

### **Synthesis and crystallization of the complex salt Cu(TT9)<sub>2</sub>Br<sub>2</sub>·3H<sub>2</sub>O**

Prismatic green crystals of the complex Cu(TT9)<sub>2</sub>Br<sub>2</sub>·3H<sub>2</sub>O were grown in two days by slow evaporation of a clear 50:50 (v/v) ethanol-water solution containing a 1:2 molar ratio of copper (II) bromide dihydrate (13.0 mg, 7.63x10<sup>-5</sup> mol) and TT9 (31.0 mg, 1.56x10<sup>-4</sup> mol) at RT in a quantitative yield (53.0 mg).

### **Synthesis and crystallization of the complex salt Zn(TT9)<sub>2</sub>Br<sub>2</sub>·H<sub>2</sub>O**

Prismatic brown crystals of the complex Zn(TT9)<sub>2</sub>Br<sub>2</sub>·H<sub>2</sub>O, were grown in a week by slow evaporation of a 50:50 (v/v) ethanol-water solution containing a 1:2 molar ratio of zinc (II) bromide (14.0 mg, 0.1 mmol) and TT9 (40.0 mg, 0.2 mmol) at RT in a 75% yield (48.0 mg).

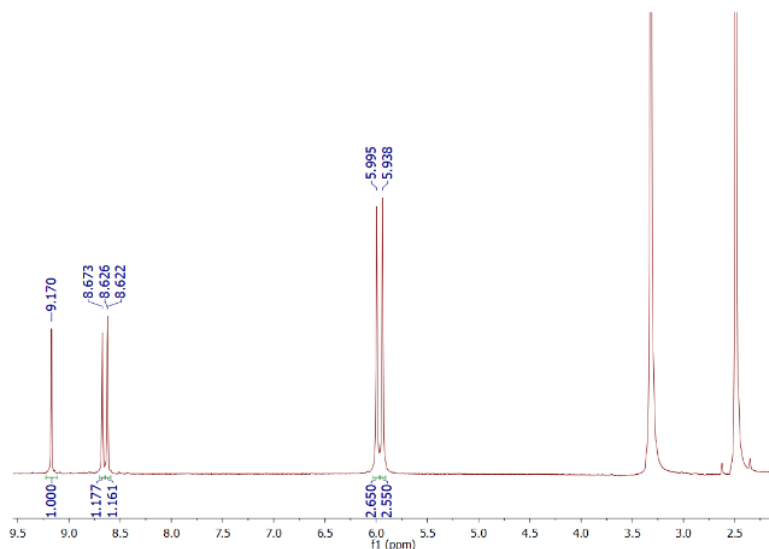


Figure 82.  $^1\text{H}$ -NMR spectrum of 5-(2-pyrazinyl)-3,4-diamino-1,2,4-triazole, in  $d_6$ -DMSO, at 25 °C. The signals at 2.51 ppm and at 3.35 ppm are due to the solvent and water respectively.

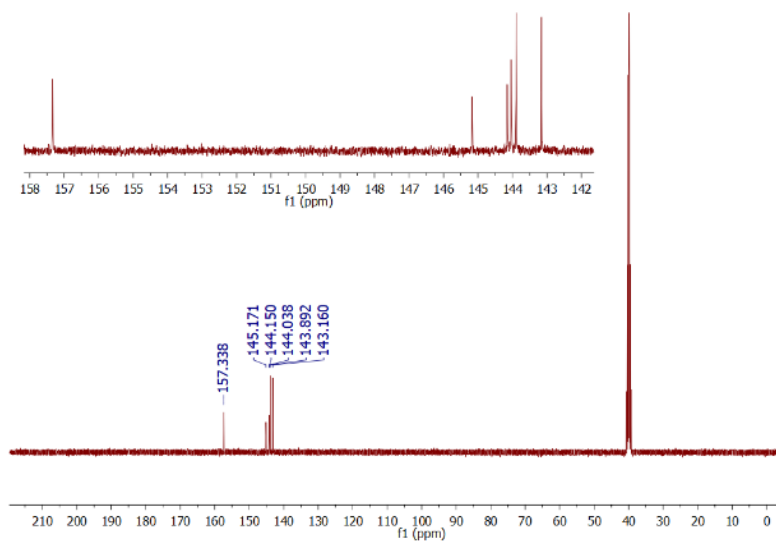


Figure 83.  $^{13}\text{C}$ -NMR spectrum of 5-(2-pyrazinyl)-3,4-diamino-1,2,4-triazole, in  $D_6$ -DMSO, at 25 °C. The signals nearly 40 ppm are due to the solvent.

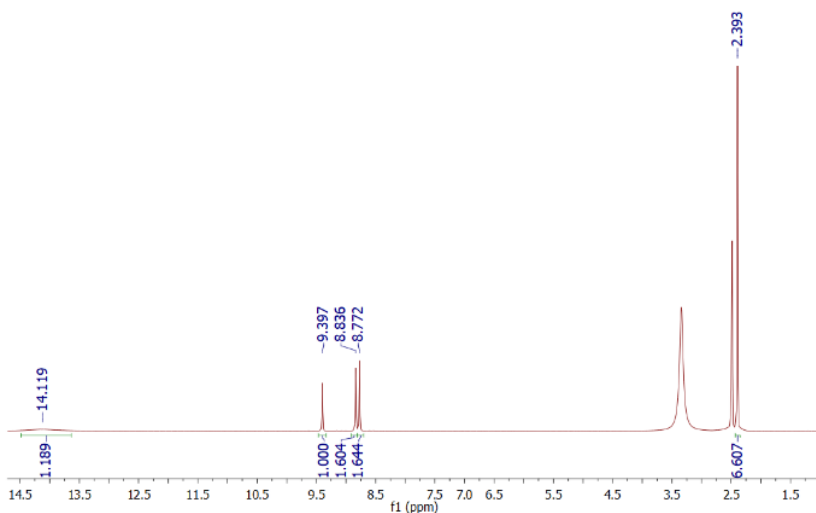


Figure 84.  $^1\text{H-NMR}$  spectrum of 4-methyl-7-(pyrazin-2-yl)-2H-[1,2,4]triazolo[3,2-c][1,2,4]triazole (TT9), in  $d_6\text{-DMSO}$ , at 25 °C. The signals at 2.51 ppm and at 3.35 ppm are due to the solvent and water respectively.

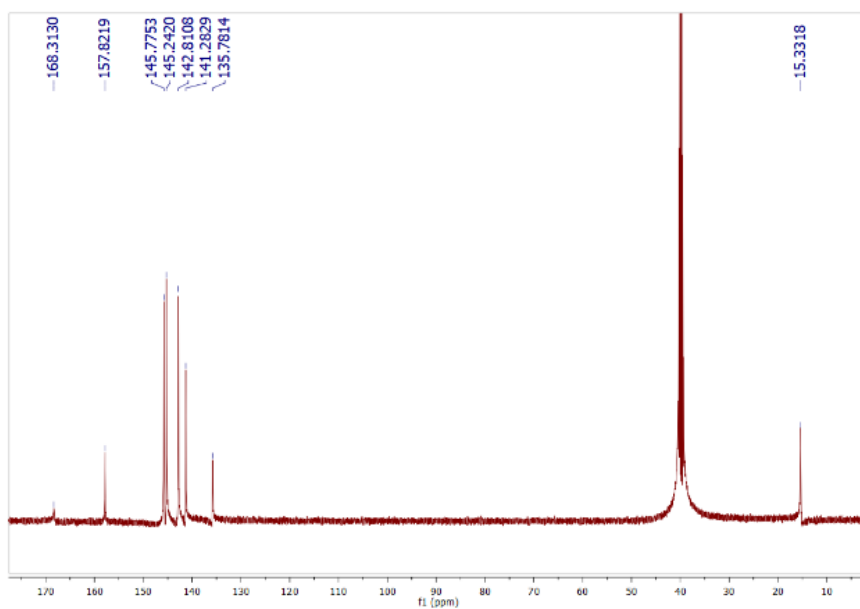


Figure 85.  $^{13}\text{C-NMR}$  spectrum of 4-methyl-7-(pyrazin-2-yl)-2H-[1,2,4]triazolo[3,2-c][1,2,4]triazole (TT9), in  $d_6\text{-DMSO}$ , at 25 °C. The signals nearly 40 ppm are due to the solvent.

## Synthesis of **bTT**

Commercial 5-Amino-1*H*-1,2,4-triazole-3-carboxylic acid (5.00 g,  $4.90 \times 10^{-2}$  mol) and diaminoguanidine monohydrochloride (6.40 g,  $5.09 \times 10^{-2}$  mol, 30% excess by mol) were finely ground in mortar. The mixture was added in portions, under mechanical stirring, to a beaker containing polyphosphoric acid (PPA, 40 g) at 100 °C. After few minutes, evolution of gaseous HCl was observed from the reaction mixture. The temperature of the pasty reaction mixture was increased to 150 °C and the mixture reacted for 5 h, under stirring. Afterwards, the mixture was poured into cold water (100 mL) and the pH of the resulting solution was increased to 5 by addition of concentrated solution of NaOH. Raw **bTT**, in the form of an off-white solid was obtained, filtered, washed with cold water and dried in oven at 100 °C. Raw **bTT** (5.5 g) was suspended in water (100 mL). Concentrated HCl 37 % (20 mL) was added drop by drop under stirring, and the suspension was heated. Upon addition of the acid and heating, the suspension progressively became a clear, pale brown solution. The solution was kept boiling under stirring, until the volume reduced to 50 mL. Then it was cooled to room temperature, and a white solid (the dichlorhydrate salt) formed. The solid was recovered by filtration and washed on the filter with ethanol. Then it was dried in oven at 110 °C. 4.9 g of dichlorhydrate salt were obtained. The salt product was solved in hot water (about 100 mL). A 1 M solution of KOH was added drop by drop until the pH was 6-7. A crystal-line precipitate formed. The suspension was cooled to room temperature and the precipitate was filtered, washed with water on the filter and dried in oven at 110 °C overnight. In this way, 3.98 g of pure **1** were obtained. Yield: 3.98 g (45 %). M.p. 347 °C (dec.). <sup>1</sup>H NMR (400 MHz, d<sub>6</sub>-DMSO) δ 5.67 (s, 2H), 5.77 (s, 2H), 6.18 (s, 2H) 12.33 (s, 1H). <sup>13</sup>C NMR (100 MHz, d<sub>6</sub>-DMSO) δ 142.59, 150.58 155.47 157.24. MS (ESI, +): m/z calcd. for C<sub>4</sub>H<sub>7</sub>N<sub>9</sub> 181.16; found 182.0 (M<sup>+</sup>·H).

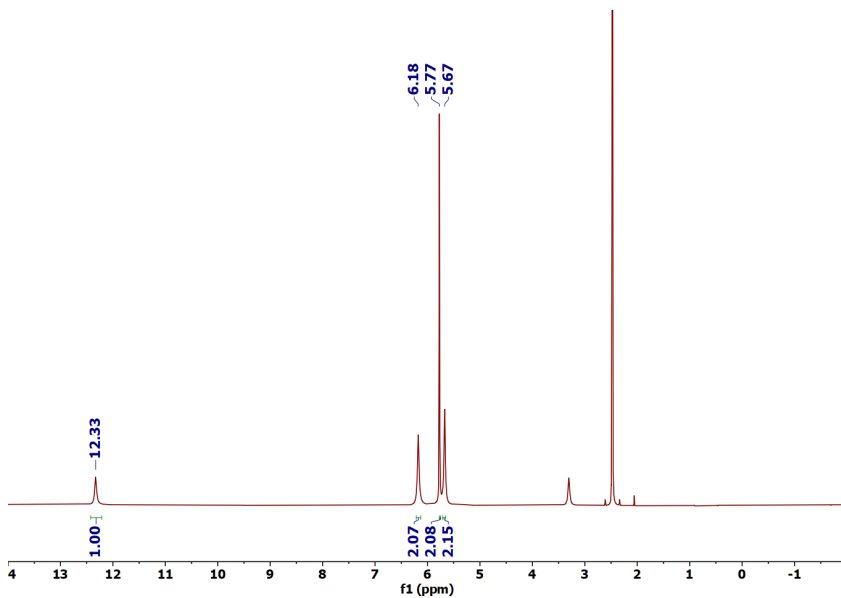


Figure 86.  $^1\text{H}$ -NMR spectrum of **bTT** in  $\text{DMSO-}d_6$  at  $25\text{ }^\circ\text{C}$ . The signals at 2.51 ppm and at 3.35 ppm are due to the solvent and water, respectively.

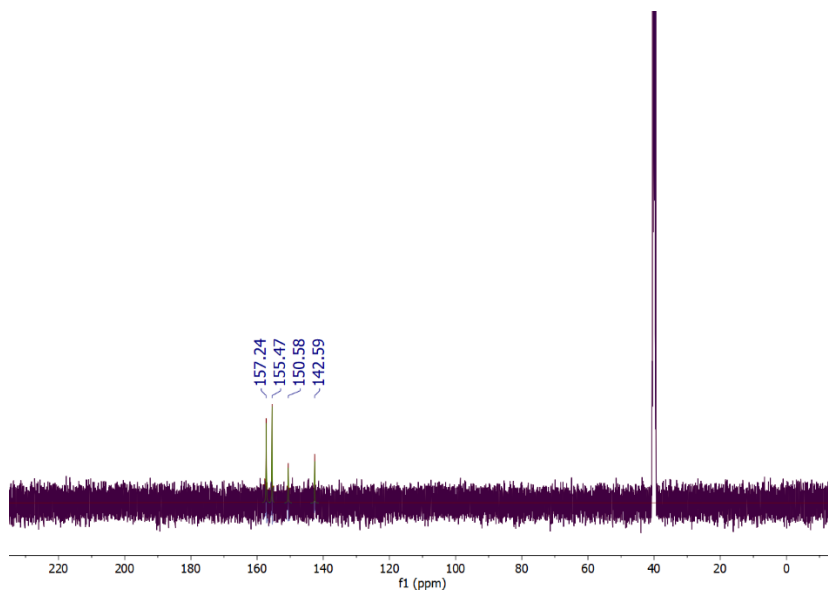


Figure 87.  $^{13}\text{C}$ -NMR spectrum of **bTT** in  $\text{DMSO-}d_6$ , at  $25\text{ }^\circ\text{C}$ . The signals nearly 40 ppm are due to the solvent.

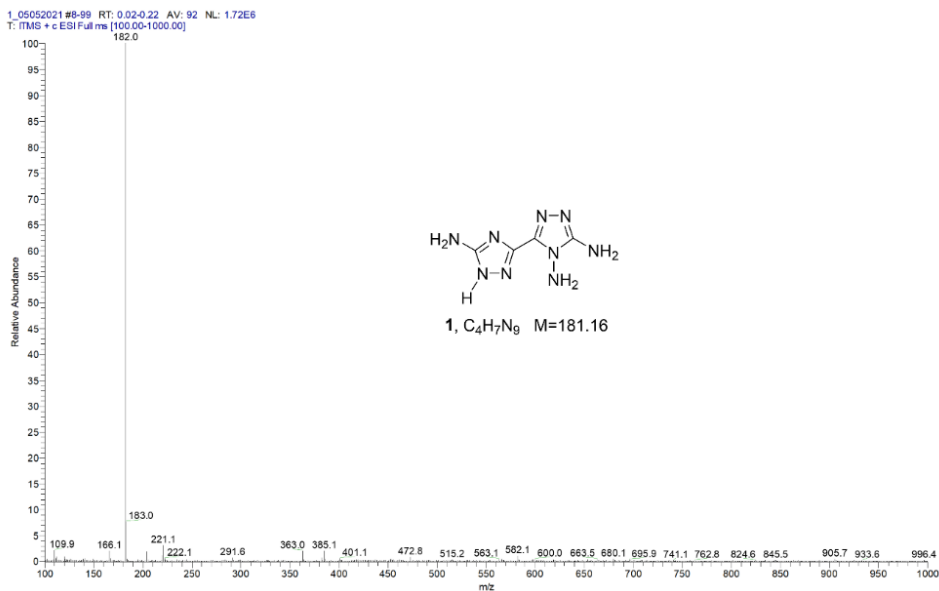


Figure 88. ESI mass spectrum of **bTT**.

### Crystallization of **bTT\_2**

**bTT\_4** (0.667 g, 1.75 mmol) was dissolved in 25 mL of hot water. The solution was added to another solution containing potassium dinitramide (KN<sub>3</sub>O<sub>4</sub>, 0.508 g, 3.50 mmol) and 2 mL of water. Pale-pink prismatic crystals of triamine monocation salt were obtained by slow cooling down to room temperature from a warm water bath (70° C) with quantitative yield.

### Crystallization of **bTT\_3**

10 drops of HBr conc. solution (48% v/v) were added to a hot water solution of 30 mg of **bTT** (0.150 mmol). Prismatic colourless crystals of dihydrate bromide salt were obtained by slow solvent evaporation at room temperature in 2 days, with 86 % yield.

### Crystallization of **bTT\_4**

5 drops of HClO<sub>4</sub> conc. solution (70% v/v) were added to a hot water solution of 30 mg of **bTT** (0.150 mmol). Prismatic colourless crystals of perchlorate salt

hydrate were obtained by slow evaporation at room temperature in 2 days, with 90% yield. The sample was dehydrated by keeping in a desiccator over  $\text{CaCl}_2$  for 1 week.

#### **Crystallization of bTT\_5**

5 drops of  $\text{HNO}_3$  conc. solution (65% v/v) were added to a hot water solution of 30 mg of **bTT** (0.150 mmol). Pale-pink lozenge crystals of nitrate salt dihydrate were obtained by slow cooling down to room temperature from warm water bath (70° C) with quantitative yield.

#### **Crystallization of bTT\_6**

5 drops of  $\text{H}_2\text{SO}_4$  con. Solution (98% v/v) were added to a hot water solution of 30 mg of **bTT** (0.150 mmol). Pale pink prismatic crystals of sulfate salt were obtained by slow cooling down to room temperature from warm water bath (70°C) with quantitative yield.

#### **Crystallization of bTT\_7**

**bTT** (30 mg, 0.150 mmol) was dissolved in 1 mL of hot water. The solution was added to another solution containing  $\text{ZnCl}_2$  (20 mg, 0.150 mmol), water (1 mL) and 10 drops of concentrated HCl solution (37% v/v). The solution was left undisturbed, and pale-brown prismatic crystals were obtained in two days, with 60% yield.

#### **Crystallization of bTT\_8**

Brown prismatic crystals of **bTT-8** dihydrate salt were grown in one day by slow cooling down to room temperature of a hot water solution containing 200 mg of **bTT** (1 mmol) and KOH concentrated solution (2 mL) with quantitative yield.

### Synthesis of 4-hydroxybenzohydrazide (HIB)

13.165 g of Hydrazine hydrate (0.263 mol) were added to 200 ml solution of methyl 4-(hydroxy) benzoate (10.015 g, 0.066mol). After 12 hours refluxing a white crystalline solid was obtained, filtered under vacuo, and washed with hexane to afford 10.864 g of 4-hydroxybenzohydrazide (yield 90.5%).  $^1\text{H}$  NMR (400 MHz, DMSO- $d_6$ )  $\delta$  4.39 (s, 2H), 6.77 (d, 2H), 7.68 (d, 2H), 9.48 (s, 1H), 9.91 (s 1H);

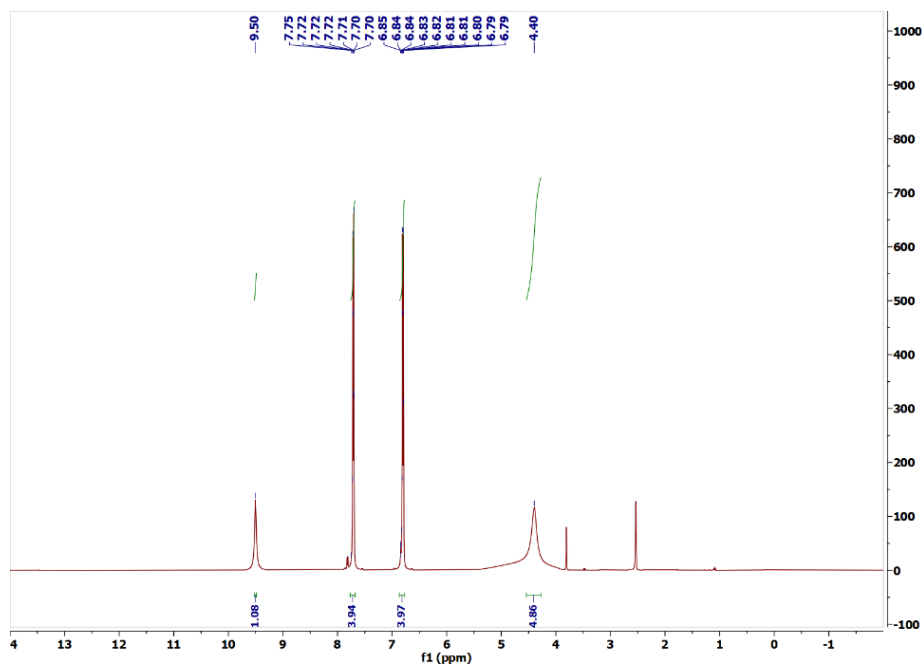


Figure 89.  $^1\text{H}$ -NMR spectrum of 4-hydroxybenzohydrazide in DMSO- $d_6$  at 25 °C. The signals at 2.51 ppm and at 3.75 ppm are due to the solvent and water, respectively.

### Synthesis of (E)-N'-benzylidene-4-hydroxybenzohydrazide (Benzim)

0.329g of benzaldehyde (3.10 mmol, 0.314 mL, 15% excess) were added to a suspension of 0.410 g of 4-hydroxybenzohydrazide (2.69 mmol) 40 mL of ethanol absolute. After refluxing for 1 hour, the solution was concentrated to 20 mL and cooled to RT. Colourless crystals were obtained, filtered under vacuo and washed

with cold ethanol afforded to 0.450 g of **Benzim** (yield 70%).  $^1\text{H}$  NMR (400 MHz, DMSO- $d_6$ )  $\delta$  11.69 (s, 1H), 8.39 (s, 1H), 7.78 (m, 5H), 7.44 (t, 3H) 6.86( d, 2H).

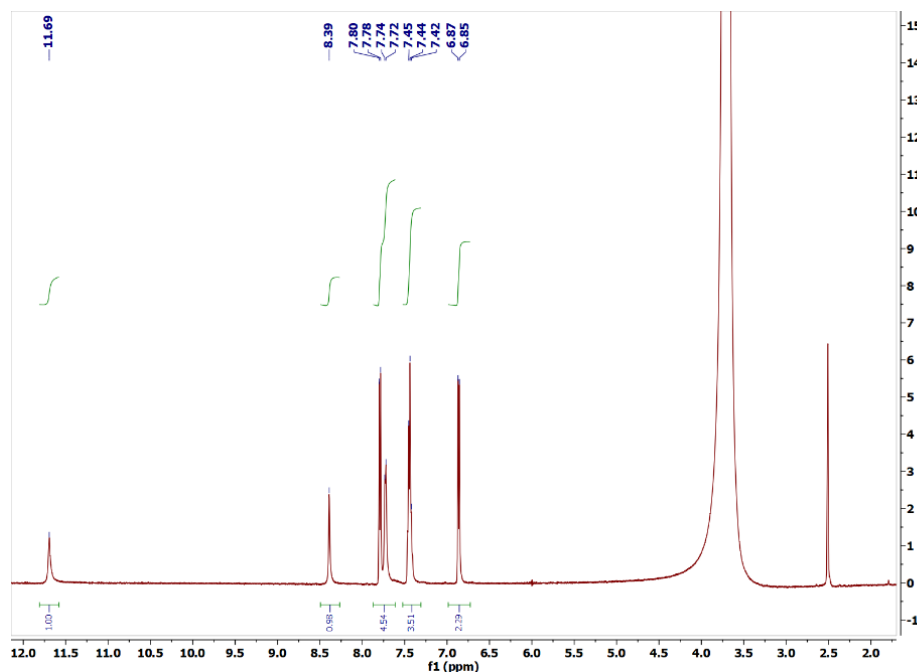


Figure 90.  $^1\text{H}$ -NMR spectrum of **Benzim** in DMSO- $d_6$  at 25 °C. The signals at 2.51 ppm and at 3.75 ppm are due to the solvent and water, respectively.

### Synthesis of (E)-4-hydroxy-N'-(4-methylbenzylidene)benzohydrazide (Toluim)

1 g of 4-methylbenzaldehyde (8.3 mmol, 1.02 mL, 15% excess) were added to a suspension of 1.08 g of 4-hydroxybenzohydrazide (7.1 mmol) 65 mL of ethanol absolute. After refluxing for 1 hour, the solution was concentrated to 30 mL and cooled to RT. Colourless crystals were obtained, filtered under vacuo and washed with cold ethanol afforded to 1.209 g of **Toluim** (yield 66%).  $^1\text{H}$  NMR (400 MHz, DMSO- $d_6$ )  $\delta$  11.58 (s, 1H), 10.11 (s, 1H), 8.40 (s, 1H), 7.81 (d, 2H), 7.60 (d, 2H), 7.25 (d, 2H), 6.87 (d, 2H).

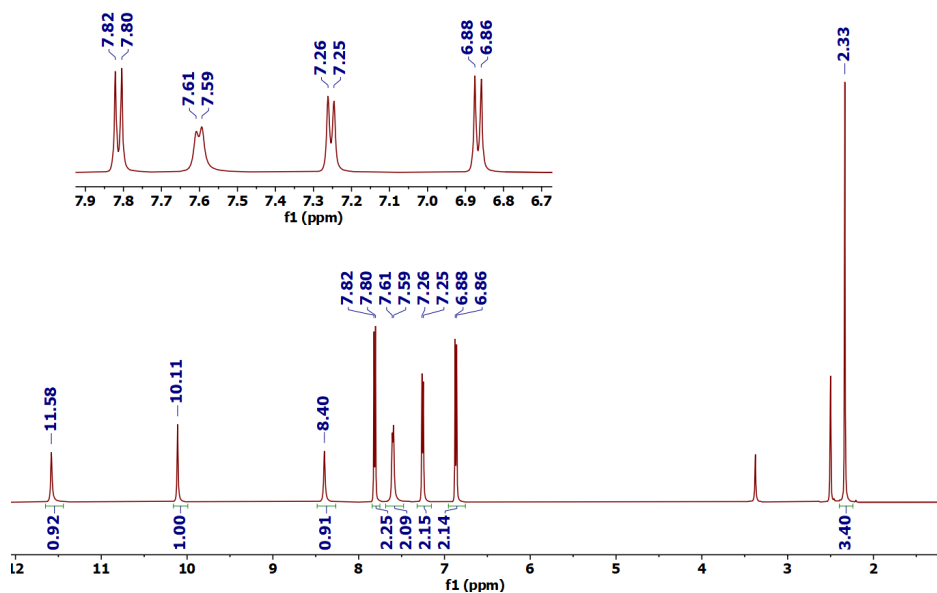


Figure 91.  $^1\text{H-NMR}$  spectrum of **Toluim** in  $\text{DMSO-}d_6$  at  $25\text{ }^\circ\text{C}$ . The signals at  $2.51\text{ ppm}$  and at  $3.35\text{ ppm}$  are due to the solvent and water, respectively.

### Synthesis of (E)-N'-(4-Fluorobenzylidene)-4-hydroxybenzohydrazide (Fluorim)

0.702 g of 4-fluorobenzaldehyde (5.66 mmol, 0.585 mL, 15% excess) were added to a suspension of 0.836 g of 4-hydroxybenzohydrazide (5.40 mmol) 50 mL of ethanol absolute. After refluxing for 1 hour, the solution was concentrated to 25 mL and cooled to RT. Colourless crystals were obtained, filtered under vacuo and washed with cold ethanol afforded to 1.35 g of **Fluorim** (yield 95%).  $^1\text{H NMR}$  (400 MHz,  $\text{DMSO-}d_6$ )  $\delta$  11.58 (s, 1H), 10.11 (s, 1H), 8.40 (s, 1H), 7.81 (d, 2H), 7.60 (d, 2H), 7.25 (d, 2H), 6.87 (d, 2H).

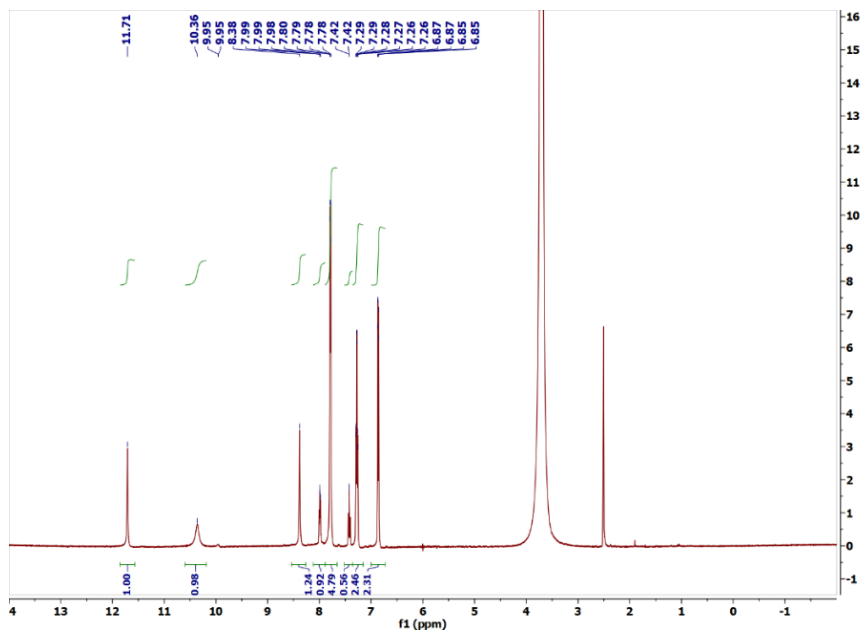


Figure 92.  $^1\text{H}$ -NMR spectrum of **Fluorim** in  $\text{DMSO-}d_6$  at  $25\text{ }^\circ\text{C}$ . The signals at 2.51 ppm and at 3.35 ppm are due to the solvent and water, respectively.

### Synthesis of (E)-N'-(4-Fluorobenzylidene)-4-hydroxybenzohydrazide (Metoxim)

0.500 g of p-anisaldehyde (3.67 mmol, 0.450 mL, 15% excess) were added to a suspension of 0.473 g of 4-hydroxybenzohydrazide (3.11 mmol) 50 mL of ethanol absolute. After refluxing for 1 hour, the solution was concentrated to 25 mL and cooled to RT. Colourless crystals were obtained, filtered under vacuo and washed with cold ethanol afforded to 0.395 g of **Metoxim** (yield 55%).  $^1\text{H}$  NMR (400 MHz,  $\text{DMSO-}d_6$ )  $\delta$  11.56 (s, 1H), 8.33 (s, 1H), 8.40 (s, 1H), 7.77 (d, 2H), 7.67 (d, 2H), 7.02 (d, 2H), 6.84 (d, 2H), 3.79 (t, 3H partially covered by solvent).

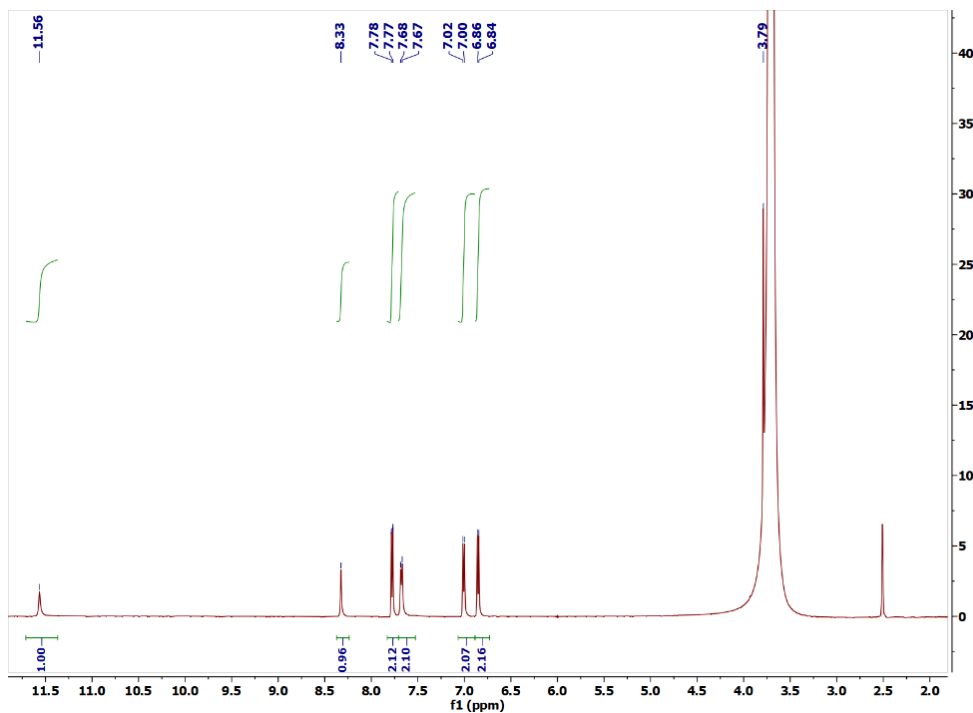


Figure 93.  $^1\text{H-NMR}$  spectrum of **Metoxim** in  $\text{DMSO-d}_6$  at  $25\text{ }^\circ\text{C}$ . The signals at  $2.51\text{ ppm}$  and at  $3.35\text{ ppm}$  are due to the solvent and water, respectively.

### Synthesis of (E)-N'-(4-chlorobenzylidene)-4-hydroxybenzohydrazide (Chlorim)

1 g of 4-chlorobenzaldehyde (7.1 mmol, 1.2 mL, 15% excess) were added to a suspension of 0.912 g of 4-hydroxybenzohydrazide (6 mmol) 50 mL of ethanol absolute. After refluxing for 1 hour, the solution was concentrated to 25 mL and cooled to RT. Colourless crystals were obtained, filtered under vacuo and washed with cold ethanol afforded to 0.892 g of **Chlorim** (yield 55%).  $^1\text{H NMR}$  (400 MHz,  $\text{DMSO-d}_6$ )  $\delta$  11.71 (s, 1H), 10.15 (s, 1H), 8.42 (s, 1H), 7.82 (d, 2H), 7.80 (d, 2H), 7.51 (d, 2H), 6.87 (d, 2H).

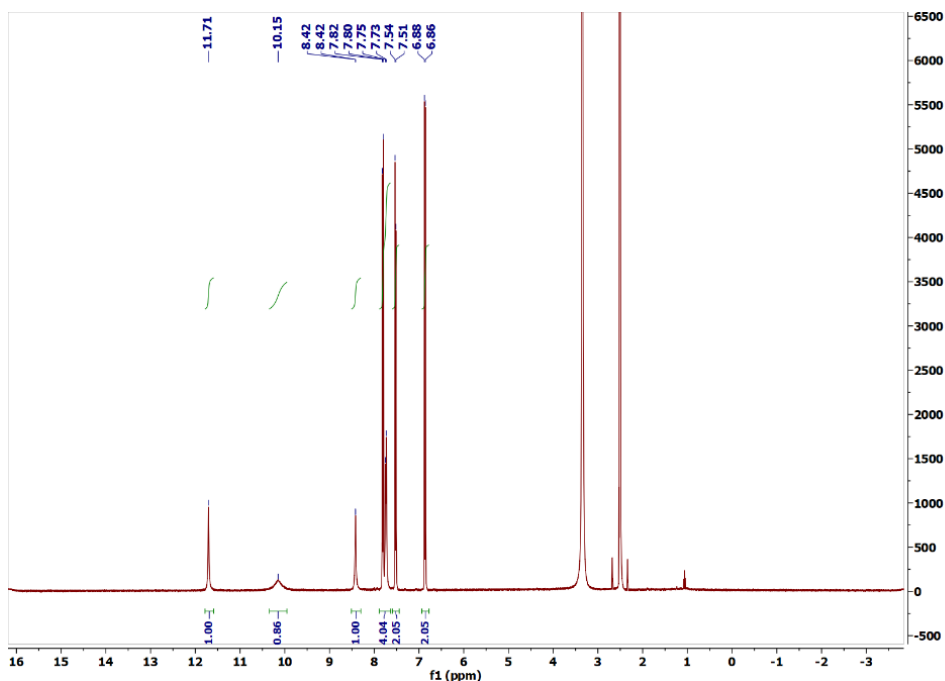


Figure 94.  $^1\text{H-NMR}$  spectrum of **Chlorim** in  $\text{DMSO-}d_6$  at  $25\text{ }^\circ\text{C}$ . The signals at  $2.51\text{ ppm}$  and at  $3.35\text{ ppm}$  are due to the solvent and water, respectively.

### Crystallization of Tol\_NMP1

Large prismatic colourless crystals of solvate polymorph I were obtained by heating a 20 wt. % suspension of **Toluim** in NMP on a hot plate until dissolution occurred, then the solution was placed in an oven at  $60\text{ }^\circ\text{C}$  and cooled to RT at  $5^\circ\text{C/h}$ . The crystals were obtained with quantitative yields.

### Crystallization of Tol\_NMP2

Solvate polymorph II was obtained from I after a SCSC transition. The forms were unequivocally characterized by X-ray diffraction.

### Crystallization of Tol\_NMP3

Large prismatic colourless crystals of solvate polymorph I were obtained by heating a 33 wt. % suspension of **Toluim** in NMP on a hot plate until dissolution occurred, then the solution was placed in an oven at  $100^\circ\text{C}$  and cooled to RT at  $2^\circ\text{C/h}$ . The crystals were obtained with quantitative yields.

## Appendix B: Materials and Methods

### Computational analysis

The calculations performed on **TT9**, **bTT** and related compounds were carried out by using the Gaussian 09 package.<sup>150</sup> The BMK functional in conjunction with the 6-31+G\*\* basis set was used throughout.<sup>151,152</sup> The relative stability of the phases has been checked using a triple- $\zeta$  basis set.<sup>153</sup> That potential was chosen after an extensive benchmark of computational methodologies for similar systems. Effects due to polarization of the solvent were included by the polarizable continuum model (PCM);<sup>154</sup> the nature of all stationary points (both in vacuum and in the solution phase) was verified by computing the eigenvalues of the Hessian matrix. Both for the neutral and the protonated forms, populations of tautomers have been obtained by Boltzmann statistics at 298 K with DFT predicted energies. That approach requires a rapid establishment of equilibrium between tautomers, which is indeed the case, because it has been shown that tautomeric equilibria for a closely related triazolo-triazole are established on a  $\sim 10$  ps timescale.<sup>155</sup>

## DFT-Calculations on crystal phases

Periodic 3D ab initio calculations were performed adopting Density Functional Theory (DFT) method using the CRYSTAL17 suite of program.<sup>55</sup> Linear Combination of Atomic Orbital (LCAO) expanded in Gaussian Basis set approach were used. An unrestricted spin polarization configuration was considered for all systems in antiferromagnetic arrangement ( $\uparrow\downarrow$ ). Hybrid B3LYP<sup>156,157</sup> functionals and the empirical Grimme D3 correction<sup>158</sup> were employed to obtain a correct evaluation of the exchange and dispersion interactions, which are very important in this kind of molecular crystal. All-electron Ahlrichs triple zeta plus polarization basis set of Gaussian-type functions, centred on the nuclei, have been adopted for C, N, O, H, S, Se, Cl and Br atoms<sup>159,160</sup>. The self-consistent-field (SCF) convergence threshold of the energy was set to  $10^{-10}$  Hartree for structural optimizations and  $10^{-11}$  for vibration frequency calculations. The convergence parameter of the root means square (RMS) of the gradient and the displacement were enforced from the default values of 0.0003 a.u. and 0.0012 a.u. to 0.0001 a.u. and 0.0004 a.u., respectively, to increase the accuracy of geometry optimizations of the final structures. The truncations of exchange and Coulomb infinite lattice series can be set by five tolerance parameters  $T_i$  (see Crystal 17 manual), which were set to 8 ( $T_1 - T_3$ ), 12 ( $T_4$ ) and 50 ( $T_5$ ), for a correct evaluation of the exchange interactions. The irreducible part of the Brillouin zone was sampled adopting a  $\Gamma$ -point-centred Pack-Monkhorst grid consisting of 36 k-points. These mesh grids correspond to a shrinking factor value (IS, see Crystal 17 manual) of 4. The DFT exchange-correlation contribution to the Fock matrix was calculated by numerical integration over the unit cell volume. Angular and radial points for the integration grid are produced through Lebedev 2D angular point distributions and Gauss-Legendre radial quadrature. The default pruned grid XLGRID were increased to a very dense XXLGRID with 991454 total points (99 radial and 1454 angular points).

### **Thermal measurement**

Differential scanning calorimetric (DSC) and thermogravimetric (TGA) analysis were performed using a Perkin-Elmer Pyris instrument, under flowing nitrogen or air, at 10 K/min scanning rate.

### **Optical analysis**

Temperature controlled optical microscopy was performed with a Zeiss Axioskop polarizing microscope equipped with a Mettler FP90 heating stage. The microscope was also equipped with support for recording movies and photographs through a Huawei P30 smartphone device.

### **X-Ray analysis**

All data for crystal structure determinations were measured on a Bruker-Nonius KappaCCD diffractometer equipped with Oxford Cryostream 700 apparatus, using graphite monochromated MoK $\alpha$  radiation (0.71073 Å). Data were collected at room temperature and at -100 °C. Reduction of data and semiempirical absorption correction were done using SADABS program.<sup>161</sup> The structures were solved by direct methods (SIR97 program<sup>162</sup>) and refined by the full-matrix least-squares method on  $F^2$  using SHELXL-2016 program<sup>163</sup> with the aid of the program WinGX.<sup>164</sup> H atoms bonded to C were generated stereochemically and refined by the riding model, those bonded to O and N where found in difference Fourier maps, and their coordinates were refined. To all H atoms,  $U_{iso}$  equal to 1.2 times  $U_{eq}$  of the carrier atom was given. The analysis of the crystal packing was performed using the program Mercury.<sup>165</sup>

### **Magnetic Measurements**

Magnetic susceptibility measurements were performed with an Oxford VSM Maglab 9T device under perpendicular magnetic field of 0.05T

### **NMR analysis**

NMR spectra were recorded with Bruker and Varian spectrometers operating at 400 MHz and 500 MHz respectively.

## Acid-base and complexation analysis

The compound stock solutions were prepared starting from the solid. Deionized and doubly distilled water was used to prepare all aqueous solutions. NaCl (Fluka, dried overnight at 120 °C) was used to prepare the ionic medium solutions. Stock solutions of HCl (Carlo Erba p.a.) were standardized against  $\text{KHCO}_3$  using methyl red as indicator, with a reproducibility of 0.1 %. NaOH (Baker p.a.) stock solutions were standardized against standardized HCl solutions. The protolytic equilibria were studied by UV-vis absorption spectroscopy in 0.5 M NaCl, 4% ethanol (v/v), as the ionic medium. following a procedure already described below. The experiments were performed as acid-base titrations at constant total concentration. The investigated pH range extends from 0.3 to 12. For each experimental point, the equilibrium free proton concentration was evaluated from the measured electromotive force at the ends of the galvanic cell GE/TS/RE, where TS indicates the test solution, GE is the glass electrode, and RE is a reference electrode (0.5 M NaCl|Hg<sub>2</sub>Cl<sub>2</sub>|Hg(Pt)) placed outside but electrically connected to TS through a salt bridge. The Nernst potential of the cell, E(mV), can be written as  $E = E_0 + 59.16 \log [\text{H}^+] + E_j$  where  $E_j$  = liquid junction potential due to the replacement of  $\text{Na}^+$  with  $\text{H}^+$ . The evaluation of the constant of the glass electrode,  $E_0$ , was performed in the first stage of each experiment by a coulometric titration, using the Gran method.<sup>166</sup> The test solutions at  $0.3 < \text{pH} < 2$  were obtained analytically. All the experiments were carried out in air in a thermostat, at  $25.00 \pm 0.03$  °C. Potentiometric experimental data were collected by means of an automatic data acquisition system based on Hewlett-Packard (HP) instrumentation. The glass membrane electrodes reversible to protons were supplied by Metrohm. Highly precise ( $\pm 0.02$  mV) emf measurements were made by adapting the impedance of the glass electrode through operational amplifiers. Coulombmetric variations of the solution composition were carried out using a Hewlett Packard “DC Power Supply”. The intensity of the current in the

electrolysis circuit was measured from the potential drop at the ends of a calibrated resistance; the current density was set at about 1 mA/cm<sup>2</sup>.

The conditional equilibrium constants  $K_{a1}$  and  $K_{a2}$  of **TT9**, determined by the UV–vis absorbance analysis as a function of the pH. From the Lambert-Beer law, assuming additivity of the absorbances, it is:

$$A^\lambda = b \left( \sum_i \varepsilon_i^\lambda c_i \right) = b (\varepsilon_1^\lambda [H_2L^+] + \varepsilon_2^\lambda [HL] + \varepsilon_3^\lambda [L^-]) \quad (1)$$

in which  $b$  is the optical path of the cell (1 cm) and  $\varepsilon_i^\lambda$  is the molar extinction coefficient of the species  $i$  at the given wavelength. The analytical concentration of TT9 ( $HL$ ),  $C$ , is given by:

$$C = [H_2L^+] + [HL] + [L^-] \quad (2)$$

The acid-base equilibrium constants are

$$K_{a1} = \frac{[HL] \cdot [H_3O^+]}{[H_2L^+]}, K_{a2} = \frac{[L^-] \cdot [H_3O^+]}{[HL]} \quad (3)$$

From these, it is possible to express the concentration of each species but one (e. g. the neutral one), as a function of the equilibrium constants and the concentration of  $H_3O^+$ :

$$[H_2L^+] = \frac{[HL] \cdot [H_3O^+]}{K_{a1}}, [L^-] = \frac{[HL] \cdot K_{a2}}{[H_3O^+]} \quad (4)$$

Putting (4) in (2) it is

$$C = \frac{[HL] \cdot [H_3O^+]}{K_{a1}} + [HL] + \frac{[HL] \cdot K_{a2}}{[H_3O^+]} \quad (5)$$

So, it is

$$[HL] = \frac{CK_{a1}[H_3O^+]}{[H_3O^+]^2 + K_{a1}[H_3O^+] + K_{a1}K_{a2}} \quad (6)$$

Putting (4) and (6) in (1) yields

$$A = b \cdot \left( \varepsilon_1^\lambda \frac{[HL] \cdot [H_3O^+]}{K_{a1}} + \varepsilon_2^\lambda [HL] + \varepsilon_3^\lambda \frac{[HL] \cdot K_{a2}}{[H_3O^+]} \right) \quad (7)$$

$$A = b \cdot [HL] \left( \varepsilon_1^\lambda \frac{[H_3O^+]}{K_{a1}} + \varepsilon_2^\lambda + \varepsilon_3^\lambda \frac{K_{a2}}{[H_3O^+]} \right) \quad (8)$$

$$A = b \cdot \frac{CK_{a1}[H_3O^+]}{[H_3O^+]^2 + K_{a1}[H_3O^+] + K_{a1}K_{a2}} \left( \varepsilon_1^\lambda \frac{[H_3O^+]}{K_{a1}} + \varepsilon_2^\lambda + \varepsilon_3^\lambda \frac{K_{a2}}{[H_3O^+]} \right) \quad (9)$$

$$A = b \cdot \frac{C}{[H_3O^+]^2 + K_{a1}[H_3O^+] + K_{a1}K_{a2}} (\varepsilon_1^\lambda [H_3O^+]^2 + \varepsilon_2^\lambda K_{a1}[H_3O^+] + \varepsilon_3^\lambda K_{a1}K_{a2}) \quad (10)$$

and, finally, the Bouger-Lambert-Beer equation

$$A = b \cdot \frac{C}{10^{-2pH} + 10^{-pH-pK_{a1}} + 10^{-pK_{a1}-pK_{a2}}} (\varepsilon_1^\lambda 10^{-2pH} + \varepsilon_2^\lambda 10^{-pH-pK_{a1}} + \varepsilon_3^\lambda 10^{-pK_{a1}-pK_{a2}})$$

The UV-Vis spectra were performed using a **TT9** constant concentration of  $3.0 \cdot 10^{-5}$  M. Formation of complexes of **TT9** with  $\text{Cu}^{2+}$  and  $\text{Zn}^{2+}$  was investigated by UV-vis spectrophotometry, as well. The experiments were performed as acid-base titrations of **TT9**-Cu(II) or **TT9**-Zn(II) solutions, keeping constant the total concentration of the triazole ( $c=3.0 \cdot 10^{-5}$  M) and of the metal, at various metal/ligand concentration ratios (1/1, 1/2, 1/4). The pH range investigated was  $3 < \text{pH} < 7$  for **TT9**-Cu(II) and  $1 < \text{pH} < 10$  for **TT9**-Zn(II). The upper limit of pH is imposed by precipitation of sparingly soluble metal hydroxides. Absorption spectra were recorded with a Varian Cary 50 UV-vis spectrophotometer using 1 cm cell. The primary spectrophotometric data (A, pH,  $\lambda$ ) were elaborated graphically<sup>167</sup> and numerically by using the HYPSPPEC 2008 program<sup>168</sup> for the determination of equilibrium constants in solution.

For **bTT**, the acid-base properties were studied in the same condition of temperature and ionic medium. The experiments were performed as acid-base

titrations at constant total concentration of **bTT** ( $C = 5.01 \cdot 10^{-5}$  M). The investigated pH spans between 0.7 and 10.

### Sensitivity testing

The impact sensitivity tests were carried out according to STANAG 4489<sup>169</sup> modified instruction<sup>170</sup> using a BAM (Bundesanstalt für Materialforschung) drophammer<sup>171</sup>. The friction sensitivity tests were carried out according to STANAG 4487<sup>172</sup> modified instruction<sup>173</sup> using the BAM friction tester. The classification of the tested compounds results from the “UN Recommendations on the Transport of Dangerous Goods”.<sup>174</sup> Additionally all compounds were tested upon the sensitivity towards electrical discharge using the Electric Spark Tester ESD 2010 EN.<sup>175</sup>

In order to be able to calculate the detonation parameters of **bTT** and of the corresponding salts, the enthalpy ( $H$ ) was calculated quantum chemically with the CBS-4M method.<sup>153</sup> The CBS method begins with a HF/3–21G(d) calculation to optimize the structure and for the calculations of the zero-point energy. Then, using a larger basis set, the so-called base-energy is calculated. A MP2/6–31+G calculation with a CBS extrapolation gives the perturbation-theory correct energy, which takes the electron correlation into account. A MP4(SDQ)/6–31+(d,p) calculation is used, to estimate the correlation contributions of a higher order. The most widely used CBS-4M version today is a re-parametrization of the original CBS-4 version, which contains additional empirical correction terms (M stands for “minimal population localization” here).

The enthalpies of the gaseous species M can then be calculated using the method of the atomization energies:<sup>176–178</sup>

$$\Delta H_f^0(g, M) = H_M^0 - \sum H_{atoms}^0 + \sum \Delta H_f^0(atoms)$$

The calculated enthalpies (H) for neutral **bTT** and the corresponding ions as well as the relevant atoms H, C, N, O and Cl using the CBS-4M method, are summarized in Table 18.

Therefore, in Table 18 we already have the  $H_{(molecules)}^o$  and  $H_{(atom)}^o$  values (given in a. u. = atomic units; 1 a. u. = 1 H = 627.089 kcal mol<sup>-1</sup>). The values for  $H_f^o$  (atoms) are easily obtained from the literature and are summarized in Table 19.

Table 18. CBS-4M values

	Symmetry	NIMAG	$-H^{298}$ / a. u.
1H-C <sub>4</sub> H <sub>7</sub> N <sub>9</sub>	C <sub>s</sub>	0	648.458350
[C <sub>4</sub> H <sub>8</sub> N <sub>9</sub> ] <sup>+</sup>	C <sub>s</sub>	0	648.839050
[C <sub>4</sub> H <sub>9</sub> N <sub>9</sub> ] <sup>2+</sup>	C <sub>s</sub>	0	649.075205
N(NO <sub>2</sub> ) <sub>2</sub> <sup>-</sup>	C <sub>2</sub>	0	464.499541
ClO <sub>4</sub> <sup>-</sup>	T <sub>d</sub>	0	760.171204
NO <sub>3</sub> <sup>-</sup>	D <sub>3h</sub>	0	280.080429
H			0.500991
C			37.786156
N			54.522462
O			74.991202
Cl			459.674555

Table 19. Literature values for  $H_f^o$  (atoms) (in kcal mol<sup>-1</sup>).

	NIST <sup>179</sup>
C	
H	52.1
C	171.3
N	113.0
O	59.6
Cl	29.0

According to the equation given above, we can now easily calculate the standard enthalpies of formation  $H_f^o$  (g) for the gas phase (Table 20).

Table 20. Calculated standard enthalpies of formation  $\Delta H_f^\circ$  (g) for the gas-phase.

gas-phase species	formula	$\Delta H_f^\circ$ (g)/ kcal mol <sup>-1</sup>	$\Delta H_f^\circ$ (g) / kJ mol <sup>-1</sup>
<b>bTT</b>	C <sub>4</sub> H <sub>7</sub> N <sub>9</sub>	120.0	502.2
<b>bTT</b> <sup>+</sup>	[C <sub>4</sub> H <sub>8</sub> N <sub>9</sub> ] <sup>+</sup>	247.6	1035.8
<b>bTT</b> <sup>2+</sup>	[C <sub>4</sub> H <sub>9</sub> N <sub>9</sub> ] <sup>2+</sup>	465.7	1948.6
Dinitramide anion	[N(NO <sub>2</sub> ) <sub>2</sub> ] <sup>-</sup>	-29.2	-122.2
Perchlorate anion	[ClO <sub>4</sub> ] <sup>-</sup>	-66.1	-276.6
Nitrate anion	[NO <sub>3</sub> ] <sup>-</sup>	-74.6	-312.3

To be able to convert the standard enthalpies of formation  $\Delta H_f^\circ$  (g) for the gas-phase into values for the condensed phase, for covalent molecules (NG) we additionally require the enthalpy of sublimation  $\Delta H_{\text{sub}}$ . (for solids) or the enthalpy of vaporization  $\Delta H_{\text{vap}}$ . (for liquids). Both values can be estimated using the Trouton's rule, in which  $T_m$  is the melting point of the solid and  $T_b$  is the boiling point of the liquid:<sup>180</sup>

$$\Delta H_{\text{sub}}. [\text{J mol}^{-1}] = 188 T_m [\text{K}]$$

$$\Delta H_{\text{vap}}. [\text{J mol}^{-1}] = 90 T_b [\text{K}]$$

**bTT** is a solid and has a m.p. of 351 °C (= 624 K). Therefore, the enthalpy of sublimation is calculated to be  $\Delta H_{\text{sub}}(\mathbf{bTT}) = 117 \text{ kJ mol}^{-1}$  (28.0 kcal mol<sup>-1</sup>).

In the case of ionic solids of the type AB, AB<sub>2</sub> or A<sub>2</sub>B, the lattice energy ( $\Delta U_L$ ) and lattice enthalpy ( $\Delta H_L$ ) can be calculated by using the Jenkin's method.<sup>181-183</sup> Only the molecular volumes of the ions are required. These can be most easily obtained from single crystal X-ray diffraction data:

$$\Delta U_L = |z_+||z_-|v \left[ \frac{a}{\sqrt[3]{V_M}} + \beta \right]$$

Here  $|z^+|$  and  $|z^-|$  are the dimensionless charges of the cations and anions and  $v$  is the number of ions per ‘molecule’ (2 for  $[\mathbf{bTT}^+][\text{N}_3\text{O}_4]$ , 3 for  $[\mathbf{bTT}^{2+}][\text{ClO}_4]_2$  and  $[\mathbf{bTT}^{2+}][\text{NO}_3]_2$ .  $V_M$  is the volume in  $\text{nm}^3$  of a formula unit (e.g. for all anhydrous:  $V_M([\mathbf{bTT}][\text{N}_3\text{O}_4]) = 0.256 \text{ nm}^3$ ,  $V_M([\mathbf{bTT}^{2+}][\text{ClO}_4]_2) = 0.324 \text{ nm}^3$ ,  $V_M([\mathbf{bTT}^{2+}][\text{NO}_3]_2) = 0.280 \text{ nm}^3$ ). The constants  $\alpha$  and  $\beta$  are dependent on the composition of the salt and are summarized in Table 21.

Table 21 The values for the constants  $\alpha$  and  $\beta$  for calculating the lattice energy by using the Jenkin’s method.

salt type	$\alpha / \text{kJ mol}^{-1}$	$\beta / \text{kJ mol}^{-1}$
AB	117.3	51.9
AB <sub>2</sub>	133.5	60.9
A <sub>2</sub> B	165.3	-29.8

The lattice energy  $\Delta U_L$  can easily be converted into the corresponding lattice enthalpy  $\Delta H_L$ :

$$\Delta H_L(A_p B_q) = \Delta U_L + \left[ p \left( \frac{n_A}{2} - 2 \right) + q \left( \frac{n_B}{2} - 2 \right) \right] RT$$

$n_A$ ,  $n_B = 3$  for monoatomic ions, 5 for linear polyatomic ions, 6 for non-linear, polyatomic ions. Therefore, the following values for the lattice energies and enthalpies can be written for the anhydrous salts:

Table 22 Lattice energies and enthalpies.

Salt	Salt name from Chart 10	$\Delta U_L / \text{kJ mol}^{-1}$	$\Delta H_L / \text{kJ mol}^{-1}$
$[\mathbf{bTT}^+][\text{N}_3\text{O}_4]$	<b>bTT-2</b>	473.3	478.3
$[\mathbf{bTT}^{2+}][\text{ClO}_4]_2$	<b>bTT-4</b>	1531.6	1539.0
$[\mathbf{bTT}^{2+}][\text{NO}_3]_2$	<b>bTT-5</b>	1589.8	1597.2

The final solid-state enthalpies of formation  $\Delta H_f^0$  for all compounds analyzed are summarized in Table 23:

Table 23 Enthalpies of formation of **bTT** compounds.

compound	formula	$\Delta H_f^0 / \text{kJ mol}^{-1}$	$\rho / \text{g cm}^{-3}$
<b>bTT</b>	$\text{C}_4\text{H}_7\text{N}_9$	+385.2	1.629
<b>[bTT<sup>+</sup>][N<sub>3</sub>O<sub>4</sub>]</b>	$\text{C}_4\text{H}_8\text{N}_{12}\text{O}_4$	+435.3	1.837
<b>[bTT<sup>2+</sup>][ClO<sub>4</sub>]<sub>2</sub></b>	$\text{C}_4\text{H}_9\text{N}_9\text{O}_8\text{Cl}_2$	-143.6	1.908
<b>[bTT<sup>2+</sup>][NO<sub>3</sub>]<sub>2</sub></b>	$\text{C}_4\text{H}_9\text{N}_{11}\text{O}_6$	-273.2	1.773

### SHG setup

The intensity of the second-harmonic (SH) wave is independent on the polarization direction of the fundamental wavelength in SHG from randomly-oriented powders – as in the case studied here – because the detected intensity results from a uniform average on all possible SH polarizations. Hence, a fixed configuration for the polarization direction of both fundamental and SH waves was used for all the investigated samples. The SHG measurements were performed in reflection mode, with the fundamental wave at wavelength 1064 nm provided by a 25 ps duration Nd:YAG laser impinging at an angle of incidence of 45° on the sample surface, placed horizontally. Suitable optical filters were used to block the fundamental beam diffused by the sample and the residual SH signal generated by various optical elements composing the experimental setup. The horizontally-polarized (S wave) component of the SH wave generated by a horizontally-polarized fundamental beam was detected through a photomultiplier tube coupled to the exit slit of a monochromator tuned at the SH wavelength (532 nm), used to abate the noise caused by spurious (non-SHG) signals at different

wavelengths. The laser spot size on the sample surface was about 1 mm. Each SH intensity reading was obtained by averaging the SHG signal over 400 laser shots. For each sample, it was verified that the measured intensity was independent on the polarization direction chosen for signal detection, as expected for the case of powdered samples.

- Number of averaged waveforms: 400 waveforms.
- Cursor parameters (gating):  $\Delta = 30\text{ns}$ ,  $@ = 49.6\text{ ns}$
- Scales:  $\Delta t = 10\text{ ns}$ ,  $\Delta y = 100\text{ mV}$
- Zero signal on Min: +2 mV. The signal used was the minimum of the PMT waveform (more linear than the Area).

## Appendix C: Crystallographic Data

**NTD phase I:**  $C_{10}H_6N_2S$ ,  $M_r=186.23$ , monoclinic,  $P2_1/c$ ,  $Z=8$ , orange,  $a=12.066(4)$  Å,  $b=6.997(3)$  Å,  $c=20.105(7)$  Å,  $\beta=98.87(2)^\circ$ ,  $V=1677.1(11)$  Å<sup>3</sup>,  $T=173$  K, 16864 refl.ns collected, 3809 unique ( $R_{int}=0.0366$ ),  $R=0.0440$  ( $I>2\sigma(I)$ ),  $wR(all)=0.1161$ ,  $GOF=1.063$ , final max./min. peak 0.320/-0.270 e/Å<sup>3</sup>. CCDC 1957518.

**NTD phase II:**  $C_{10}H_6N_2S$ ,  $M_r=186.23$ , monoclinic,  $P2_1/c$ ,  $Z=4$ , orange,  $a=9.997(4)$  Å,  $b=12.192(5)$  Å,  $c=7.167(3)$  Å,  $\beta=109.56(2)^\circ$ ,  $V=823.1(6)$  Å<sup>3</sup>,  $T=173$  K, 4716 refl.ns collected, 1867 unique ( $R_{int}=0.0380$ ),  $R=0.0402$  ( $I>2\sigma(I)$ ),  $wR(all)=0.1194$ ,  $GOF=1.013$ , final max./min. peak 0.248/-0.338 e/Å<sup>3</sup>. CCDC 1957520.

**NTD phase III:**  $C_{10}H_6N_2S$ ,  $M_r=186.23$ , monoclinic,  $P2_1/c$ ,  $Z=4$ , orange,  $a=3.833(2)$  Å,  $b=16.419(5)$  Å,  $c=13.410(5)$  Å,  $\beta=104.25(2)^\circ$ ,  $V=818.0(6)$  Å<sup>3</sup>,  $T=173$  K, 5712 refl.ns collected, 1844 unique ( $R_{int}=0.0330$ ),  $R=0.0353$  ( $I>2\sigma(I)$ ),  $wR(all)=0.1122$ ,  $GOF=1.047$ , final max./min. peak 0.350/-0.247 e/Å<sup>3</sup>. CCDC 1957522.

**NSeD:**  $C_{10}H_6N_2Se$ ,  $M_r=233.13$ , monoclinic,  $P2_1/c$ ,  $Z=4$ , dark orange,  $a=6.353(3)$  Å,  $b=4.222(2)$  Å,  $c=32.268(6)$  Å,  $\beta=100.690(10)^\circ$ ,  $V=850.5(6)$  Å<sup>3</sup>,  $T=173$  K, 6658 refl.ns collected, 1926 unique ( $R_{int}=0.0364$ ),  $R=0.0305$  ( $I>2\sigma(I)$ ),  $wR(all)=0.0764$ ,  $GOF=1.084$ , final max./min. peak 0.391/-0.828 e/Å<sup>3</sup>. CCDC 1957524.

**NTD\_bfly:**  $C_{20}H_{12}N_4S_2$ ,  $M_r=372.46$ , orthorhombic,  $Pna2_1$ ,  $Z=4$ , colorless,  $a=16.0130(12)$  Å,  $b=7.3440(13)$  Å,  $c=13.5770(16)$  Å,  $V=1596.6(4)$  Å<sup>3</sup>,  $T=173$  K, 13132 refl.ns collected, 3280 unique ( $R_{int}=0.0350$ ),  $R=0.0355$  ( $I>2\sigma(I)$ ),  $wR(all)=0.0917$ ,  $GOF=1.051$ , final max./min. peak 0.553/-0.256 e/Å<sup>3</sup>. CCDC 1957526

**btd-1:**  $C_6H_4Cl_2CuN_2S$ ,  $M_r=270.63$ , monoclinic,  $P2_1/m$   $Z=2$ , yellow plate,  $a=3.713(3)$  Å  $b=12.553(6)$  Å  $c=8.767(4)$  Å,  $\beta=97.73(2)^\circ$ ,  $V=404.9$  Å<sup>3</sup>,  $T=298(2)$  K, 2981 reflcns collected, 884 unique ( $R_{int}=0.060$ ),  $R=0.0603$  ( $I > 2\sigma(I)$ ),  $R_w(\text{all})=0.0860$   $GOF=1.161$ , final max/min peak  $1.97/-0.65$  e/Å<sup>3</sup>. CCDC not submitted yet

**btd-2:**  $C_6H_4Br_2CuN_2S$ ,  $M_r=359.53$ , monoclinic,  $P2_1/m$   $Z=2$ , red plate,  $a=3.897(3)$  Å,  $b=12.568(6)$  Å,  $c=9.030(4)$  Å,  $\beta=97.33(2)^\circ$ ,  $V=438.7(4)$  Å<sup>3</sup>,  $T=293(2)$  K, 2612 reflcns collected, 1026 unique ( $R_{int}=0.039$ ),  $R=0.0563$  ( $I > 2\sigma(I)$ ),  $R_w(\text{all})=0.1582$   $GOF=1.257$ , final max/min peak  $2.18/-1.23$  e/Å<sup>3</sup>. CCDC not submitted yet

**bsed-1:**  $C_6H_4Cl_2CuN_2Se$   $M_r=317.51$  monoclinic,  $P2_1/m$   $Z=2$ , green plate,  $a=3.6770(15)$  Å,  $b=12.682(3)$  Å,  $c=8.707(2)$  Å,  $\beta=98.51(2)^\circ$ ,  $V=401.6(2)$  Å<sup>3</sup>,  $T=293(2)$  K, 3141 reflcns collected, 758 unique ( $R_{int}=0.089$ ),  $R=0.057$  ( $I > 2\sigma(I)$ ),  $R_w(\text{all})=0.087$   $GOF=1.052$ , final max/min peak  $2.630/-0.82$  e/Å<sup>3</sup>. CCDC not submitted yet

**bsed-2:**  $C_{12}H_8Br_2CuN_4Se_2$   $M_r=366.15$  triclinic,  $P\bar{1}$   $Z=4$ , dark brown lozenge,  $a=8.4870(10)$  Å,  $b=9.5870(12)$  Å,  $c=10.3190(8)$  Å,  $\alpha=94.514(10)^\circ$ ,  $\beta=109.679(9)^\circ$ ,  $\gamma=102.793(11)^\circ$ ,  $V=760.13(41)$  Å<sup>3</sup>,  $T=293(2)$  K, 9198 reflcns collected, 3438 unique ( $R_{int}=0.0520$ ),  $R=0.073$  ( $I > 2\sigma(I)$ ),  $R_w(\text{all})=0.153$   $GOF=1.135$ , final max/min peak  $1.924/-1.184$  e/Å<sup>3</sup>. CCDC not submitted yet

**TT9 hydrate:** (C<sub>8</sub>H<sub>7</sub>N<sub>7</sub>)·H<sub>2</sub>O, M = 219.22, Triclinic, a = 5.4070(13), b = 8.507(3), c = 11.507(5) Å, α=109.32(3)°, β=93.16(3)°, γ=96.25(3)°, V = 494.2(3) Å<sup>3</sup>, T = 293 K, space group *P* $\bar{1}$ , Z = 2, 5361 reflections measured, 2218 unique (R<sub>int</sub> = 0.051), which were used in all calculations. Final indices (on *F*<sup>2</sup>) were R=0.049 (I>2σ(I)), wR= 0.138 (all data), GOF=1.05. Final Δρ<sub>max</sub>, Δρ<sub>min</sub> was 0.22 and -0.24 e/ Å<sup>3</sup>. CCDC: 2016572

**TT9 hydrochloride:** (C<sub>8</sub>H<sub>8</sub>N<sub>7</sub>)Cl, M = 237.66, Monoclinic, a = 5.290(2), b = 16.438(4), c = 12.291(4) Å, β=107.96(2)°, V = 1016.7(6) Å<sup>3</sup>, T = 293 K, space group *P*2<sub>1</sub>/*c*, Z = 4, 10090 reflections measured, 2313 unique (R<sub>int</sub> = 0.074), which were used in all calculations. Final indices (on *F*<sup>2</sup>) were R=0.049 (I>2σ(I)), wR= 0.102 (all data), GOF=1.02. Final Δρ<sub>max</sub>, Δρ<sub>min</sub> was 0.26 and -0.32 e/ Å<sup>3</sup>. CCDC: 2016577

**TT9-dication tetrachlorozincate:** (C<sub>8</sub>H<sub>9</sub>N<sub>7</sub>)ZnCl<sub>4</sub>, M = 410.39, Orthorhombic, a = 8.7870(17), b = 16.250(4), c = 41.341(7) Å, V = 5903(2) Å<sup>3</sup>, T = 293 K, space group *Pnma*, Z = 16, 48632 reflections measured, 6987 unique (R<sub>int</sub> = 0.0645), which were used in all calculations. Final indices (on *F*<sup>2</sup>) were R=0.069 (I>2σ(I)), wR= 0.1768 (all data), GOF=1.167. Final Δρ<sub>max</sub>, Δρ<sub>min</sub> was 1.13 and -1.04 e/ Å<sup>3</sup>. CCDC: 2016573

**TT9-dication hexachlorostannate dihydrate:** (C<sub>8</sub>H<sub>9</sub>N<sub>7</sub>)SnCl<sub>6</sub>·2H<sub>2</sub>O, M = 570.64, Orthorhombic, a = 12.1370(19), b = 15.2500(11), c = 10.851(3) Å, V = 2008.4(6) Å<sup>3</sup>, T = 173 K, space group *Pna*2<sub>1</sub>, Z = 4, 8930 reflections measured, 4002 unique (R<sub>int</sub> = 0.0291), which were used in all calculations. Final indices (on *F*<sup>2</sup>) were R=0.0231 (I>2σ(I)), wR= 0.055 (all data), GOF=1.088. Final Δρ<sub>max</sub>, Δρ<sub>min</sub> was 0.410 and -0.605 e/ Å<sup>3</sup>. CCDC: 2016576

**Sodium triazolate trihydrate:**  $\text{Na}(\text{C}_8\text{H}_6\text{N}_7) \cdot 3\text{H}_2\text{O}$ ,  $M = 277.4$ , Triclinic,  $a = 6.8520(9)$ ,  $b = 9.1940(17)$ ,  $c = 10.1550(16)$  Å,  $\alpha = 72.687(18)^\circ$ ,  $\beta = 81.788(18)^\circ$ ,  $\gamma = 86.177(14)^\circ$ ,  $V = 604.29(18)$  Å<sup>3</sup>,  $T = 293$  K, space group  $P\bar{1}$ ,  $Z = 2$ , 7679 reflections measured, 2748 unique ( $R_{\text{int}} = 0.031$ ), which were used in all calculations. Final indices (on  $F^2$ ) were  $R = 0.038$  ( $I > 2\sigma(I)$ ),  $wR = 0.100$  (all data),  $\text{GOF} = 1.06$ . Final  $\Delta\rho_{\text{max}}$ ,  $\Delta\rho_{\text{min}}$  was 0.24 and -0.20 e/Å<sup>3</sup>. CCDC: 2016575

**Cu(TT9)Cl<sub>2</sub> hydrate:**  $\text{Cu}_2(\text{C}_8\text{H}_7\text{N}_7)_2\text{Cl}_4 \cdot 5\text{H}_2\text{O}$ ,  $M = 761.38$ , Triclinic,  $a = 10.745(2)$ ,  $b = 11.371(3)$ ,  $c = 12.811(2)$  Å,  $\alpha = 71.003(12)^\circ$ ,  $\beta = 76.242(15)^\circ$ ,  $\gamma = 73.412(16)^\circ$ ,  $V = 1400.2(5)$  Å<sup>3</sup>,  $T = 293$  K, space group  $P\bar{1}$ ,  $Z = 4$ , 18414 reflections measured, 6353 unique ( $R_{\text{int}} = 0.0511$ ), which were used in all calculations. Final indices (on  $F^2$ ) were  $R = 0.0405$  ( $I > 2\sigma(I)$ ),  $wR = 0.0978$  (all data),  $\text{GOF} = 1.003$ . Final  $\Delta\rho_{\text{max}}$ ,  $\Delta\rho_{\text{min}}$  was 0.465 and -0.454 e/Å<sup>3</sup>. CCDC: 2016578

**Zn<sub>2</sub>(TT9)<sub>2</sub>(H<sub>2</sub>O)<sub>6</sub>(Zn<sub>2</sub>Br<sub>6</sub>)<sub>2</sub> dihydrate:**  $\text{Zn}_2(\text{C}_8\text{H}_7\text{N}_7)_2(\text{H}_2\text{O})_6(\text{Zn}_2\text{Br}_6)_2 \cdot 2\text{H}_2\text{O}$ ,  $M = 761.38$ , Triclinic,  $a = 9.282(3)$ ,  $b = 10.500(9)$ ,  $c = 13.206(12)$  Å,  $\alpha = 107.35(7)^\circ$ ,  $\beta = 90.60(6)^\circ$ ,  $\gamma = 101.75(4)^\circ$ ,  $V = 1199.3(16)$  Å<sup>3</sup>,  $T = 173$  K, space group  $P\bar{1}$ ,  $Z = 1$ , 15578 reflections measured, 5460 unique ( $R_{\text{int}} = 0.1149$ ), which were used in all calculations. Final indices (on  $F^2$ ) were  $R = 0.0603$  ( $I > 2\sigma(I)$ ),  $wR = 0.1316$  (all data),  $\text{GOF} = 1.019$ . Final  $\Delta\rho_{\text{max}}$ ,  $\Delta\rho_{\text{min}}$  was 1.205 and -1.179 e/Å<sup>3</sup>. CCDC: 2016574

**bTT 0.5 (H<sub>2</sub>O):**  $\text{C}_4\text{H}_7\text{N}_9 \cdot 0.5(\text{H}_2\text{O})$ ,  $M = 190.19$ , Triclinic,  $a = 7.1560(7)$ ,  $b = 11.6750(16)$ ,  $c = 19.209(3)$  Å,  $\alpha = 85.50(2)^\circ$ ,  $\beta = 85.093(14)^\circ$ ,  $\gamma = 76.354(11)^\circ$ ,  $V$

= 1551.0(4) Å<sup>3</sup>, T = 173 K, space group  $P\bar{1}$ , Z = 8, 22895 reflections measured, 7082 unique, ( $R_{\text{int}} = 0.045$ ), which were used in all calculations. Final indices (on  $F^2$ ) were  $R = 0.046$  ( $I > 2\sigma(I)$ ),  $wR = 0.123$  (all data),  $\text{GOF} = 1.05$ . Final  $\Delta\rho_{\text{max}}$ ,  $\Delta\rho_{\text{min}}$  was 0.64 and -0.3 e/ Å<sup>3</sup>. CCDC: 2092331

**bTT\_2:** C<sub>4</sub>H<sub>8</sub>N<sub>9</sub>(N<sub>3</sub>O<sub>4</sub>), M = 288.22, Triclinic, a = 7.722(2), b = 8.773(2), c = 9.442(4) Å,  $\alpha = 64.422(15)^\circ$ ,  $\beta = 66.67(2)^\circ$ ,  $\gamma = 71.33(3)^\circ$ , V = 521.1(3) Å<sup>3</sup>, T = 173 K, space group  $P\bar{1}$ , Z = 2, 6676 reflections measured, 2386 unique, ( $R_{\text{int}} = 0.078$ ), which were used in all calculations. Final indices (on  $F^2$ ) were  $R = 0.059$  ( $I > 2\sigma(I)$ ),  $wR = 0.162$  (all data),  $\text{GOF} = 1.04$ . Final  $\Delta\rho_{\text{max}}$ ,  $\Delta\rho_{\text{min}}$  was 0.34 and -0.32 e/ Å<sup>3</sup>. CCDC: 2092333

**bTT\_3:** (C<sub>4</sub>H<sub>9</sub>N<sub>9</sub>)Br<sub>2</sub>·2H<sub>2</sub>O, M = 379.05, Triclinic, a = 6.5350(15), b = 7.0520(19), c = 14.486(6) Å,  $\alpha = 96.67(4)^\circ$ ,  $\beta = 100.35(3)^\circ$ ,  $\gamma = 106.565(16)^\circ$ , V = 619.5(4) Å<sup>3</sup>, T = 173 K, space group  $P\bar{1}$ , Z = 2, 8954 reflections measured, 2789 unique, ( $R_{\text{int}} = 0.035$ ), which were used in all calculations. Final indices (on  $F^2$ ) were  $R = 0.026$  ( $I > 2\sigma(I)$ ),  $wR = 0.062$  (all data),  $\text{GOF} = 1.10$ . Final  $\Delta\rho_{\text{max}}$ ,  $\Delta\rho_{\text{min}}$  was 0.45 and -0.64 e/ Å<sup>3</sup>. CCDC: 2092335

**bTT\_4:** (C<sub>4</sub>H<sub>9</sub>N<sub>9</sub>)(ClO<sub>4</sub>)<sub>2</sub>·H<sub>2</sub>O, M = 400.12, Triclinic, a = 5.2730(8), b = 7.239(3), c = 9.730(3) Å,  $\alpha = 100.17(3)^\circ$ ,  $\beta = 95.68(2)^\circ$ ,  $\gamma = 105.38(3)^\circ$ , V = 348.29(18) Å<sup>3</sup>, T = 173 K, space group  $P1$ , Z = 1, 4548 reflections measured, 2585 unique, ( $R_{\text{int}} = 0.026$ ), which were used in all calculations. Final indices (on  $F^2$ ) were  $R = 0.025$  ( $I > 2\sigma(I)$ ),  $wR = 0.067$  (all data),  $\text{GOF} = 1.06$ . Final  $\Delta\rho_{\text{max}}$ ,  $\Delta\rho_{\text{min}}$  was 0.22 and -0.41 e/ Å<sup>3</sup>. CCDC: 2092337

**bTT\_5:** (C<sub>4</sub>H<sub>9</sub>N<sub>9</sub>)(NO<sub>3</sub>)<sub>2</sub>·H<sub>2</sub>O, M = 325.24, Triclinic, a = 6.690(5), b = 7.290(4), c = 13.985(5) Å, α = 75.21(10) °, β = 81.90(10) °, γ = 67.68(9) °, V = 609.3(8) Å<sup>3</sup>, T = 173 K, space group *P* $\bar{1}$ , Z = 2, 7338 reflections measured, 2778 unique, (R<sub>int</sub> = 0.036), which were used in all calculations. Final indices (on *F*<sup>2</sup>) were R = 0.038 (*I* > 2σ(*I*)), wR = 0.097 (all data), GOF = 1.07. Final Δρ<sub>max</sub>, Δρ<sub>min</sub> was 0.29 and -0.30 e/Å<sup>3</sup>. CCDC: 2092339

**bTT\_6:** (C<sub>4</sub>H<sub>9</sub>N<sub>9</sub>)ZnCl<sub>4</sub>·2H<sub>2</sub>O, M = 427.41, Monoclinic, a = 9.0580(15), b = 21.642(3), c = 8.4120(19) Å, β = 110.89(2) °, V = 1540.7(5) Å<sup>3</sup>, T = 173 K, space group *P*2<sub>1</sub>/*c*, Z = 4, 7338 reflections measured, 2778 unique, (R<sub>int</sub> = 0.021), which were used in all calculations. Final indices (on *F*<sup>2</sup>) were R = 0.024 (*I* > 2σ(*I*)), wR = 0.052 (all data), GOF = 1.14. Final Δρ<sub>max</sub>, Δρ<sub>min</sub> was 0.29 and -0.33 e/Å<sup>3</sup>. CCDC: 2092341

**bTT\_7:** (C<sub>4</sub>H<sub>9</sub>N<sub>9</sub>)(SO<sub>4</sub>), M = 427.41, Monoclinic, a = 6.3710(11), b = 11.251(3), c = 14.4290(15) Å, β = 109.517(10) °, V = 974.8(3) Å<sup>3</sup>, T = 173 K, space group *P*2<sub>1</sub>/*c*, Z = 4, 7822 reflections measured, 2232 unique, (R<sub>int</sub> = 0.023), which were used in all calculations. Final indices (on *F*<sup>2</sup>) were R = 0.028 (*I* > 2σ(*I*)), wR = 0.077 (all data), GOF = 1.10. Final Δρ<sub>max</sub>, Δρ<sub>min</sub> was 0.37 and -0.38 e/Å<sup>3</sup>. CCDC not submitted yet

**bTT\_8:** K(C<sub>4</sub>H<sub>6</sub>N<sub>9</sub>)·2H<sub>2</sub>O, M = 255.31, Monoclinic, a = 4.230(3), b = 17.330(5), c = 13.579(4) Å, β = 90.99(2) °, V = 995.3(8) Å<sup>3</sup>, T = 173 K, space group *P*2<sub>1</sub>/*c*, Z = 4, 6339 reflections measured, 2241 unique, (R<sub>int</sub> = 0.029), which were used in all calculations. Final indices (on *F*<sup>2</sup>) were R = 0.031 (*I* > 2σ(*I*)), wR = 0.078 (all data), GOF = 1.06. Final Δρ<sub>max</sub>, Δρ<sub>min</sub> was 0.28 and -0.27 e/Å<sup>3</sup>. CCDC: 2092342

**Benzim:**  $C_{14}H_{12}N_2O_2$ ,  $M = 240.26$ , Orthorhombic,  $a = 8.9650(6)$ ,  $b = 9.8970(19)$ ,  $c = 13.848(2)$  Å,  $V = 1228.7(3)$  Å<sup>3</sup>,  $T = 298$  K, space group  $Pna2_1$ ,  $Z = 4$ , 5493 reflections measured, 2585 unique, ( $R_{int} = 0.0558$ ), which were used in all calculations. Final indices (on  $F^2$ ) were  $R = 0.050$  ( $I > 2\sigma(I)$ ),  $wR = 0.097$  (all data),  $GOF = 1.03$ . Final  $\Delta\rho_{max}$ ,  $\Delta\rho_{min}$  was 0.14 and -0.15 e/Å<sup>3</sup>. CCDC not submitted yet

**Fluorim:**  $C_{14}H_{11}FN_2O_2$ ,  $M = 258.25$ , Orthorhombic,  $a = 16.9900$ ,  $b = 14.206(5)$ ,  $c = 20.111(6)$  Å,  $V = 4854(2)$  Å<sup>3</sup>,  $T = 298$  K, space group  $Pbca$ ,  $Z = 16$ , 19551 reflections measured, 5399 unique, ( $R_{int} = 0.031$ ), which were used in all calculations. Final indices (on  $F^2$ ) were  $R = 0.049$  ( $I > 2\sigma(I)$ ),  $wR = 0.146$  (all data),  $GOF = 1.07$ . Final  $\Delta\rho_{max}$ ,  $\Delta\rho_{min}$  was 0.19 and -0.23 e/Å<sup>3</sup>. CCDC not submitted yet

**Toluim:**  $C_{15}H_{14}N_2O_2$ ,  $M = 254.28$ , Orthorhombic,  $a = 8.831(5)$ ,  $b = 9.877(8)$ ,  $c = 14.715(6)$  Å,  $V = 1283.5(14)$  Å<sup>3</sup>,  $T = 298$  K, space group  $P2_12_12_1$ ,  $Z = 4$ , 7479 reflections measured, 2896 unique, ( $R_{int} = 0.070$ ), which were used in all calculations. Final indices (on  $F^2$ ) were  $R = 0.057$  ( $I > 2\sigma(I)$ ),  $wR = 0.126$  (all data),  $GOF = 1.07$ . Final  $\Delta\rho_{max}$ ,  $\Delta\rho_{min}$  was 0.22 and -0.22 e/Å<sup>3</sup>. CCDC not submitted yet

**Toluim\_NMP1:**  $C_{15}H_{14}N_2O_2 \cdot C_3H_7NO$ ,  $M = 353.41$ , Orthorhombic,  $a = 7.3790(12)$ ,  $b = 14.380(2)$ ,  $c = 17.192(3)$  Å,  $V = 1824.2(5)$  Å<sup>3</sup>,  $T = 173$  K, space group  $P2_12_12_1$ ,  $Z = 4$ , 9645 reflections measured, 3937 unique, ( $R_{int} = 0.059$ ), which were used in all calculations. Final indices (on  $F^2$ ) were  $R = 0.048$  ( $I > 2\sigma(I)$ ),  $wR = 0.129$  (all data),  $GOF = 1.05$ . Final  $\Delta\rho_{max}$ ,  $\Delta\rho_{min}$  was 0.24 and -0.25 e/Å<sup>3</sup>. CCDC not submitted yet

**Toluim\_NMP2:**  $C_{15}H_{14}N_2O_2 \cdot C_3H_7NO$ ,  $M = 353.41$ , Monoclinic,  $a = 15.384(6)$ ,  $b = 14.307(5)$ ,  $c = 21.295(8)$  Å,  $\beta = 129.01(2)^\circ$ ,  $V = 3642(2)$  Å<sup>3</sup>,  $T = 173$  K, space group  $P2_1/c$ ,  $Z = 8$ , 50606 reflections measured, 8324 unique, ( $R_{int} = 0.090$ ),

which were used in all calculations. Final indices (on  $F^2$ ) were  $R = 0.059$  ( $I > 2\sigma(I)$ ),  $wR = 0.152$  (all data),  $GOF = 1.06$ . Final  $\Delta\rho_{\max}$ ,  $\Delta\rho_{\min}$  was 0.24 and -0.22 e/Å<sup>3</sup>. CCDC not submitted yet

**Toluid\_NMP3:** C<sub>15</sub>H<sub>14</sub>N<sub>2</sub>O<sub>2</sub>·C<sub>3</sub>H<sub>6</sub>NO,  $M = 353.41$ , Monoclinic,  $a = 7.786(3)$ ,  $b = 14.321(3)$ ,  $c = 16.686(3)$  Å,  $\alpha = 91.048(16)^\circ$ ,  $\beta = 129.01(2)^\circ$ ,  $\gamma = 99.57(3)^\circ$ ,  $V = 1822.1(8)$  Å<sup>3</sup>,  $T = 173$  K, space group  $P\bar{1}$ ,  $Z = 4$ , 20862 reflections measured, 8278 unique, ( $R_{\text{int}} = 0.064$ ), which were used in all calculations. Final indices (on  $F^2$ ) were  $R = 0.056$  ( $I > 2\sigma(I)$ ),  $wR = 0.135$  (all data),  $GOF = 1.03$ . Final  $\Delta\rho_{\max}$ ,  $\Delta\rho_{\min}$  was 0.20 and -0.21 e/Å<sup>3</sup>. CCDC not submitted yet

**All crystal structures without the CCDC number can be provided on request.**

## List of Publications

Effect of chalcogen bond on the packing and coordination geometry in hybrid organic-inorganic Cu(II) networks, *manuscript in preparation*.

Snake-like macroscopic motion in a new dynamic crystal solvate, *manuscript in preparation*

1. Emmanuele Parisi, Alessandro Landi, Sandra Fusco, Carla Manfredi, Andrea Peluso, Sabrina Wahler, Thomas M. Klapötke, and Roberto Centore “[High-Energy-Density Materials: an amphoteric N-Rich Bis\(triazole\) and Salts of Its Cationic and Anionic Species.](#)” *Inorganic Chemistry*, **2021**, 60, 21, 16213-16222. doi.org/10.1021/acs.inorgchem.1c02002
2. Emmanuele Parisi and Roberto Centore “[Stabilization of an elusive tautomer by metal coordination.](#)” *Acta Crystallographica C* **2021**, C77, 395-401 doi.org/10.1107/S2053229621006203
3. Sukuntala Gupta, Partha Pratim Das, Przemyslaw Kula, Emmanuele Parisi and Roberto Centore “[Phase behavior and crystal structures of 2,3-difluorinated p-terphenyl derivatives.](#)” *Acta crystallographica C* **2021**, C77, 435-440 doi.org/10.1107/S2053229621006367
4. Emmanuele Parisi, Domenica Capasso, Amedeo Capobianco, Andrea Peluso, Sonia di Gaetano, Sandra Fusco, Carla Manfredi, Rosaria Mozzillo, Gabriella Pinto and Roberto Centore “[Tautomeric and conformational switching in a new versatile N-rich heterocyclic ligand.](#)” *Dalton Transactions* **2020**, 49(41), 14452-14462. doi.org/10.1039/D0DT02572K
5. Azizolla Beheshti, Fatemeh Panahi, Peter Mayer, Hossein Motamedi, Emmanuele Parisi and Roberto Centore “[Synthesis, structural characterization, antibacterial activity and selective dye adsorption of silver \(I\)-based coordination polymers by tuning spacer length and binding mode of chromate anion.](#)” *Journal of Solid State Chemistry* **2020**, 287, 121322. doi.org/10.1016/j.jssc.2020.121322

6. Sandra Fusco, Emmanuele Parisi, Sabato Volino, Carla Manfredi and Roberto Centore. "[Redox and Emission Properties of triazolo-triazole Derivatives and Copper\(II\) Complexes.](#)" *Journal of Solution Chemistry* **2020**, 49(4), 504-521. doi.org/10.1007/s10953-020-00975-3
7. Roberto Centore, Fabio Borbone, Antonio Carella, Mauro Causà, Sandra Fusco, Francesco Silvio Gentile and Emmanuele Parisi "[Hierarchy of Intermolecular Interactions and Selective Topochemical Reactivity in Different Polymorphs of Fused-Ring Heteroaromatics](#)" *Crystal Growth & Design* **2020**, 20(2), 1229-1236. doi.org/10.1021/acs.cgd.9b01491
8. Sandra Fusco, Domenica Capasso, Roberto Centore, Sonia Di Gaetano and Emmanuele Parisi "[A new biologically active molecular scaffold: Crystal structure of 7-\(3-hydroxyphenyl\)-4-methyl-2H-\[1,2,4\]triazolo\[3,2-c\]\[1,2,4\]triazole and selective antiproliferative activity of three isomeric triazolo-triazoles.](#)" *Acta crystallographica C* **2019**, 75, 1398-1404. doi.org/10.1107/S2053229619012403
9. "[Poly\[\( \$\mu\$ 4-phenylphosphonato\)zinc\(II\)\]](#)" *IUCrData* **2019**, 4, .doi.org/10.1107/S2414314619012227

## Bibliography

- 1 I. Kitaigorodoski, A., *Molecular crystals and molecules*, Academic Press, New York, Academic P., 1973.
- 2 G. R. Desiraju, *Angew. Chemie - Int. Ed.*, 2007, **46**, 8342–8356.
- 3 R. Pepinsky, *Phys. Rev.*, 1955, **100**, 971.
- 4 G. M. J. Schmidt, *Pure Appl. Chem.*, 1971, **27**, 647–678.
- 5 G. R. Desiraju, *Stimul. Concepts Chem.*, 2005, 293–306.
- 6 S. Saha, M. K. Mishra, C. M. Reddy and G. R. Desiraju, *Acc. Chem. Res.*, 2018, **51**, 2957–2967.
- 7 Ö. Almarsson and M. J. Zaworotko, *Chem. Commun.*, 2004, 1889–1896.
- 8 H. Furukawa, K. E. Cordova, M. O’Keeffe and O. M. Yaghi, *Science*, 2013, **341**, 1230444.
- 9 K. Yadava, G. Gallo, S. Bette, C. E. Mulijanto, D. P. Karothu, I. H. Park, R. Medishetty, P. Naumov, R. E. Dinnebier and J. J. Vittal, *IUCrJ*, 2020, **7**, 83–89.
- 10 L. He, S. Ji, H. Lai and T. Chen, *J. Mater. Chem. B*, 2015, **3**, 8383–8393.
- 11 Z. M. Saeed, B. Dhokale, A. F. Shunnar, W. M. Awad, H. H. Hernandez, P. Naumov and S. Mohamed, *Cryst. Growth Des.*, 2021, **21**, 4151–4161.
- 12 D. Marabello, P. Antoniotti, P. Benzi, F. Beccari, C. Canepa, E. Cariati, A. Cioci and L. Lo Presti, *Acta Crystallogr. Sect. B Struct. Sci. Cryst. Eng. Mater.*, 2021, **77**, 506–514.
- 13 Y. Li, M. Qiu, Y. Bai, S. Qu and Z. Hao, *J. Serbian Chem. Soc.*, 2018, **83**, 265–270.
- 14 M. Annadhasan, S. Basak, N. Chandrasekhar and R. Chandrasekar, *Adv. Opt. Mater.*, 2020, **8**, 1–30.
- 15 C. Yang, L. Zhu, R. A. Kudla, J. D. Hartman, R. O. Al-Kaysi, S. Monaco, B. Schatschneider, A. Magalhães, G. J. O. Beran, C. J. Bardeen and L. J. Mueller, *CrystEngComm*, 2016, **18**, 7319–7329.
- 16 Z. Chen, S. Duan, X. Zhang, B. Geng, Y. Xiao, J. Jie, H. Dong, L. Li and W. Hu, *Adv. Mater.*, 2021, **2104166**, 1–9.

- 17 B. H. Lessard, *ACS Appl. Mater. Interfaces*, 2021, **13**, 31321–31330.
- 18 A. Yassar, *Polym. Sci. - Ser. C*, 2014, **56**, 4–19.
- 19 <https://www.marketsandmarkets.com/Market-Reports/organic-electronics-market-144113962.html#:~:text=The%20global%20organic%20electronics%20market%20size%20is%20expected,to%20grow%20rapidly%20in%20the%20coming%20five%20years>.
- 20 P. Yu, Y. Zhen, H. Dong and W. Hu, *Chem*, 2019, **5**, 2814–2853.
- 21 W. Zhao, S. Li, H. Yao, S. Zhang, Y. Zhang, B. Yang and J. Hou, *J. Am. Chem. Soc.*, 2017, **139**, 7148–7151.
- 22 H. Y. Chen, G. Schweicher, M. Planells, S. M. Ryno, K. Broch, A. J. P. White, D. Simatos, M. Little, C. Jellett, S. J. Cryer, A. Marks, M. Hurhangee, J. L. Brédas, H. Sirringhaus and I. McCulloch, *Chem. Mater.*, 2018, **30**, 7587–7592.
- 23 J. J. Yoo, G. Seo, M. R. Chua, T. G. Park, Y. Lu, F. Rotermund, Y. K. Kim, C. S. Moon, N. J. Jeon, J. P. Correa-Baena, V. Bulović, S. S. Shin, M. G. Bawendi and J. Seo, *Nature*, 2021, **590**, 587–593.
- 24 W. S. Yang, J. H. Noh, N. J. Jeon, Y. C. Kim, S. Ryu, J. Seo and S. Il Seok, *Science*, 2015, **348** (6240), 1234–1237.
- 25 E. Lamanna, F. Matteocci, E. Calabrò, L. Serenelli, E. Salza, L. Martini, F. Menchini, M. Izzì, A. Agresti, S. Pescetelli, S. Bellani, A. E. Del Río Castillo, F. Bonaccorso, M. Tucci and A. Di Carlo, *Joule*, 2020, **4**, 865–881.
- 26 V. La Ferrara, A. De Maria, G. Rametta and P. Delli Veneri, *Mater. Adv.*, 2021, **2**, 5396–5405.
- 27 Y. Wang, C. Ji, X. Liu, S. Han, J. Zhang, Z. Sun, A. Khan and J. Luo, *Inorg. Chem. Front.*, 2018, **5**, 2450–2455.
- 28 B. Bin Deng, C. C. Xu, T. T. Cheng, Y. T. Yang, Y. T. Hu, P. Wang, W. H. He, M. J. Yang and W. Q. Liao, *J. Am. Chem. Soc.*, 2020, **142**, 6946–6950.
- 29 P. F. Li, W. Q. Liao, Y. Y. Tang, H. Y. Ye, Y. Zhang and R. G. Xiong, *J. Am. Chem. Soc.*, 2017, **139**, 8752–8757.
- 30 G. Kieslich, S. Sun and A. K. Cheetham, *Chem. Sci.*, 2015, **6**, 3430–3433.

- 31 Z. Sun, A. Martinez and F. Wang, *Nat. Photonics*, 2016, **10**, 227–238.
- 32 W. R. Browne and B. L. Feringa, *Nat. Nanotechnol.*, 2006, **1**, 25–35.
- 33 R. Centore, M. Jazbinsek, A. Tuzi, A. Roviello, A. Capobianco and A. Peluso, *CrystEngComm*, 2012, **14**, 2645–2653.
- 34 R. Centore, S. Fusco, F. Capone and M. Causà, *Cryst. Growth Des.*, 2016, **16**, 2260–2265.
- 35 T. M. Klapötke, *Chemistry of High-Energy Materials*, 5th edn., Walter de Gruyter, Berlin/Boston, 2019.
- 36 T. M. Klapötke, *Energetic Materials Encyclopedia*, de Gruyter, 2021.
- 37 P. Naumov, S. Chizhik, M. K. Panda, N. K. Nath and E. Boldyreva, *Chem. Rev.*, 2015, **115**, 12440–12490.
- 38 S. Chandra Sahoo, N. K. Nath, L. Zhang, M. H. Semreen, T. H. Al-Tel and P. Naumov, *RSC Adv.*, 2014, **4**, 7640–7647.
- 39 S. C. Abrahams, J. M. Robertson and J. G. White, *Acta Crystallogr.*, 1949, **2**, 238–244.
- 40 V. C. Sinclair, J. M. Robertson and A. McL Mathieson, *Acta Crystallogr.*, 1950, **3**, 251–256.
- 41 G. R. Desiraju and A. Gavezzotti, *Acta Crystallogr. Sect. B*, 1989, **45**, 473–482.
- 42 G. R. Desiraju and A. Gavezzotti, *J. Chem. Soc. Chem. Commun.*, 1989, 621–623.
- 43 M. Chen, L. Yan, Y. Zhao, I. Murtaza, H. Meng and W. Huang, *J. Mater. Chem. C*, 2018, **6**, 7416–7444.
- 44 H. Klauk, M. Halik, U. Zschieschang, F. Eder, G. Schmid and C. Dehm, *Appl. Phys. Lett.*, 2003, **82**, 4175–4177.
- 45 H. Okamoto, N. Kawasaki, Y. Kaji, Y. Kubozono, A. Fujiwara and M. Yamaji, *J. Am. Chem. Soc.*, 2008, **130**, 10470–10471.
- 46 P. Y. Gu, Z. Wang, G. Liu, H. Yao, Z. Wang, Y. Li, J. Zhu, S. Li and Q. Zhang, *Chem. Mater.*, 2017, **29**, 4172–4175.
- 47 C. Wetzel, A. Mishra, E. Mena-osteritz, A. Liess, M. Stolte, F. Wu and P. Ba, *Org. Lett.*, 2014, **1**, 1–4.

- 48 G. Cavallo, P. Metrangolo, T. Pilati, G. Resnati and G. Terraneo, *Cryst. Growth Des.*, 2014, **14**, 2697–2702.
- 49 P. Scilabra, G. Terraneo and G. Resnati, *Acc. Chem. Res.*, 2019, **52**, 1313-1324.
- 50 P. C. Ho, J. Z. Wang, F. Meloni and I. Vargas-Baca, *Coord. Chem. Rev.*, 2020, **422**, 213464.
- 51 E. R. T. Tiekink, *Coord. Chem. Rev.*, 2021, **443**, 214031.
- 52 G. R. Desiraju, P. S. Ho, L. Kloo, A. C. Legon, R. Marquardt, P. Metrangolo, P. Politzer, G. Resnati and K. Rissanen, *Pure Appl. Chem.*, 2013, **85**, 1711–1713.
- 53 A. F. Cozzolino, I. Vargas-Baca, S. Mansour and A. H. Mahmoudkhani, *J. Am. Chem. Soc.*, 2005, **127**, 3184–3190.
- 54 S. Tsuzuki and N. Sato, *J. Phys. Chem. B*, 2013, **117**, 6849–6855.
- 55 M. R. and S. C. R. Dovesi, V. R. Saunders, C. Roetti, R. Orlando, C. M. Zicovich-Wilson, F. Pascale, B. Civalleri, K. Doll, N. M. Harrison, I. J. Bush, P. D’Arco, M. Llunell, M. Causà, Y. Noël, L. Maschio, A. Erba, *CRYSTAL17*, User’s Manual, University of Torino.
- 56 P. R. . J. Turner, M. J.; McKinnon, J. J.; Wolff, S. K.; Grimwood, D. J.; Spackman and M. A. D.; *CrystalExplorer17*, Spackman, 2017.
- 57 M. Causà and R. Centore, *CrystEngComm*, 2017, **19**, 1320–1327.
- 58 U. H. F. Bunz, *Acc. Chem. Res.*, 2015, **48**, 1676–1686.
- 59 M. P. Cava and R. H. Schlessinger, *Tetrahedron Lett.*, 1964, **5**, 3815–3818.
- 60 J. D. Dunitz, V. Schomaker and K. N. Trueblood, *J. Phys. Chem.*, 1988, **92**, 856–867.
- 61 G. S. Papaefstathiou, A. Tsohos, C. P. Raptopoulou, A. Terzis, V. Psycharis, D. Gatteschi and S. P. Perlepes, *Cryst. Growth Des.*, 2001, **1**, 191–194.
- 62 H.-K. Fun, J. H. Goh, A. C. Maity and S. Goswami, *Acta Crystallogr. Sect. E Struct. Reports Online*, 2011, **67**, m181–m182.
- 63 V. Luzzati, *Acta Crystallogr.*, 1951, **4**, 193–200.
- 64 J. S. Miller and A. J. Epstein, *MRS Bull.*, 2000, **25**, 21–30.

- 65 G. S. Papaefstathiou, S. P. Perlepes, A. Escuer, R. Vicente, A. Gantis, C. P. Raptopoulou, A. Tsohos, V. Psycharis, A. Terzis and E. G. Bakalbassis, *J. Solid State Chem.*, 2001, **159**, 371–378.
- 66 C. J. Milios, P. V. Ioannou, C. P. Raptopoulou and G. S. Papaefstathiou, *Polyhedron*, 2009, **28**, 3199–3202.
- 67 L. M. Lee, P. J. W. Elder, P. A. Dube, J. E. Greedan, H. A. Jenkins, J. F. Britten and I. Vargas-Baca, *CrystEngComm*, 2013, **15**, 7434–7437.
- 68 W. Li, Z. Wang, F. Deschler, S. Gao, R. H. Friend and A. K. Cheetham, *Nat. Rev. Mater.*, 2017, **2**, 16099.
- 69 A. Caretta, R. Miranti, A. H. Arkenbout, A. O. Polyakov, A. Meetsma, R. Hidayat, M. O. Tjia, T. T. M. Palstra and P. H. M. van Loosdrecht, *J. Phys. Condens. Matter*, 2013, **25**, 505901.
- 70 L. Zhao, T. L. Hung, C. C. Li, Y. Y. Chen, M. K. Wu, R. K. Kremer, M. G. Banks, A. Simon, M. H. Whangbo, C. Lee, J. S. Kim, I. Kim and K. H. Kim, *Adv. Mater.*, 2012, **24**, 2469–2473.
- 71 P. Martins, J. Jesus, S. Santos, L. R. Raposo, C. Roma-Rodrigues, P. V. Baptista and A. R. Fernandes, *Molecules*, 2015, **20**, 16852–16891.
- 72 A. J. Heeger, *Chem. Soc. Rev.*, 2010, **39**, 2354–2371.
- 73 Q. Miao, *Adv. Mater.*, 2014, **26**, 5541–5549.
- 74 M. Argeri, F. Borbone, U. Caruso, M. Causà, S. Fusco, B. Panunzi, A. Roviello, R. Shikler and A. Tuzi, *Eur. J. Inorg. Chem.*, 2014, **2014**, 5916–5924.
- 75 C. Maglione, A. Carella, R. Centore, S. Fusco, A. Velardo, A. Peluso, D. Colonna and A. Di Carlo, *J. Photochem. Photobiol. A Chem.*, 2016, **321**, 79–89.
- 76 C. B. Nielsen, S. Holliday, H.-Y. Chen, S. J. Cryer and I. McCulloch, *Acc. Chem. Res.*, 2015, **48**, 2803–2812.
- 77 M. L. Gettings, S. E. Davis Finch, A. Sethia, E. F. C. Byrd, M. Zeller and D. G. Piercey, *Inorg. Chem.*, 2021, **60**, 7607–7611.
- 78 C. Bian, Q. Lei, J. Zhang, X. Guo, Z. Ma, H. Yang, H. Li and Z. Xiao, *Polyhedron*, 2021, **201**, 115158.
- 79 Y. C. Martin, *J. Comput. Aided. Mol. Des.*, 2009, **23**, 693–704.
- 80 M. Sutradhar, E. C. B. A. Alegria, K. T. Mahmudov, M. F. C. Guedes Da

- Silva and A. J. L. Pombeiro, *RSC Adv.*, 2016, **6**, 8079–8088.
- 81 S. Fusco, E. Parisi, A. Carella, A. Capobianco, A. Peluso, C. Manfredi, F. Borbone and R. Centore, *Cryst. Growth Des.*, 2018, **18** (10), 6293–6301
- 82 R. Centore, C. Manfredi, A. Capobianco, S. Volino, M. V. Ferrara, A. Carella, S. Fusco and A. Peluso, *J. Org. Chem.*, 2017, **82**, 5155–5161.
- 83 R. Centore, C. Manfredi, S. Fusco, C. Maglione, A. Carella, A. Capobianco, A. Peluso, D. Colonna and A. Di Carlo, *J. Mol. Struct.*, 2015, **1093**, 119–124.
- 84 M. Pagacz-Kostrzewa, A. Bil and M. Wierzejewska, *J. Photochem. Photobiol. A Chem.*, 2017, **335**, 124–129.
- 85 R. Centore, S. Fusco, A. Capobianco, V. Piccialli, S. Zaccaria and A. Peluso, *Eur. J. Org. Chem.*, 2013, 3721–3728.
- 86 A. G. Harter, T. M. Klapötke, J. Stierstorfer, M. Voggenreiter and X. Zeng, *ChemPlusChem*, 2021, **86**, 870–874.
- 87 L. Hu, R. J. Staples and J. M. Shreeve, *Chem. Eng. J.*, 2021, **420**, 129839.
- 88 F. Lu, E. Wang, J. Huang, M. Huang, F. Nie and F. X. Chen, *Polyhedron*, 2016, **117**, 445–452.
- 89 Z. M. Li, J. G. Zhang, Y. Cui, T. L. Zhang, Y. J. Shu, V. P. Sinditskii, V. V. Serushkin and V. Yu. Egorshin, *J. Chem. Eng. Data*, 2010, **55**, 3109–3116.
- 90 T. M. Klapötke, P. C. Schmid, S. Schnell and J. Stierstorfer, *Chem. Eur. J.*, 2015, **21**, 9219–9228.
- 91 R. Centore, A. Carella and S. Fusco, *Struct. Chem.*, 2011, **22**, 1095–1103.
- 92 T. M. Klapötke, P. C. Schmid, S. Schnell and J. Stierstorfer, *J. Mater. Chem. A*, 2015, **3**, 2658–2668.
- 93 R. Centore, M. Causà, S. Fusco and A. Carella, *Cryst. Growth Des.*, 2013, **13**, 3255–3260.
- 94 Y. Tang, Z. Yin, A. K. Chinnam, R. J. Staples and J. M. Shreeve, *Inorg. Chem.*, 2020, **59**, 17766–17774.
- 95 Y. Xue, H. Xiong, J. Tang, G. Cheng and H. Yang, *Prop. Explos. Pyrotech.*, 2021, **46**, 1070–1078.

- 96 R. C. Weast, *CRC Handbook of Chemistry and Physics*, CRC Press Inc., Boca Raton, Florida, 65th edn., 1984.
- 97 H. Östmark, U. Bemm, H. Bergman and A. Langlet, *Thermochim. Acta*, 2002, **384**, 253–259.
- 98 C. Xue, J. Sun, B. Kang, Y. Liu, X. Liu, G. Song and Q. Xue, *Prop. Explos. Pyrotech.*, 2010, **35**, 333–338.
- 99 M. Suceska, *EXPLO5 – COMPUTER PROGRAM FOR CALCULATION OF DETONATION*, Version 6.05.02, Zagreb, 2018.
- 100 V. Bruno, A. Castaldo, R. Centore, A. Sirigu, F. Sarcinelli, M. Casalboni and R. Pizzoferrato, *J. Polym. Sci. Part A Polym. Chem.*, 2002, **40**, 1468–1475.
- 101 A. Anbarasi, S. M. Ravi Kumar, G. J. S. Sundar, M. A. Mosses, M. P. Raj, M. Prabhakaran, R. Ravisankar and R. Gunaseelan, *Phys. B Condens. Matter*, 2017, **522**, 31–38.
- 102 M. Thakur, J. Xu, A. Bhowmik and L. Zhou, *Appl. Phys. Lett.*, 1999, **74**, 635–637.
- 103 T. Kaino, B. Cai and K. Takayama, *Adv. Funct. Mater.*, 2002, **12**, 599–603.
- 104 L. R. Dalton, W. H. Steier, B. H. Robinson, C. Zhang, A. Ren, S. Garner, A. Chen, T. Londergan, L. Irwin, B. Carlson, L. Fifield, G. Phelan, C. Kincaid, A. Jen, S. California and L. Angeles, *J. Mater. Chem.* 1999, **9**, 1905–1920.
- 105 K. Jagannathan, P. Umarani, V. Ratchagar, V. Ramesh and S. Kalainathan, *Spectrochim. Acta - Part A Mol. Biomol. Spectrosc.*, 2016, **153**, 735–740.
- 106 P. A. Franken, A. E. Hill, C. W. Peters and G. Weinreich, *Phys. Rev. Lett.*, 1961, **7**, 118–119.
- 107 Y. Enami, C. T. Derose, D. Mathine, C. Loychik, C. Greenlee, R. A. Norwood, T. D. Kim, J. Luo, Y. Tian, A. K.-Y. Jen and N. Peyghambarian, *Nat. Photonics*, 2007, **1**, 180–185.
- 108 H. Ma, A. K.-Y. Jen and L. R. Dalton, *Adv. Mater.*, 2002, **14**, 1339–1365.
- 109 G. Pasupathi and P. Philominathan, *J. Miner. Mater. Charact. Eng.*, 2012, **11**, 904–907.

- 110 B. L. Koreneva, L. G. ; Zolin, V. F. ; Davydov, *Nonlinear optics of molecular crystals*, Moscow, Izdatel'stvo Nauka, 1985.
- 111 M. Packiya raj, S. M. Ravi Kumar, D. Sivavishnu, T. Kubendiran, A. Anbarasi and S. E. Allen Moses, *Cryst. Res. Technol.*, 2018, **53**, 1700271.
- 112 Y. Zheng, X. Jia, K. Li, J. Xu and X. Bu, *Adv. Energy Mater.*, 2021, 2100324.
- 113 F. Cai, J. Yu, J. Qian, Y. Wang, Z. Chen, J. Huang, Z. Ye and S. He, *Laser Photon. Rev.*, 2014, **8**, 865–874.
- 114 J. Zyss and J. L. Oudar, *Phys. Rev. A*, 1982, **26**, 2028–2048.
- 115 S.-H. Lee, B.-J. Kang, J.-S. Kim, B.-W. Yoo, J.-H. Jeong, K.-H. Lee, M. Jazbinsek, J. W. Kim, H. Yun, J. Kim, Y. S. Lee, F. Rotermund and O. P. Kwon, *Adv. Opt. Mater.*, 2015, **3**, 756–762.
- 116 O.-P. Kwon, S.-J. Kwon, M. Jazbinsek, A. Choubey, V. Gramlich and P. Günter, *Adv. Funct. Mater.*, 2007, **17**, 1750–1756.
- 117 R. Centore, A. Roviello, in *Advances in Macromolecules*, M. V. Russo Editor. Springer US, 2010, 79–117.
- 118 C. Pratt Brock and J. D. Dunitz, *Chem. Mater.*, 2002, **6**, 1118–1127.
- 119 U. Caruso, R. Centore, B. Panunzi, A. Roviello and A. Tuzi, *Eur. J. Inorg. Chem.*, 2005, **13**, 2747–2753.
- 120 R. Centore, A. Roviello, A. Tuzi and B. Panunzi, *Acta Crystallogr. Sect. C*, 2002, **58**, m26--m28.
- 121 R. Centore and A. Tuzi, *Acta Crystallogr. Sect. C*, 2001, **57**, 698–701.
- 122 O.-P. Kwon, M. Jazbinsek, H. Yun, J.-I. Seo, J.-Y. Seo, S.-J. Kwon, Y. S. Lee and P. Günter, *CrystEngComm*, 2009, **11**, 1541–1544.
- 123 G. M. Frankenbach and M. C. Etter, *Chem. Mater.*, 2002, **4**, 272–278.
- 124 B. K. Saha, A. Nangia and J.-F. Nicoud, *Cryst. Growth Des.*, 2006, **6**, 1278–1281.
- 125 P. Metrangolo, F. Meyer, T. Pilati, G. Resnati and G. Terraneo, *Angew. Chem. Int. Ed.*, 2008, **47**, 6114–6127.
- 126 F. Pan, M. Shing Wong, V. Gramlich, C. Bosshard and P. Günter, *J. Am. Chem. Soc.*, 1996, **118**, 6315–6316.

- 127 J. A. Swift and M. D. Ward, *Chem. Mater.*, 2000, **12**, 1501–1504.
- 128 A. Subashini, K. Ramamurthi and H. Stoeckli-Evans, *Acta Crystallogr. Sect. C*, 2012, **68**, o408--o412.
- 129 D.H. Shi, *Acta Crystallogr. Sect. E*, 2009, **65**, o2107.
- 130 C. Bosshard, M. Bösch, I. Liakatas, M. Jäger and P. Günter, in *Nonlinear Optical Effects and Materials*, Gunter P. Editor, Springer Berlin, 2000, **72** 163–299.
- 131 P. Naumov, D. P. Karothu, E. Ahmed, L. Catalano, P. Commins, J. Mahmoud Halabi, M. B. Al-Handawi and L. Li, *J. Am. Chem. Soc.*, 2020, **142**, 13256–13272.
- 132 S. K. Park and Y. Diao, *Chem. Soc. Rev.*, 2020, 49, 8287–8314.
- 133 H. Koshima, *Mechanically responsive materials for soft robotics*, Wiley-VCH Verlag GmbH & Co. KGaA, 2020.
- 134 D. P. Karothu, J. Mahmoud Halabi, L. Li, A. Colin-Molina, B. Rodríguez-Molina and P. Naumov, *Adv. Mater.*, 2020, **32**, 1–11.
- 135 A. Khalil, D. P. Karothu and P. Naumov, *J. Am. Chem. Soc.*, 2019, **141**, 3371–3375.
- 136 Y. Duan, S. Semin, P. Tinnemans, H. Cuppen, J. Xu and T. Rasing, *Nat. Commun.*, 2019, **10**, 4573.
- 137 R. Maeda, J. J. Tsaur, S. H. Lee and M. Ichiki, *Piezoelectric Microactuator Devices*, Kluwer Academic Publishers, 2004, vol. 12.
- 138 S. Büttgenbach, *Micromachines*, 2014, **5**, 929–942.
- 139 N. Chandrasekhar, M. A. Mohiddon and R. Chandrasekar, *Adv. Opt. Mater.*, 2013, **1**, 305–311.
- 140 R. Chandrasekar, *Phys. Chem. Chem. Phys.*, 2014, **16**, 7173–7183.
- 141 R. Centore and M. Causà, *Cryst. Growth Des.*, 2018, **18**, 3535–3543.
- 142 P. Naumov and P. K. Bharadwaj, *CrystEngComm*, 2015, **17**, 8775.
- 143 H. Koshima, K. Takechi, H. Uchimoto, M. Shiro and D. Hashizume, *Chem. Commun.*, 2011, **47**, 11423–11425.
- 144 L. Zhu, F. Tong, N. Zaghoul, O. Baz, C. J. Bardeen and R. O. Al-Kaysi, *J. Mater. Chem. C*, 2016, **4**, 8245–8252.

- 145 D. Kitagawa, C. Iwaihara, H. Nishi and S. Kobatake, *Crystals*, 2015, **5**, 551–561.
- 146 T. Seki, T. Mashimo and H. Ito, *Chem. Lett.*, 2020, **49**, 174–177.
- 147 P. Naumov, S. C. Sahoo, B. A. Zakharov and E. V. Boldyreva, *Angew. Chemie*, 2013, **125**, 10174–10179.
- 148 M. K. Panda, R. Centore, M. Causà, A. Tuzi, F. Borbone and P. Naumov, *Sci. Rep.*, 2016, **6**, 29610
- 149 C. A. Parker and L. G. Harvey, *Analyst*, 1962, **87**, 558-565.
- 150 J. C. and D. J. F. M. J. Frisch, G. W. Trucks, H. B. Schlegel, G. E. Scuseria, M. A. Robb, J. R. Cheeseman, G. Scalmani, V. Barone, B. Mennucci, G. A. Petersson, H. Nakatsuji, M. Caricato, X. Li, H. P. Hratchian, A. F. Izmaylov, J. Bloino, G. Zheng, J. L. Sonnenberg, M. Had, *GAUSSIAN16*, Revision C.01, Wallinford CT, 2016.
- 151 W. J. Hehre, R. Ditchfield and J. A. Pople, *J. Chem. Phys.*, 1972, **56**, 2257–2261.
- 152 A. D. Boese and J. M. L. Martin, *J. Chem. Phys.*, 2004, **121**, 3405–3416.
- 153 A. Schäfer, C. Huber and R. Ahlrichs, *J. Chem. Phys.*, 1994, **100**, 5829–5835.
- 154 J. Tomasi, B. Mennucci and R. Cammi, *Chem. Rev.*, 2005, **105**, 2999–3094.
- 155 A. Capobianco, M. Di Donato, T. Caruso, R. Centore, A. Lapini, C. Manfredi, A. Velardo, S. Volino and A. Peluso, *J. Mol. Struct.*, 2020, **1203**, 127368.
- 156 A. D. Becke, *J. Chem. Phys.*, 1993, **98**, 5648–5652.
- 157 C. Lee, W. Yang and R. G. Parr, *Phys. Rev. B*, 1988, **37**, 785–789.
- 158 S. Grimme, J. Antony, S. Ehrlich and H. Krieg, *J. Chem. Phys.*, 2010, **132**, 154104.
- 159 D. Vilela Oliveira, J. Laun, M. F. Peintinger and T. Bredow, *J. Comput. Chem.*, 2019, **40**, 2364–2376.
- 160 F. Weigend and R. Ahlrichs, *Phys. Chem. Chem. Phys.*, 2005, **7**, 3297–3305.
- 161 Bruker-Nonius (2002). SADABS, Bruker-Nonius, Delft, The

Netherlands.

- 162 A. Altomare, M. C. Burla, M. Camalli, G. L. Cascarano, C. Giacobozzo, A. Guagliardi, A. G. G. Moliterni, G. Polidori and R. Spagna, *J. Appl. Crystallogr.*, 1999, **32**, 115–119.
- 163 G. M. Sheldrick, *Acta Crystallogr. Sect. C Struct. Chem.*, 2015, **71**, 3–8.
- 164 L. J. Farrugia, *J. Appl. Crystallogr.*, 2012, **45**, 849–854.
- 165 C. F. Macrae, I. J. Bruno, J. A. Chisholm, P. R. Edgington, P. McCabe, E. Pidcock, L. Rodriguez-Monge, R. Taylor, J. Van De Streek and P. A. Wood, *J. Appl. Crystallogr.*, 2008, **41**, 466–470.
- 166 G. Gran, *Analyst*, 1952, **77**, 661–671.
- 167 H. Freiser, *J. Chem. Educ.*, 1962, **39**(7), 379
- 168 P. Gans, A. Sabatini and A. Vacca, *Talanta*, 1996, **43**, 1739–1753.
- 169 NATO standardization agreement (STANAG) on explosives. *Impact sensitivity test No. 4489*, 1st ed., Sept 17, 1999.
- 170 WIWEB-Standardarbeitsanweisung 4-5.1.02. *Ermittlung der Explosionsgefährlichkeit, hier der Schlagempfindlichkeit mit dem Fallhammer*, Nov 8, 2002.
- 171 <http://www.bam.de>, <http://www.bam.de>.
- 172 NATO standardization agreement (STANAG) on explosive. *Friction sensitivity test No. 4487*, 1st ed., Aug 22, 2002
- 173 WIWEB-Standardarbeitsanweisung 4-5.1.03. *Ermittlung der Explosionsgefährlichkeit oder der Reibeempfindlichkeit mit dem Reibeapparat*, Nov 8, 2002
- 174 Impact: insensitive, >40 J; less sensitive,  $\geq 35$  J; sensitive,  $\geq 4$  J; very sensitive,  $\leq 3$  J. Friction: insensitive, >360 N; less sensitive, 360 N; sensitive, <360 N and >80 N; very sensitive,  $\leq 80$  N; extremely sensitive,  $\leq 10$  N. According to the UN recommendations on the transport of dangerous goods.
- 175 <http://www.ozm.cz>., <http://www.ozm.cz>.
- 176 L. A. Curtiss, K. Raghavachari, P. C. Redfern, V. Rassolov and J. A. Pople, *J. Chem. Phys.*, 1998, **109**, 7764–7776.
- 177 B. M. Rice and E. F. C. Byrd, *J. Mater. Res.*, 2006, **21**, 2444–2452.

- 178 E. F. C. Byrd and B. M. Rice, *J. Phys. Chem. A*, 2006, **110**, 1005–1013.
- 179 P. J. Linstrom, W. G. Mallard (eds). NIST Chemistry WebBook, NIST Standard Reference Database Number 69, June 2005, National Institute of Standards and Technology, Gaithersburg MD, 20899 (<http://webbook.nist.gov>).
- 180 D. H. Williams and M. S. Westwell, *Chem. Biol.*, 1996, **3**, 695–701.
- 181 H. D. B. Jenkins, *Chemical Thermodynamics at a Glance*, Blackwell, Oxford. 2008.
- 182 H. D. B. Jenkins, H. K. Roobottom, J. Passmore and L. Glasser, 1999, *Inorg. Chem.* 3609–3620.
- 183 H. D. B. Jenkins, D. Tudela and L. Glasser, *Inorg. Chem.*, 2002, **41(9)**, 2364–2367.